High Efficiency Single and Multijunction Organic Photovoltaics

by

Xiaozhou Che

A dissertation submitted in partial fulfillment
of the requirements for the degree of
Doctor of Philosophy
(Applied Physics)
in The University of Michigan
2018

Doctoral Committee:

       Professor Stephen R. Forrest, Chair
       Professor Roy Clarke
       Professor Cagliyan Kurdak
       Professor Jamie D. Phillips

Xiaozhou Che

amyche@umich.edu

ORCID iD: 0000-0002-6697-7522

For all the people I love and by whom I am loved

ACKNOWLEDGEMENTS

I still remember the date, Aug. 15, 2012, when I took a long flight from my hometown Beijing to Detroit, marking the beginning of my PhD at the University of Michigan. Time always flies faster than we expect, and I'm about to cross the finish line of this journey of which I enjoyed every moment. My accomplishments achieved during the PhD program would have been impossible without the help of others. I'd like to take this chance to express my sincere gratitude to every one of them.

I'm grateful to Professor Cagliyan Kurdak, the director of the Applied Physics Program. He interviewed me during my application and offered the fellowship. Without him I would not have had the opportunity to study at the University of Michigan. I also want to acknowledge the program founder and former director, Professor Roy Clarke, and the staff members, Charles Sutton, Cynthia McNabb and Lauren Segall. All of them work hard to make the Applied Physics a unique program and a lovely family. I'd like to thank Professor Jamie D. Phillips for being part of my committee. It was fun taking his class and talking with him about solar cell research.

My most sincere gratitude goes to my PhD advisor, Professor Stephen R. Forrest. His passion and profound understanding towards science sets a great example. He always pushes me in a positive direction to challenge myself and think outside the box to achieve the impossible, shaping me into a qualified PhD researcher. He is also very amusing and knowledgeable, making the group meetings and personal conversations full of fun stuff to learn besides science. The experience of working in his group will undoubtedly benefit me for the rest of my life.

My research projects would not have been accomplished without the help of my colleagues and collaborators. Our group administrator, Eva Ruff, does everything she could can to assist us with the logistics. My mentor, Xin Xiao, spent lots of time teaching me the basic knowledge and experimental/data analysis skills that well prepared me for later projects. I especially thank the Sunshot team: Jeramy D. Zimmerman, Brian E. Lassiter, Xin Xiao, Olga L. Griffith, Kyusang Lee, Yongxi Li, Quinn Burlingame, Boning Qu and many others. It was challenging but also fun to accomplish certain milestones and present them via teleconference every quarter. I'm also thankful to all the other students in the OCM group. We have a fantastic group culture where everyone is willing to help and make friends with each other. The group parties and activities are really unique memories.

In addition, I'd like to acknowledge Professor Ken-Tsung Wong from National Taiwan University for the collaboration of my d-a-a' molecule projects. My main collaborators from his group are Chin-Lung Chung, Han Han and Chun-Kai Wang. They also gave me a very welcomed reception during my visit to their lab. I want to acknowledge my undergraduate research advisor at Peking University, Dapeng Yu, who brought me to the scientific world of semiconductor physics and solar cells that convinced me to pursue my PhD degree.

Last but not least, I want to thank my family for their love and care. My parents always provide endless support for my life and study. My grandparents, especially my grandfather, sets a good model as a scientist. My aunts, uncles and cousins living across in US make me feel at home in a foreign country. My dissertation is dedicated to everyone I love and by whom I am loved.

Xiaozhou Che

Ann Arbor, April 2018

TABLE OF CONTENTS

LIST OF FIGURES

LIST OF TABLES

ABSTRACT

Organic photovoltaics (OPVs) offer a lightweight and potentially cost-effective approach for solar energy harvesting. The first OPV heterojunction device was reported in 1985 with 1% efficiency. There has been a rapid development of small molecule and polymer materials, as well as different growth techniques such as vapor-deposition and solution-processing over the past 30 years. With recent emergence of the non-fullerene acceptors (NFAs), the efficiency has been improved to 15%; a benchmark for OPV commercialization. The flexible and semitransparent form factors of OPVs also lead to unique applications such as flexible electronics and building integrated photovoltaics (BIPV), showing considerable market potential.

This dissertation will focus on high efficiency single and multijunction OPVs. Following the background introduction of organic materials and solar cells, the simulation methods based on transfer matrix is discussed. The rest of the work can be divided into two parts. The first part studies a group of dipolar donor molecules with donor-acceptor-acceptor' structures, either with the propeller or coplanar donor unit. The molecular conjugation length and side chain configuration are adjusted to better understand the structure-property-performance relationships. In the second part, two multijunction structures will be discussed, both of which employ subcells with the d-a-a' donors. The first structure focuses on the fully vacuum-deposited tandem and triple junction cells with efficiencies of 10-11%, delivering several important multijunction design principles. It is followed by discussion of a tandem cell combining the vacuum-deposited and solution-processed NFA-based subcells, achieving a record

15% efficiency with close to 100% fabrication yield. A variety of characterization methods including crystallography, photoluminescence, external quantum efficiency and current density-voltage measurements, optical simulation etc. will be presented along with these results. With improved donor and NFA materials along with their inherent structural design flexibility, further improvement of OPV performance is expected to be achieved in the near future with plenty of market potential.

CHAPTER I

Introduction to Organic Photovoltaics

Organic material is usually defined as a chemical compound that contains a carbon-hydrogen bond.[1] A more general definition is a compound that contains a significant amount of carbon. While the simple carbon oxides (for example, CO and CO_2) are inorganics, fullerene molecules like C_{60} and C_{70} are considered as organics.

Organic material is an important material category that is found in all living things, from DNA to chromosomes. Organics for optical and electrical applications are divided into small molecules (monomers and oligomers) and polymers. The small molecule has well defined molecular structures and weights, with simple pathways for purification.[2,3] They can be deposited by vapor-deposition or solution process. Polymers, on the other hand, have large molecular weights with repeating subunits along a chain, which can only be solution-processed.[4] Several examples of small molecules and polymers are listed in Fig. 1.1. The names and molecular structures of organic materials mentioned in this dissertation can be found in Appendix A.

Organics are known as excitonic materials. An exciton is defined as a bound state of an electron and a hole with electrostatic Coulomb force, whose binding energy is[5]:

$$E_b = \frac{q^2}{4\pi\varepsilon_0\varepsilon_r r},$$ (1.1)

where $q = 1.6 \times 10^{-19} C$ (elementary charge) and $\varepsilon_0 = 8.85 \times 10^{-12} F/m$ (the per-
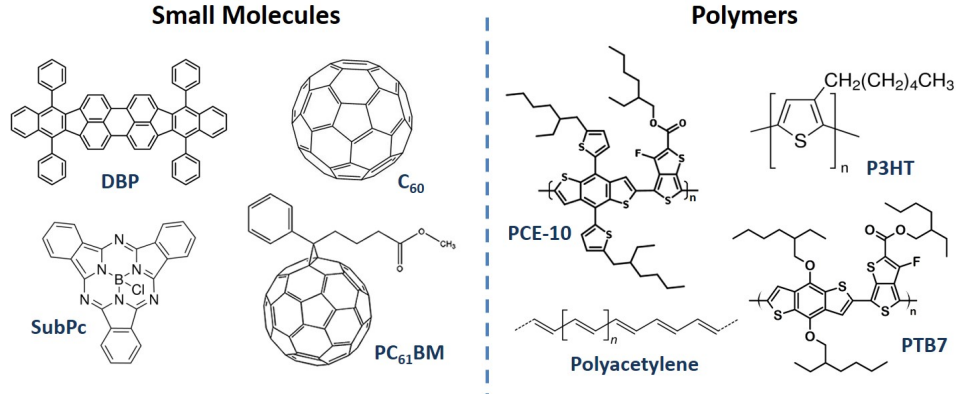
Figure 1.1: Examples of organic small molecules and polymers.

mittivity of free space). The value ε_r is the dielectric constant (also called relative permittivity), and r is the exciton radius. For inorganic materials like silicon or sapphire, ε_r is usually > 10.[6,7] It leads to a small exciton binding energy on the order of 10 meV, which is comparable with the room temperature thermal energy of $k_B T = 26$ meV. The so-called Wannier-Mott excitons, can therefore dissociate at room temperature into free electrons and holes. For organics, the low dielectric constant (~ 3)[8] results in large exciton binding energy of several hundreds meV. Such a tightly bonded electron-hole pair is called the Frenkel exciton, which usually resides on a single molecule with small radius.[9]

Table 1.1: Comparison of inorganic and organic materials.

	Inorganic	*Organic*
Exciton	Wannier-Mott	Frenkel
Charge Transport	Band Transport	Polaron Hopping
Absorption coefficient	Low (10^4-10^5 cm^{-1})	High (10^5-10^6 cm^{-1})
Mobility	High (>1000 cm^2/V·s)	Low (10^{-6}-1 cm^2/Vs)
Exciton binding energy	Low (10-100 meV)	High (500-1000 meV)

Table 1.1 compares the main differences between organic and inorganic materials. Due to the charge transport mechanism of hopping, organics exhibit much lower

2

mobility than the inorganics. On the other hand, the main advantage of organic materials is their much higher absorption coefficient, showing potential for optoelectronic applications including solar cells. Organic devices are usually low cost, light weight, with simple ways of fabrication and mechanical flexibility. Section 1.1 will explain the intra- and inter-molecular properties of organics in detail, leading to the significance of organic semiconductor research. Then in Section 1.2, we will cover basic concepts and properties of organic photovoltaics (OPVs). Finally, Section 1.3 briefly summarizes the OPV history and state of the art, which brings out the topics of following chapters for high efficiency single and multijunction OPVs.

1.1 Properties of organics

1.1.1 Intramolecular properties

Unlike inorganic solids that are held together through strong covalent or ionic bonds resulting in continuous bands, organic molecules interact by the much weaker van der Waals force[10]. The electronic wavefunction is localized on the individual molecules that leads to discrete energy levels with narrow energy band widths. Inside an organic molecule, atoms are connected by covalent bonds with the overlapping electron clouds, causing energy splitting to the lower and higher energy molecular orbitals. To calculate the electronic orbitals of organic materials, the Born-Oppenheimer (B-O) approximation[11] is applied which separates the electronic and nuclear motions. The wavefunction can be written as:

$$\Psi_{total} = \Psi_{electronic} \cdot \Psi_{nuclear} \cdot \sigma_{spin}. \tag{1.2}$$

The total energy components are also treated separately as (near equilibrium):

$$E_{total} = E_e(0) + V_N(0) + \Delta E_e(Q) + \Delta V_N(Q), \tag{1.3}$$

where E_e is the electron kinetic energy, V_N is the nuclear repulsion energy, and Q refers to the relative nuclear coordinate. For an N-electron system, the wavefunction can be written as: $\Phi_e(\{r_i\}) = \prod_{i=1}^{N} \Phi_{e,i}(r_i)$ where r_i is the electron position. The electronic states can then be solved from the eigenvalues of Schrödinger's equation with the B-O approximation, assuming that the electron distribution changes much faster than nuclear positions upon excitation due to the much smaller mass. For more complex systems, the molecular levels can be calculated by density functional theory (DFT)[12], where the electron density functions are used instead of solving the discrete electronic wavefunctions.
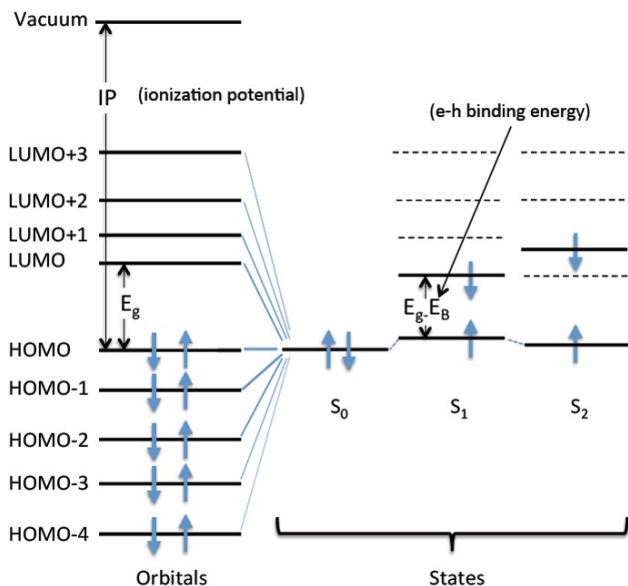
Figure 1.2: Electronic orbitals *vs* molecular states.

As indicated by Fig. 1.2 left, each electronic orbital from the lower to higher energy is filled with two electrons of antiparallel spin based on the Pauli exclusion principle[13]. The HOMO level refers to the highest occupied molecular orbital, while the LUMO level is the lowest unoccupied molecualr orbital. Other orbital levels below the HOMO and above the LUMO are noted as HOMO-1, HOMO-2... and LUMO+1, LUMO+2... respectively. The orbital energies have values < 0 referenced to the vacuum level. Figure 1.2 on the right displays the molecular electronic states.

The ground state is noted as S_0, followed by the singlet excited states S_1, S_2..., with the energies referenced to each other. The electronic states refer to a collection of electrons and contains a linear combination of different orbitals. The most important transition for OPV, for example, is from S_0 to S_1 state, noted as $S_1 \leftarrow S_0$. In the calculation of orbitals we assume molecular relaxation is much slower than excitation. The electronic states are formed after relaxation. Therefore the exciton binding energy, E_B, needs to be included with an energy shift.
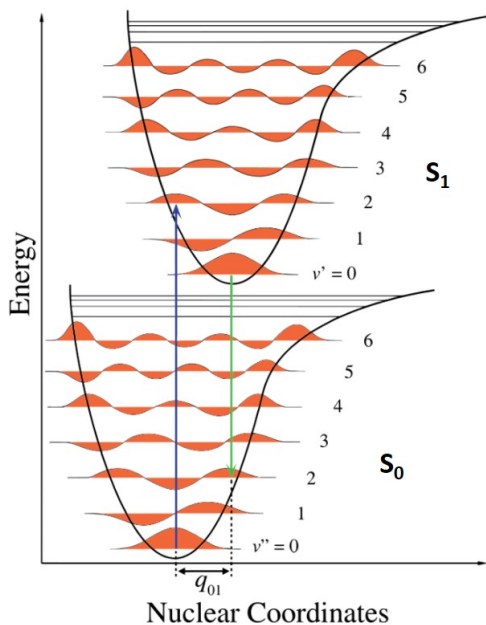
Figure 1.3: Franck-Condon principle energy diagram associating Morse potential and electronic transitions. Figure from Wikipedia:Franck-Condon principle.

While the electrons are treated separately based on the B-O approximation, the nuclear motion also plays an important role upon excitation of the organic molecules. The vibrational excitations are phonon modes, resulting in roughly equal level spacings from the bottom of each electronic state that causes the broadening of absorption bands. The simplified solution has a form of simple harmonic oscillator. It is often corrected by the relatively more accurate Morse potential with a finite energy, where the potential is:

$$V_r = D_e(1 - e^{-\alpha(r-r_e)})^2; \qquad \alpha = \sqrt{k_e/2D_e}, \tag{1.4}$$

where D_e is the well depth, k_e is the force constant at the minimum of the quantum well, α relates to the potential width, and r is the distance between the atoms with the equilibrum bond distance r_e. The eigenenergies of the vibrational states have the form of (m being the nuclei mass):

$$E_n = h\nu_0(n + \frac{1}{2}) - \frac{1}{4D_e}[h\nu_0(n + \frac{1}{2})]^2; \qquad \nu_0 = \frac{a}{2\pi}\sqrt{2D_e/m}. \tag{1.5}$$
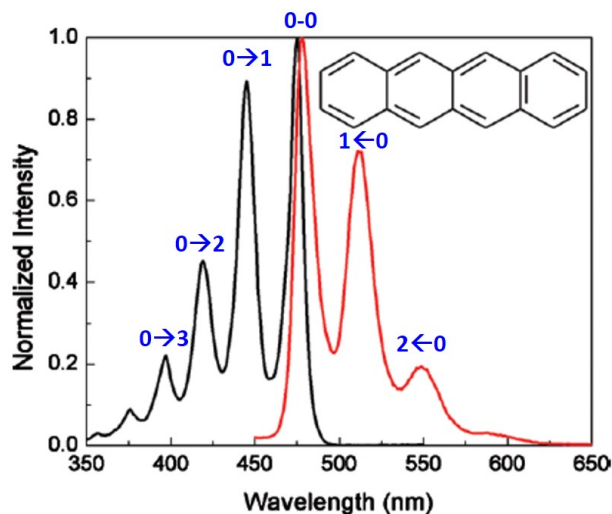
Figure 1.4: Absorption vs emission. Normalized steady state absorption (black) and emission (red) spectra of the tetracene monomer in toluene, displaying small Stokes shift. Figure from Ref.[14]

.

The electronic state diagram with confined vibronic states are illustrated in Fig. 1.3, with a shift q_0 in nuclear coordinates from S_0 to S_1 states. The vibronic transitions follow the Franck-Condon principle approximation[15] that they occur without changes of nuclei positions, resulting in vertical transitions. The organic optical properties are related to the transitions between different states, resulting in absorptions and emissions. At room temperature, the absorption occurs mostly from the lowest

vibronic state of the ground state to different vibronic excited states, noted as 0→0, 0→1, 0→2... According to Kasha's rule,[16] photon emission occurs in appreciable yield after relaxation from the lowest vibronic state of the excited state, i.e. 0←0, 1←0, 2←0... As a result, the emitted photon energy is lower than the absorption. A Stokes shift between the 0-0 absorption and emission transition is usually observed due to molecular rearrangements as shown in Fig. 1.4.

As indicated in Table 1.1, organic materials generally exhibit very strong absorption. The transition probability between the initial (i) and final (f) states follows the Fermi's golden rule:[17]

$$k_{f\leftarrow i} = \frac{2\pi}{\hbar} |<\psi_f|H'|\psi_i>|^2 \, \rho \tag{1.6}$$

with ρ being the density of the final states. The perturbation is $H' = \text{-}\boldsymbol{\mu}\cdot\mathbf{E}$, where $\boldsymbol{\mu}$ refers to the dipole moment and $\mathbf{E}$ refers to the electric field. The matrix element $M_{f\leftarrow i} = <\psi_f|H_{int}|\psi_i>$ should be non-zero to allow for a transition. Based on B-O approximation, it can be written as:

$$M_{f\leftarrow i} = -<\psi_{e,f}(\boldsymbol{r}_f)|\boldsymbol{\mu} \cdot \mathbf{E}|\psi_{e,i}(\boldsymbol{r}_i)><\psi_{N,f}(\boldsymbol{Q}_f)|\psi_{N,i}(\boldsymbol{Q}_i)><\sigma_f(S_f)|\sigma_i(S_i)>. \tag{1.7}$$

The first term is the spatial transition between electronic states, requiring the initial and final states with opposite spatial parity. The transition has higher probability to occur with the dipole moment $\boldsymbol{\mu}$ extending along the molecular axis. The second term comes from the nuclear vibronic transitions, with the Franck-Condon factor (FC) defined as:

$$FC_{f\leftarrow i} = |<\psi_{N,f}(\boldsymbol{Q}_f)|\psi_{N,i}(\boldsymbol{Q}_i)>|^2. \tag{1.8}$$

The transition is more likely with larger overlap between the two vibronic states in different electronic manifolds, i.e., with a higher FC factor. Therefore, a minimal

change of the nucleus position is preferred. The last term in Eq. 1.7 requires the initial and final spin states having the same parity, forbidding singlet-triplet transitions.

The oscillator strength (f) showing the absorption or emission strength between the two states is defined by:[9]

$$f_{in,fm} = \frac{4\pi m_e c}{3q^2 \hbar} \langle \nu_{in,fm} \rangle |\mu_{if,e}|^2 FC_{f \leftarrow i} = \frac{4.319 \times 10^{-9}}{n_0} \int \epsilon(\nu) d\nu, \qquad (1.9)$$

where i and f, n and m refer to the initial and final electronic and vibronic states, respectively; and $\mu_{if,e}$ is the electronic transition dipole moment. The second part of the equation shows a more practical expression where n_0 is the refractive index of the medium, ε is the molar absorption coefficient, and ν is the wavenumber.

1.1.2 Intermolecular properties

In the solid state, organic molecules are held together via the relatively weak van der Waals force compared with the covalent or ionic bonds. The van der Waals force is oriented by the interaction of permanent or induced dipoles. Such dipole-dipole interaction between the molecules produces an attractive force, which is called the London dispersion force that decreases as r^{-6}.[18] In addition, a repulsive component arises at closer distance between the molecules ($\propto r^{-12}$) from the Pauli exclusion principle due to electron orbital overlap. The overall interaction can be approximated by the Lennard-Jones potential[19] as a function of distance:

$$V_{L-J} = 4\varepsilon \left[\left(\frac{\sigma}{r} \right)^6 - \left(\frac{\sigma}{r} \right)^{12} \right], \qquad (1.10)$$

where ε is the potential wall depth, σ is the distance at zero potential, and r is the distance between the molecules.

Due to the weak intermolecular force, the electrons tend to be highly localized on a single molecule. The tight binding approximation is therefore proper to describe

nearest neighbor interactions.[20] That the total Hamitonian is treated as a sum of the individual molecular components and the interaction between neighbors. The solution leads to a broadening of the single molecule electronic orbitals into narrow energy bands, as illustrated by Fig. 1.5. In contrast to the continuous band structure of inorganics, the discrete energy bands for organic materials result in charge transfer by thermally-assisted hopping.[9]
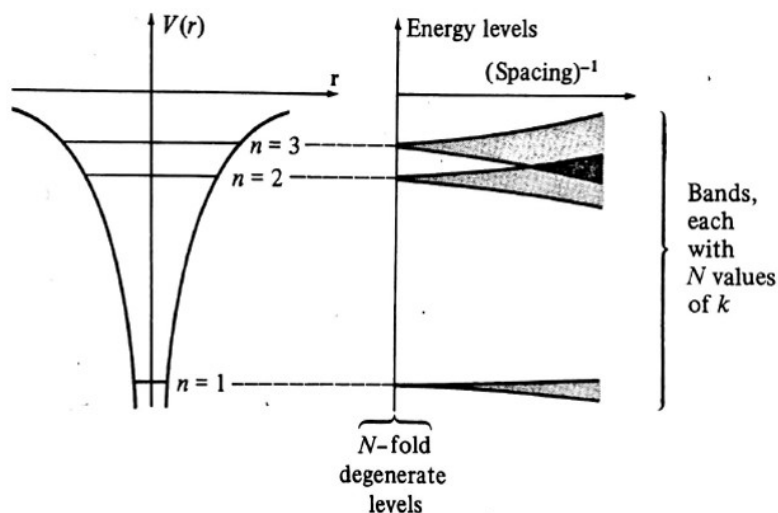
Figure 1.5: Broadening of the energy bands with intermolecular interactions.
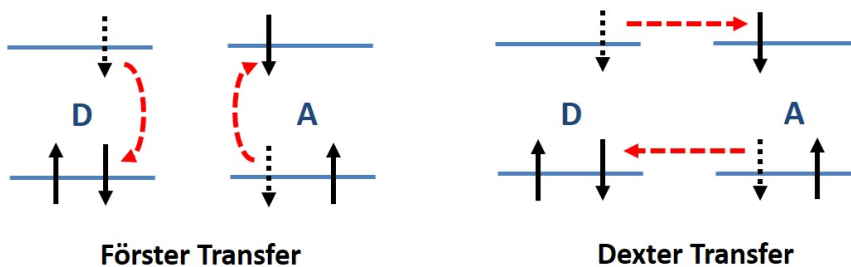
Figure 1.6: Förster and Dexter transfers. D refers to 'donor' and A refers to 'acceptor'.

There are two major types of energy transfer between the organic molecules that describe exciton diffusion: Förster transfer and Dexter transfer, as drawn in Fig. 1.6. Förster transfer, also known as fluorescent resonant energy transfer (FRET), originates from non-radiative resonant dipole-dipole coupling. It possesses a relatively

long transfer distance on the order of 10 nm that depends on r^{-6}. FRET occurs when there is overlap between the donor emission and acceptor absorption spectra, which serves as the main transfer path in organic solar cells. For Dexter transfer, the excited electron is transferred from one molecule to a second through close contact, occurring at a much shorter distance; typically within 1 nm.

1.1.3 Why OPVs are interesting

Solar energy has been one of the most promising renewable energy alternatives to reduce greenhouse gas emissions. The highest solar cell efficiency $\sim 46\%$ is achieved for the concentrated GaInP/GaAs/GaInAs/GaInAs multijunciton cell, as reported by Fraunhofer ISE.[21] The very high fabrication and accessory (concentrators, trackers, cooling systems etc.) costs make it most suitable for high-tech applications such as in space. Crystalline Si solar cells are the most widely utilized solar technology that has been optimized for commercial electricity generation with stable performance. A record single junction efficiency over 26% has recently been demonstrated.[22] Though Si is a very abundant element, the module and the balance of the system (BOS) costs of the solar panels are much higher than the material itself.[23] Moreover, the bulk form factor also limits its use where the flexibility and light weight are important.

Thin film solar technologies are made with layers hundreds of times thinner than silicon solar cells. Among them, amorphous Si (α-Si) offers very low cost but also low efficiency; around 10%. This makes α-Si less competitive with other commercial technologies in the market. α-Si panels are less subject to cracks than crystalline Si, but are not designed for flexible applications. CdTe and CIGS are popular thin film technologies, both of which reach the power conversion efficiencies $> 20\%$.[24,25] However they both contain cadmium, which is one of the most toxic materials to human health, making panel disposal an environmental concern. CIGS can be deposited on the glass or plastic substrates with full-panel flexibility. Its main disadvantage,

however, is the very high production cost. Organic photovoltaics, on the other hand, provide unique features over inorganic thin film PVs including very low cost, flexible and lightweight form factors with transparency to the visible spectrum.[3,26,27]

Low cost

Organic materials, both small molecules and polymers, can be deposited by vacuum deposition or solution processes. Theses low energy processes do not require high temperature resistant substrates, greatly reducing the fabrication costs. Due to the large absorption coefficient and low mobility, the OPV thickness is on the order of several hundred nanometers, leading to a small material consumption. All of these factors make OPV a potentially low cost thin film technology if a competitive efficiency and lifetime can be achieved. In addition, the organic materials for OPV usually only contain the non-toxic elements like C, H, O, S, N, with relatively small environmental impact.

Flexibility
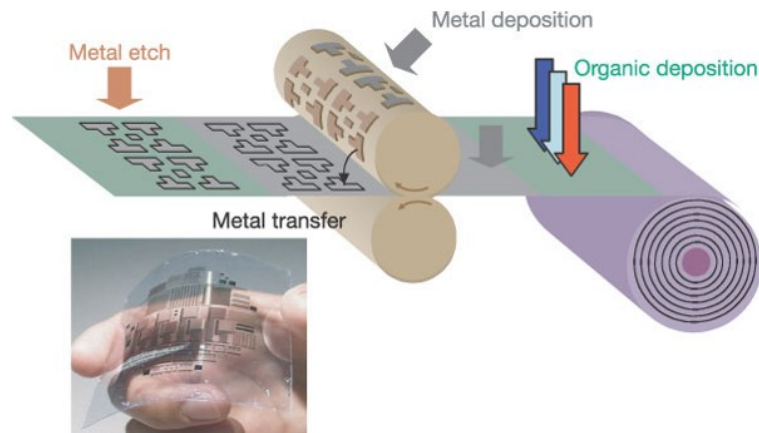
Figure 1.7: Conceptual diagram of the OPV roll to roll fabrication on flexible substrates. Figure from Ref.[26].

OPV cells with ultrathin active layers (usually < 300 nm) can be deposited or printed on a variety of flexible substrates from plastics to metal foils.[28–30] The light weight form factor therefore allows for application to different types of surfaces, such

as the wearable solar fibers on cloth, or solar paints on buildings or cars. Such features also makes it applicable to roll-to-roll (R2R) fabrication[26,31], as illustrated by the conceptual diagram in Fig. 1.7. OPV materials and the metal electrodes are deposited on the moving web through different deposition technologies, such as vacuum thermal evaporation (VTE), organic vapor phase deposition (OVPD)[32], spray coating[33], doctor blade coating[34] etc., all integrated into one system. The production cost can be reduced with the high speed R2R fabrication process.

Semitransparency
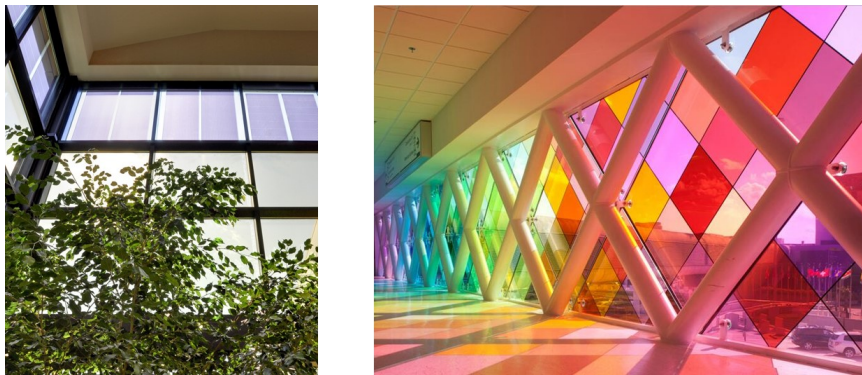
Figure 1.8: Semitransparent OPVs for BIPV applications.

A unique feature of OPVs is that they can be made semitransparent with tunable colors due to the narrow absorption bands of excitons. The opaque metal contact is replaced with the transparent electrode such as indium tin oxide (ITO) or Ag nanowires. With the recent development of non-fullerene acceptors absorbing primarily in the near-infrared (NIR), it is possible to make OPVs almost transparent in the visible below 650 nm while generating power with the absorption in NIR.[30,35] The donor and acceptor absorption ranges and blend ratios can be chosen to achieve neutral or saturated colors, showing great potential in building integrated photovoltaic (BIPV) markets[36,37] for electricity generation as well as decoration purposes, as shown by the examples in Fig. 1.8.

1.2 Concepts and properties of OPVs

1.2.1 Heterojunction

In inorganic solar cells, the n-type semiconductor has a larger free electron concentration than holes. This unbalance is created by doping the intrinsic semiconductor material with electron-rich donor impurities. The p-type semiconductor doped with an acceptor gives a larger free hole concentration. Figure 1.9 (left) illustrates the simplified case for an inorganic p-n junction. The photo-excited electrons flow from the p-type to the n-type material due to the energy offset, while the holes flow with the opposite direction.
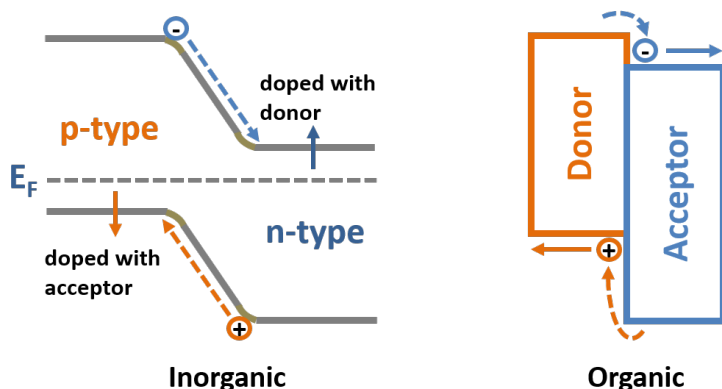
Figure 1.9: Organic vs. inorganic junctions. Definition and working principle (under light) of (Left) The n- and p-type semiconductor in inorganic solar cells. E_F refers to the Fermi level; (Right) The donor/acceptor heterojunction in organic solar cells.

For organics, however, electrons and holes are bonded as excitons with a large energy, leaving almost no free charges. A type-II junction (where the HOMO and LUMO levels of one molecule are both higher than the other) is required for efficient exciton dissociation, as seen in Fig.1.9 (right). We call the material with shallower energy levels (relative to the vacuum) the donor. The other material with deeper HOMO and LUMO levels is the acceptor. With a large enough energy offset, the exciton can dissociate at the donor-acceptor interface, leaving the electrons on the

acceptor side while the holes are left on the donor side. Due to this definition, a donor in one system can also be the acceptor in another. The details of photocurrent generation will be explained below.

1.2.2 Dark current

In the dark, the OPV behaves like a diode. The generalized inorganic Shockley equation based on delocalized free charge carriers, however, cannot be directly applied to the case of organics. Giebink *et al.* developed the ideal diode equation with a picture of polaron pair generation, dissociation and recombination shown by Fig.1.10.[38]
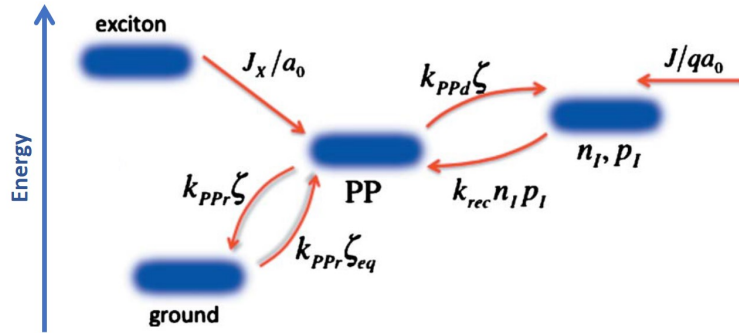
Figure 1.10: Polaron pair related processes in organic heterojunctions.

The exciton diffuses to the donor/acceptor interface and forms polaron pairs (PP), also known as charge transfer (CT) states, with the density of ζ. k_{PPd} refers to the dissociation rate from PP to free electrons and holes, with densities of n_I and p_I, respectively, at the interface, while k_{rec} is the free carrier bimolecular recombination coefficient. k_{PPr} refers to the polaron pair recombination rate back to the ground state, which is also linked to the PP population under thermal equilibrium, with the population of ζ_{eq}. The ideal diode equation for an organic heterojunction (HJ) in absence of the interface traps can be simplified as Eq. 1.11a. Under equilibrium condition, $\frac{k_{PPd}}{k_{PPd,eq}} = 1$.

Molecular disorder in most organic materials broadens the density of states with Gaussian distribution close to the HOMO and LUMO levels. The states at the low energy tail of the distribution can be treated as traps, which leads to an addition recombination mechanism at the interface. Ideality factors n_D and n_A, respectively, for the donor and acceptor materials are therefore introduced, leading to the modified dark current equation in Eq. 1.11b. The five parameters: n_D, J_{sD}, n_A, J_{sA} and R_S, can be fitted from the measured dark current density as a function of voltage.

$$J_{dark}(V) = J_{s0} \left[\exp\left(\frac{V - JR_S}{k_B T/q} \right) - \frac{k_{PPd}}{k_{PPd,eq}} \right];$$

(1.11a)

$$J_{dark}(V) = J_{sD} \left[\exp\left(\frac{V - JR_S}{n_D k_B T/q} \right) - \frac{k_{PPd}}{k_{PPd,eq}} \right] + J_{sA} \left[\exp\left(\frac{V - JR_S}{n_A k_B T/q} \right) - \frac{k_{PPd}}{k_{PPd,eq}} \right].$$

(1.11b)

1.2.3 Photocurrent and external quantum efficiency (EQE)
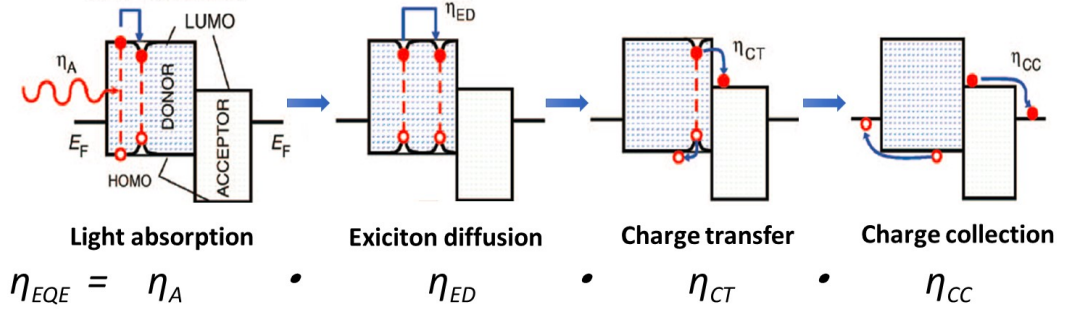
Figure 1.11: Photocurret generation in OPVs and the definition of external quantum efficiency (EQE). Figures from [39].

In Fig. 1.10, J_X is the exciton flux density, generated by photons under illumination. As seen in Fig. 1.11, the photocurrent generation of organic solar cells can be divided into four steps. First, the incoming photons create the molecular excited state - the exciton. It then diffuses toward the junction, where the electrons and holes see a favorable energy gap at the interface between the donor and acceptor materials

and form the charge transfer state. Finally, it dissociates into free polarons that are collected at the respective electrodes.

The external quantum efficiency (EQE) is defined as the ratio of the number of charge carriers collected at the electrodes to the number of incident photons. It is the product of the four efficiencies shown in Fig. 1.11: light absorption (η_A), exciton diffusion (η_{ED}), charge transfer (η_{CT}) and charge collection (η_{CC}). By definition, the photocurrent can be calculated by integrating the EQE over incident light irradiance at each wavelength.

The most widely applied illumination spectrum for reporting solar cell performance is AM 1.5G solar spectrum. The "AM" is the air mass that sunlight needs to travel through before reaching the earth, which is defined as:

$$AM = \frac{1}{cos(\theta)},\tag{1.12}$$

where θ is the zenith angle (see Fig. 1.12). $AM = 1$ if the sun is directly overhead, and $AM = 0$ if it is measured in space before going through the atmosphere. AM 1.5, therefore, corresponds to the latitude of 48°, roughly where Seattle locates.
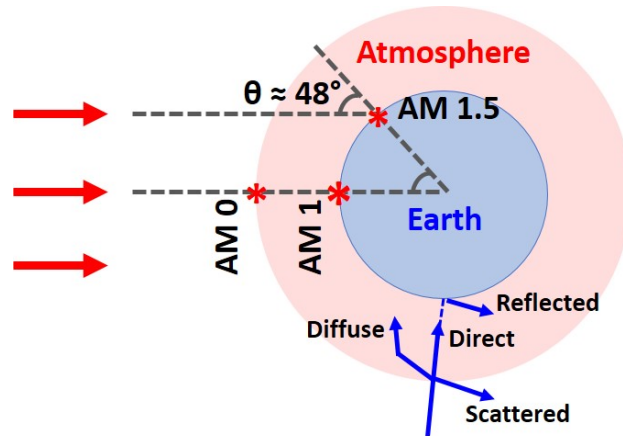
Figure 1.12: The definition of Air Mass (AM). The locations of AM 0, 1 and 1.5 are marked by the red stars.

The "G" or "D" following AM 1.5 refer to "Global" and "Direct" respectively. As

shown by Fig. 1.12, after reaching the earth's atmosphere, some of the solar radiation is scattered, absorbed or reflected out, while the rest of the light either directly reaches (i.e. D) or diffuses to the earth's surface. Global (G) is defined as the total radiation of direct and diffuse, plus the portion that is reflected by the ground. Fig. 1.13 presents the solar irradiance of AM 0, AM 1.5G and AM 1.5D. AM 0 has the highest irradiance intensity and is that of a black body at the sun's surface temperature of 5778 K. AM 1.5G is higher than AM 1.5D, both of which are lower than AM 0 with dips above 900 nm, which is primarily caused by the absorption of water and CO_2 in the atmosphere. The standard OPV cell performance in this dissertation is based on AM 1.5G, 1 sun spectrum with a power density of 1000 W/m^2.
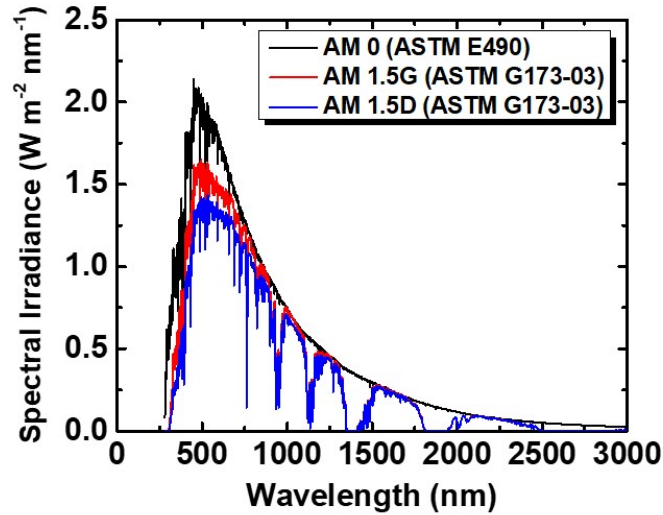
Figure 1.13: AM 0, AM 1.5G and AM 1.5D solar spectral irradiance over wavelength.

With the AM 1.5G spectral irradiance (Φ_P, with the unit of $Wm^{-2}nm^{-1}$) and the measured EQE response, the photocurrent (J_{ph}) generated by the solar cell without voltage bias is:

$$J_{ph} = \int_\lambda \frac{q\Phi_P(\lambda)EQE(\lambda)}{hc/\lambda}d\lambda. \tag{1.13}$$

17

1.2.4 Current density-voltage (J-V) characteristics

A solar cell, either organic or inorganic, is used to generate electric power at forward voltage bias under illumination. Fig. 1.14 shows the J-V characteristics of a solar cell. The three main parameters are short circuit current (J_{SC}), open circuit voltage (V_{OC}) and fill factor (FF).
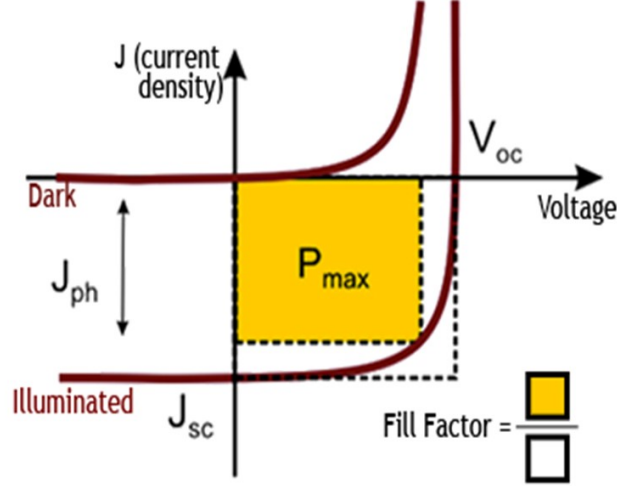
Figure 1.14: Current density-voltage ($J - V$) characteristics and parameters of the solar cells. Figure taken from http://met.usc.edu/projects/solarcells.php

The J_{SC} is defined as the solar cell current density at zero bias voltage. Based on Eq. 1.11b, the dark current is always zero at zero bias under equilibrium. The J_{SC} is therefore the photocurrent, which is determined by the EQE and the incident spectral irradiance as discussed above. When measuring the J-V characteristics under a solar simulator (usually with a Xe light source), there is always a spectral mismatch between the simulator and the actual AM 1.5G solar irradiance. The mismatch factor, M, is used to correct the current generation discrepancy:[40]

$$M = \frac{\int_{\lambda_1}^{\lambda_2} E_R(\lambda)S_R(\lambda)}{\int_{\lambda_1}^{\lambda_2} E_S(\lambda)S_R(\lambda)} \cdot \frac{\int_{\lambda_1}^{\lambda_2} E_S(\lambda)S_T(\lambda)}{\int_{\lambda_1}^{\lambda_2} E_R(\lambda)S_T(\lambda)}, \qquad (1.14)$$

where $E_R(\lambda)$ is the reference spectral irradiance, $E_S(\lambda)$ is the simulator spectral

irradiance, $S_R(\lambda)$ is the responsivity of the reference cell, and $S_T(\lambda)$ is the responsivity of the OPV cell being tested. All the parameters are functions of wavelength (λ) over the range of the solar spectrum detected by the reference or the test cell. It is worth noting that the spectra, $E_R(\lambda)$ and $E_S(\lambda)$, appear both on the numerator and the denominator that cancels out their absolute values. Therefore only the relative spectra are needed to calculate M. With the measured current density ($J_{SC,measured}$) under solar simulator illumination, the actual $J_{SC,corrected}$ is then:

$$J_{SC,corrected} = \frac{J_{SC,measured}}{M}. \tag{1.15}$$

In theory, the J_{SC} corrected by the mismatch factor should be equal to the EQE integrated J_{SC} calculated from Eq. 1.13.

The V_{OC} corresponds to the forward bias applied to the solar cell at zero current, where the dark current and photocurrent are balanced. The FF is defined as the maximum power density generated in the 4th quadrant, P_{max} (the yellow box in Fig. 1.14), divided by the product of J_{SC} and V_{OC} (the white box). The power conversion efficiency (PCE) is therefore:

$$PCE = \frac{P_{max}}{P_{incident}} = \frac{J_{SC} \times V_{OC} \times FF}{P_{incident}}. \tag{1.16}$$

Under AM 1.5G solar irradiation, $P_{incident} = 100 \ mW/cm^2$, leading to a simpler expression: $PCE \ (\%) = J_{SC}(mA/cm^2) \times V_{OC}(V) \times FF$.

1.2.5 Single and multijunciton device structures

Single junction OPVs

A single junction OPV structure as shown in Fig. 1.15 on the left contains an active layer that generates photocurrent, sandwiched by the buffer layers on both cathode and anode sides. The buffers prevent exciton quenching while efficiently

conducting electrons and holes. The OPVs often employ the bottom-illuminated structure where the light enters in from the substrate side. A transparent electrode such as indium tin oxide (ITO) is usually applied to the glass substrate. Metal electrodes such as Ag or Al are deposited on the other side of the device, while they can be replaced by the transparent electrodes for semitransparent applications.
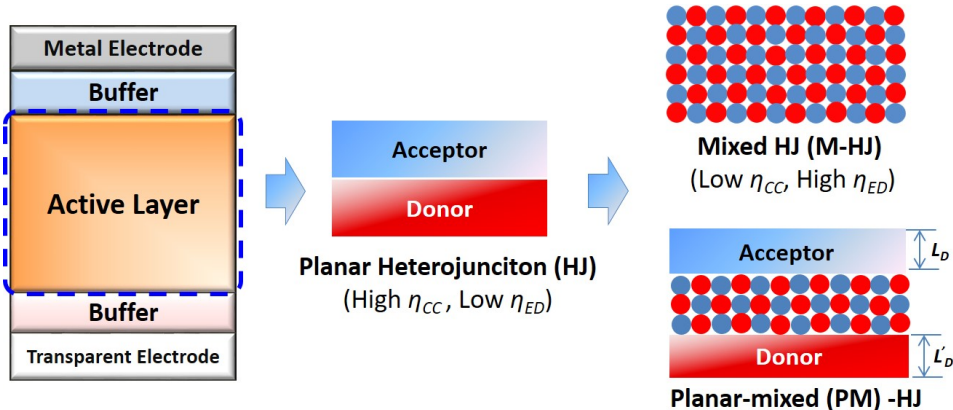
Figure 1.15: Single junction device structures and different types of heterojunctions.

Among the four efficiencies that determines EQE (as discussed in subsection 1.2.3), the light absorption and exciton diffusion are the main limitations. In organic materials, the exciton diffusion length is typically on the order of 10 nm. For active layers with a planar heterojunction (P-HJ) structure as shown in the middle of Fig. 1.15, the layer thicknesses are limited by the exciton diffusion lengths in the donor and acceptor materials, leading to inefficient light absorption.

To mitigate the problem of the short diffusion length, vacuum deposited mixed-heterojunction (M-HJ) for small molecule OPVs has been introduced.[41] The donor and acceptor molecules are mixed in the active region, similar to the bulk HJ structure for polymer cells[42]. Such a structure results in large area of donor-acceptor interfaces within the active layer, improving the exciton diffusion efficiency to ~ 1 that enables a thick active layer for efficient light absorption. On the other hand, compared with the P-HJ structure, the electrons and holes generated in the mixed layer are more

20

likely to meet and recombine on the way to being collected by the electrodes. The donor:acceptor (D:A) ratios and morphologies can be adjusted to optimize the charge collection efficiency. In other cases, a neat layer with the thickness close to the exciton diffusion length is placed adjacent to the mixed HJ, forming the so-called planar-mixed heterojunction (PM-HJ) to further improve the absorption.[43] High efficiency OPV devices in this dissertation are mostly based on the M-HJ while some also comprising PM-HJ structures.

Multijunction OPVs
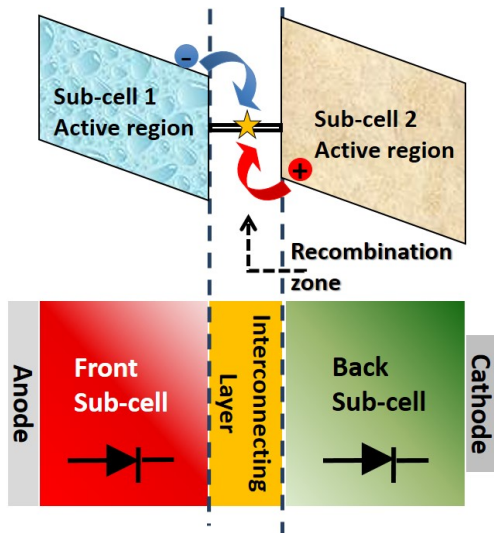
Figure 1.16: Tandem cell working principle with two subcells connected in series.

In single junction OPVs, there is the trade-off between J_{SC} and V_{OC} caused by the thermalization of the excited carriers generated by photon energies greater than the energy gap.[44] The relatively narrow absorption range of organic molecules also limit the current generation. Multijunction OPVs with two or more stacked subcells have been widely used to decrease the thermalization loss, and to give broader spectral coverage. The subcells can be connected in series or in parallel, where the former is more widely employed. Figure 1.16 displays the tandem cell working principle with two subcells connected in series. The subcells absorbing in different wavelength

ranges are connected by a charge recombination zone (CRZ) that balances the current in the tandem stack. The CRZ usually contains an electron-transporting layer, a hole-transporting layer and recombination cites such as metal nano-particles[45]. Ideally, it forms an ohmic contact, acting as a recombination center of electrons and holes. It should also be transparent, and with good charge transport ability, to minimize optical and electrical losses within the stack. A third and fouth subcell can be further added to the stack to improve the performance.

1.3 OPV history and state of the art

1.3.1 A brief history

The concept of organic photodiode was first introduced in 1970s.[46] Tang and Albrecht put a single layer microcrystalline Chlorophyll-a through electrodeposition between two dissimilar metals with different work functions, giving a V_{OC} of 0.5 V and PCE of 0.001 %. In 1986, Tang reported a breakthrough of the vacuum-deposited OPV cell with the bilayer structure: ITO/Copper(II) phthalocyanine (CuPc)/3,4,9,10-perylenetetracarboxylic bis-benzimidazole (PTCBI)/Ag.[47] Instead of the dependence of charge generation on the bias field in single-active layer cells, excitons are dissociated into charges at the interface of the two organic materials. The electrodes therefore simply provide ohmic contact to the organic layers. The P-HJ device achieved a much higher $J_{SC} = 2.3 \pm 0.1$ mA/cm^2, $FF = 0.65 \pm 0.03$, with orders of magnitude higher $PCE \approx 1.0\%$ under 75 mW/cm^2 light illumination.

In order to improve the solar cell internal quantum efficiency as well as to protect the organic layers from damage due to metal deposition, organic exciton blocking layers were introduced adjacent to the electrodes to prevent exciton quenching. In 2000, P. Peumans et al. used Bathocuproine (BCP) between the PTCBI acceptor and the Ag cathode with the structure: ITO/CuPc/PTCBI/BCP/Ag.[48] With ef-

ficient blocking of excitons and good electron transport, the efficiency is improved to 2.4% with a light trapping geometry. The hole transporting layers on the anode side were also introduced in later years, for example, the MoO_3 and poly(3,4-ethylenedioxythiophene)-poly(styrenesulfonate) (PEDOT:PSS).

Historically the efficiency of OPVs has largely been driven by the choice of acceptors. In the 1980s and 1990s, efficiencies using high electron affinity perylene based compounds (for example, PTCBI) were $\sim 2\%$ as discussed above. The vacuum-deposited fullerene C_{60} was first discovered by H. Kroto in 1985 and has been proposed as a photovoltaic material since early 1990s.[49] For quite a long time, however, it escaped the attention of the OPV community, until P. Peumans and S. R. Forrest published the structure with C_{60} as the acceptor material in 2001.[50] A PCE = 3.6% was demonstrated with the structure ITO/PEDOT:PSS/CuPc/C_{60}/BCP/Al under 150 mW/cm^2 AM 1.5G illumination, primarily due to the much longer exciton diffusion length (L_D) of C_{60} compared with PTCBI.

As it has been discussed in the previous section, in order to achieve high exciton diffusion efficiency while maintaining large absorption, M-HJ or PM-HJ device structures are generally used instead of P-HJs (see Fig. 1.15). Such concept was first introduced by A. J. Heeger and coworkers with the phase-separated solution-processed polymer donor-acceptor network blends, so the called bulk heterojunction.[42] A similar idea was employed to the vacuum-deposited small molecule cells also by Forrest *et al.*, which is the M-HJ.[51] The OPV cell with CuPc:C_{60} M-HJ as the active layer achieved a similar $PCE = 3.5\%$ with the P-HJ structure. The J_{SC} was greatly improved to 15.4 mA/cm^2, while the FF was reduced to 0.46 due to the incomplete photogenerated charge collection. Unlike the almost lossless charge transport in homogeneous layers, charge recombination limits the thickness of the mixed layers. Inspired by the structures reported earlier, J. Xue, S. R. Forrest *et al.* further proposed the hybrid PM-HJ.[43] A single junction OPV efficiency of 5.0% was demonstrated

with the mixed $CuPc:C_{60}$ sandwiched in between a neat layer of CuPc and C_{60}.

In more recent years, C_{70} has been generally employed in high efficiency OPVs instead of C_{60} because of its much stronger absorption. The spherical shapes of the fullerenes C_{60} and C_{70}, as well as the easy sublimation by thermal evaporation, render them by far the most commonly used acceptors for vacuum-deposited small molecule OPVs. Similar fullerene molecules, Phenyl-C61-butyric acid methyl ester ($PC_{61}BM$) and Phenyl-C71-butyric acid methyl ester ($PC_{71}BM$), have been used for solution-processed OPVs. By pairing the fullerene acceptors with a range of donors, the OPV efficiency for both vacuum- and solution-processed devices have been improved from 3% to over 10%.

The fullerene-based OPVs went through a bottleneck period several years ago, with the efficiencies stuck at 11-12%.[52] Until most recently, non-fullerene acceptors (NFAs) are widely developed for solution-processed OPVs.[53] The energy levels of the NFAs can be tuned to achieve the desired absorption features towards the NIR while maintaining high V_{OC} and FF. The NFAs have therefore opened a new avenue for improved optical coverage and energetic pairing with a wide diversity of donor molecules that have been developed over this same period, pushing the OPV efficiency to a new level.

1.3.2   State of the art

Single junction OPVs

The most efficient single junction VTE cell to date is achieved by the DTDCPB:C_{70} M-HJ, with $PCE = 9.6\%$.[54] It shows photoresponse onset of 800 nm with $V_{OC} = 0.92$ V. Another molecule iBuBTDC with similar absorption range also exhibits $PCE > 9\%$ when mixed with C_{70}.[55] These two donor molecules both bearing the donor-acceptor-acceptor' (d-a-a') structure will be discussed in Chapters III and IV. An efficiency of 10.2% for DTDCPB:C_{70} is achieved with a thicker active layer. A NIR-

absorbing VTE cell with absorption beyond 900 nm, on the other hand, has not achieved such high efficiency. DTDCTB has been one of the few high efficiency NIR-absorbing vapor-deposited donors reported, giving $PCE = 5.3\%$ when mixing with C_{60}[56] and 8.0% with C_{70}[54]. The recently published VTE NIR-absorbing donor slightly improved the efficiency to 6.1% when mixed with C_{60}.[57]

Solution-processed OPVs have developed more rapidly than VTE cells with a larger material base - both small molecules and polymers. Small molecule-based solution-processed cells have achieved the highest efficiency similar with that of the VTE cells $\sim 10\%$[58], while the highest PCE reported for the polymer cells with fullerene acceptors is 11.7% processed from hydrocarbon solvents.[52] Recent developments of NFAs has pushed the single junction efficiency to 14% by pairing a polymer donor with a small molecule NFA.[59] More importantly, by flexibly adjusting the energy levels, the NFA-based devices are able to absorb deeper into the NIR while maintaining a similar V_{OC}. The NFAs with energy gaps < 1.4 eV have been reported with PCEs > 11%,[35,60] which is much higher than the fullerene-based cells in the same category. Ternary structures with two donors and one acceptor, or one donor and two acceptors mixed in the active layer is another approach to improve OPV efficiency. The absorption of the ternary system can be improved over the binary structures without sacrificing V_{OC} and FF. The ternary cell with $PCE = 12.2\%$ has been reported.[61]

Multijunction OPVs

Multijunction cells have been demonstrated to further improve the performance over single junction OPVs by reducing the thermalization loss as well as covering a broader solar spectrum with two or more subcells.[62,63] Most multijunciton work reported has a series connection configuration with two terminals. The all vacuum-deposited tandem and triple junction cells with subcells showing minimal absorption overlap was reported in 2014 with efficiencies of 10.0% and 11.1% respectively[64]

(see Chapter V). A similar VTE tandem efficiency of 9.9% was reported in 2017.[57] Further improvement of VTE multijunctions have been largely limited by the NIR-absorbing subcells. Heliatek announced a 13.2% efficient vacuum-deposited tandem OPV in 2016, although no details of the structure or measurement are available.

Similar to the case for single junction cells, solution-processed multijunction efficiency has increased apace. Fullerene-based tandem structures with efficiencies $\sim$ 10-11% were published around 2014,[65–68] improving to $PCE = 12.3\%$ in 2017.[69] A tandem with double NFA-based subcells was reported recently with $PCE = 13.1\%$.[70] Very recently, by pairing a NFA-based NIR-absorbing subcell and the DTDCPB:C_{70} green-absorbing VTE subcell, we have been able to achieve the milestone efficiency of 15%, an important step towards OPV commercialization. The details of this work will be presented in Chapter VI.

Besides efficiency, the lifetime and cost are two other important factors that determines the feasibility of a solar technology. A lifetime span of 10 to 20 years with $< 20\%$ efficiency degradation has been achieved by OPV (ongoing project modified from previous work[71]). It has also been demonstrated with the R2R fabrication for low cost mass production.[31] The focus of this dissertation, though, will only be on developing high efficiency OPVs. An introduction of device simulation is presented in Chapter II. It is followed in Chapters III and IV, where the single junction OPV cells with d-a-a' vacuum-deposited donors are studied for a better understanding of the structure-property-performance relationships. Chapters V and VI are the core chapters with the works on high efficiency multijunction cells, achieving $> 10\%$ and 15% PCEs. The practical efficiency targets based on calculations will be discussed in the last chapter (VII), with an outlook of the OPV technology presented.

CHAPTER II

Device Performance Simulation

In order to achieve single or multijunction OPV cells with high efficiencies, a simulation tool is essential to predict the device performance. A reliable simulation method can serve as a guide for device structure design without doing extensive experiments. It becomes more important for multijunction structures. Here we introduce the optical simulation method. The single junction absorption is calculated based on the transfer matrix method, from which the photocurrent can be derived. For a tandem or multijunction cell, the J-V characteristics are calculated by adding up the input subcell J-V curves under a given absorbed light intensity. Each of the simulation steps will be explained in detail in this chapter.

2.1 Transfer matrix method

The transfer matrix method is used to determine the absorbed power of each thin film layer as a function of wavelength at each position.[2] A structure example is shown in Fig. 2.1 comprising m layers with the thicknesses d_1, d_2, $\cdots$, d_m grown on an optically thick substrate. The absorption of each assumed isotropic layer can be described by a complex index of $\bar{n}$, that $\bar{n}_j = n_j + i \cdot k_j$. The substrate is usually much thicker than the incident light wavelength, which needs to be treated separately from the thin film layers. The reflection (R^*) and transmission (T^*) at the air/substrate
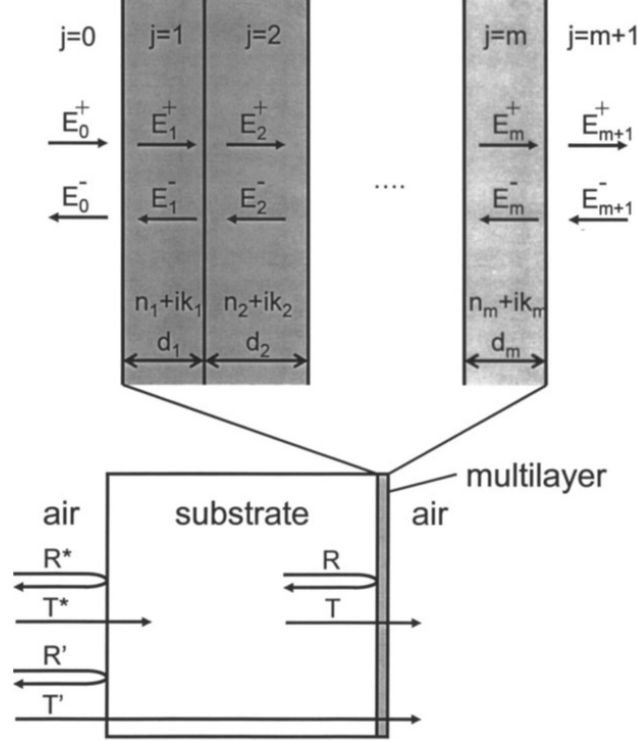
Figure 2.1: Geometry of the multilayer stack used in electric field calculations by transfer matrix method. Layers 0 and m+1 are the transparent substrate and air. Figure from Ref.[2].

interface is:

$$R^* = \left|\frac{1 - \bar{n}_0}{1 + \bar{n}_0}\right|^2 ; \qquad T^* = \frac{4\bar{n}_0}{|1 + \bar{n}_0|^2}, \tag{2.1}$$

where $\bar{n}_0$ is the refractive index of the substrate. If the reflection (R) and transmission (T) at the substrate/thin film-1 interface is calculated, the overall reflection (R') and transmission (T') can then be written as:

$$R' = \frac{R^* + R}{1 + R^* R}; \qquad T' = \frac{T^* T}{1 + R^* R}. \tag{2.2}$$

Within each layer, the electric field along the positive and negative propagation directions perpendicular to the layer interface are $\bar{E}^+$ and $\bar{E}^-$, respectively. At the interface between layers j and k, the electric field is related by the 2 × 2 interface matrix I_{jk}:

28

$$
\begin{bmatrix} \overline{E}_j^+ \\ \\ \overline{E}_j^- \end{bmatrix} = I_{jk} \begin{bmatrix} \overline{E}_k^+ \\ \\ \overline{E}_k^- \end{bmatrix} = \begin{bmatrix} \frac{1}{t_{jk}} & \frac{r_{jk}}{t_{jk}} \\ \\ \frac{r_{jk}}{t_{jk}} & \frac{1}{t_{jk}} \end{bmatrix} \begin{bmatrix} \overline{E}_k^+ \\ \\ \overline{E}_k^- \end{bmatrix}, \tag{2.3}
$$

where r_{jk} and t_{jk} are the Fresnel complex reflection and transmission coefficients:

$$
r_{jk} = \frac{\overline{n}_j - \overline{n}_k}{\overline{n}_j + \overline{n}_k}; \qquad t_{jk} = \frac{2\overline{n}_j}{\overline{n}_j + \overline{n}_k}. \tag{2.4}
$$

Also considering the phase shift marked by the matrix L_j:

$$
L_j = \begin{bmatrix} e^{-i\xi_j d_j} & 0 \\ \\ 0 & e^{i\xi_j d_j} \end{bmatrix}; \qquad \xi_j = (2\pi/\lambda)\,\overline{n}_j, \tag{2.5}
$$

the electric field relation between layer 0 and layer $m+1$ can be described by the transfer matrix S:

$$
\begin{bmatrix} \overline{E}_0^+ \\ \\ \overline{E}_0^- \end{bmatrix} = S \begin{bmatrix} \overline{E}_{m+1}^+ \\ \\ \overline{E}_{m+1}^- \end{bmatrix}, \quad S = \begin{bmatrix} S_{11} & S_{12} \\ \\ S_{21} & bS_{22} \end{bmatrix} = \left(\prod_{n=1}^{m} I_{(n-1)n}L_n \right) \cdot I_{(m+1)m}. \tag{2.6}
$$

The reflection (R) and transmission (T) at the substrate/thin film 1 interface are then:

$$
R = |r|^2 = \left| \frac{S_{21}}{S_{11}} \right|^2; \quad T = |t|^2 \cdot \frac{\overline{n}_{m+1}}{\overline{n}_0} = \left| \frac{1}{S_{11}} \right|^2 \cdot \frac{\overline{n}_{m+1}}{\overline{n}_0}. \tag{2.7}
$$

With R* and T* calculated from Eq. 2.1, and R and T calculated from Eq. 2.7, the overall R' and T' including the substrate and thin films can be calculated from Eq. 2.2.

From Eqs. 2.3 to 2.6, the time averaged absorbed power can be expressed as a function of position along the thin film stack:

$$Q_j(x) = \frac{4\pi c \varepsilon_0 k_j n_j}{2\lambda} \left| \overline{E_j}(x) \right|^2, \tag{2.8}$$

where $c = 3 \times 10^8 \ m/s$ is the speed of light, $\varepsilon_0 = 8.85 \times 10^{-12} F/m$, and the electric field of each layer is the sum of the ones propagating in the positive and negative directions:

$$\overline{E}_j(x) = \overline{E}_j^+(x) + \overline{E}_j^-(x) = (t_j^+ e^{i\xi_j x} + t_j^- e^{-i\xi_j x})\overline{E}_0^+. \tag{2.9}$$

For the expression of t_j^+ and t_j^- please refer to Ref.[2] The transfer matrix Matlab code is uploaded on http://umich.edu/~ocm/research.html.

2.2   Single junction simulation

Previous to the simulation, the wavelength-dependent refractive index n_j and extinction coefficient k_j of each layer in the single junction stack need to be measured by ellipsometer and input into the MATLAB program. Based on the transfer matrix method discussed in the previous section, the absorbed power $Q_j(\lambda)$ (Eq. 2.8) at each position (x) in the stack is calculated, which leads to the exciton generation rate:

$$G_j(\lambda, x) = (\lambda/hc)Q_j(\lambda, x). \tag{2.10}$$

In order to calculated the EQE, we will need to know the exciton diffusion, dissociation and charge extraction efficiencies besides the absorption (refer to Fig. 1.11). The OPV cells with active layers of planar or mixed HJs are therefore calculated in different ways.

2.2.1   Cells with planar heterojunction (P-HJ) structures

The OPV cell with a P-HJ active layer contains neat donor and acceptor layers. The exciton dissociation and charge extraction efficiencies are close to 100%, while

the EQE is mainly limited by exciton diffusion. The steady state exciton diffusion in each of the two layers can be solved by:

$$L_D{}^2\frac{\partial^2 n}{\partial x^2} - n + \tau G = 0; \qquad L_D = \sqrt{D\tau}, \tag{2.11}$$

where n is the exciton density, L_D refers to the exciton diffusion length of the donor or acceptor material, D is the exciton diffusivity, and τ is the exciton lifetime. L_D and τ of the donor and acceptor are input into the program. For example, the L_D for the acceptor C_{60} and C_{70} are about 25 nm and 11 nm respectively, while for small molecule donors it is usually < 10 nm.
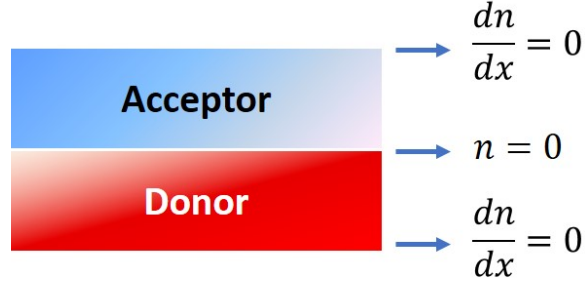
Figure 2.2: Boundary conditions of the P-HJ structure.

The exciton diffusion equation is then solved for the donor and acceptor layers, with the boundary conditions shown by Fig. 2.2. Here, n = 0 refers to the quenching donor/acceptor interface where exciton dissociation occurs. While dn/dx = 0 is the non-quenching boundary with no surface recombination velocity, applied to the interface between the active layer and the buffer blocking layers. For buffers like MoO_3, a partial quenching boundary can be assumed to better match with the actual device performance. After solving Eq. 2.11 with the proper boundary conditions, the photocurrent generated as the excitons diffuse towards the donor-acceptor (D-A) interface is then:

$$J_{ph} = q\frac{L_D^2}{\tau}\left|\frac{\delta n}{\delta x}\right|_{x=x_{DA}}; \qquad J_{ph,device} = J_{ph,donor} + J_{ph,acceptor}. \tag{2.12}$$

Finally, the EQE of the device is calculated by:

$$EQE = \frac{J/q}{\frac{1}{2}c\varepsilon_0 \left|\overline{E}_0^+\right|^2}; \qquad EQE_{device} = EQE_{donor} + EQE_{acceptor}, \qquad (2.13)$$

where $\overline{E}_0^+$ is the incident electric field of the AM 1.5G solar spectrum.

Therefore, with the optical constants (n,k) and thickness of each layer in the OPV stack as well as the donor and acceptor exciton diffusion lengths as inputs, the EQE of bilayer devices can be calculated based on the transfer matrix method and exciton diffusion equation. In situations when the EQE is known, the exciton diffusion lengths can be fitted.

2.2.2   Cells with mixed heterojunction (M-HJ) structures

For the P-HJ device, we assume 100% exciton dissociation and charge collection as an approximation. However, it is different for the devices with M-HJs, which are more widely used for high efficiency OPVs. As discussed in Section 1.2.1, excitons experience rapid dissociation with a short diffusion path towards the donor/acceptor interfaces in the blend active layers. It is therefore reasonable to assume 100% exciton diffusion and dissociation efficiencies. On the other hand, the charge collection efficiency (η_{cc}) can be significantly lower than 100%. Therefore, η_{cc} needs to be input as a known or fitting parameter for M-HJ OPV optical simulations, independent of the wavelength.

The η_{cc} of OPV cells can be measured by reverse voltage-biased EQE. With the large build-in field at reverse bias, electrons and holes are extracted with an efficiency close to 100%, while the absorption is independent on voltage. The EQE signal will increase with the reverse voltage before reaching a maximum. Figure 2.3 shows an example of an OPV cell charge collection efficiency measurement, in which case the EQE reaches the highest value at $\sim$ -3.5 V. The η_{cc} is then calculated by dividing

the EQE value at each wavelength with 0 V by the value with -3.5 V. It is almost a constant ~ 0.8 independent of the wavelength, which is a common value for M-HJ OPV cells.
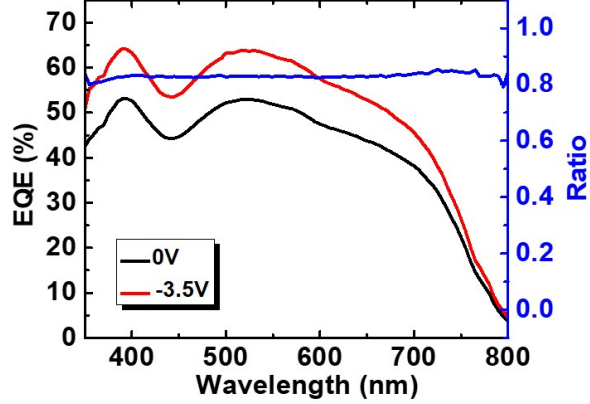
Figure 2.3: An example of the M-HJ charge collection efficiency measured by reverse voltage-biased EQE.

Similar to the bilayer structure, the exciton generation profile as a function of wavelength and position is first calculated using transfer matrices. It is then assumed that all excitons generated in the blend D:A layer are dissociated into free carriers. Or equally, we can set the exciton diffusion length (L_d in Eq. 2.11) to infinity. The current density calculated is then corrected by multiplying η_{cc} to get the final value. Finally, the EQE is obtained by Eq. 2.13 (without separating the donor and acceptor contributions).

Unlike the exciton diffusion efficiency input for the P-HJ simulation that only depends on the donor or acceptor material, the η_{cc} of the blend is sensitive to the layer thickness. Figure 2.4 shows the fitted η_{cc} as a function of the active layer thickness of a M-HJ OPV cell. With each thickness, the current density is measured ($J_{SC,Meas}$) and total current generated in the active layer ($J_{SC,Gen}$) is calculated assuming 100%
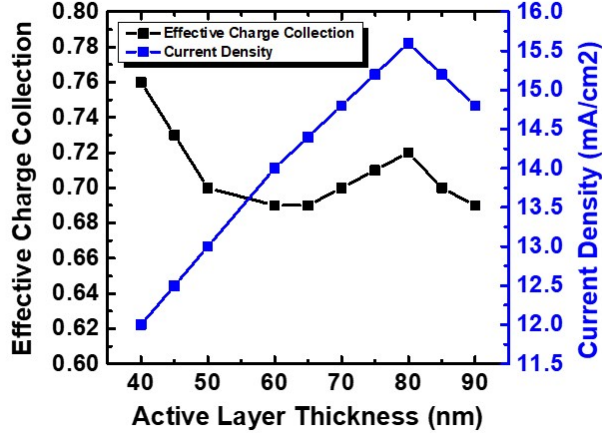
Figure 2.4: Fitted charge collection efficiency as a function of M-HJ active layer thickness.

charge collection. The effective η_{cc} is defined as:

$$\eta_{cc,eff} = \frac{J_{SC,meas}}{J_{SC,Gen}} \tag{2.14}$$

As the DTDCPB:C$_{70}$ (1:1) layer thickness increases from 40 nm to 90 nm, the $\eta_{cc,eff}$ decreases sharply from 0.76 to 0.70 and fluctuates between 0.68 and 0.72. The measured J_{SC} increases with the thickness due to higher absorption, and reaches the highest value at 80 nm, after which the absorption increase is smaller than the charge collection loss. The single junction simulation tool for devices with M-HJ active layers therefore can also be used to calculate the effective charge collection efficiency if the measured J_{SC} is known. Optimizing active layer blend ratios and growth conditions can be helpful to improve the charge collection efficiency especially for thick films.

From the above descriptions, the exciton diffusion and charge collection efficiencies are input parameters for the neat and mixed active layers, respectively, used to calculate the device EQE and J_{SC}. The layer thicknesses can be adjusted in the simulation to achieve the highest J_{SC}. On the other hand, the optical simulation cannot predict the FF, and the charge collection efficiency for M-HJ cells may vary

with thickness. Nevertheless, it is a usefully tool to optimize the devices structure for single junction cells, providing important guidance for experiment.

2.3   Multijunction simulation

The optical simulation plays an important role in single junction device optimization that saves time and materials. When coming to multijunctions with more layers and design possibilities, it becomes more and more difficult to try all thickness combinations by experiment. A good *EQE* and *J-V* characteristics prediction by simulation is therefore even more critical for multijunction designs.

2.3.1   Device performance simulation
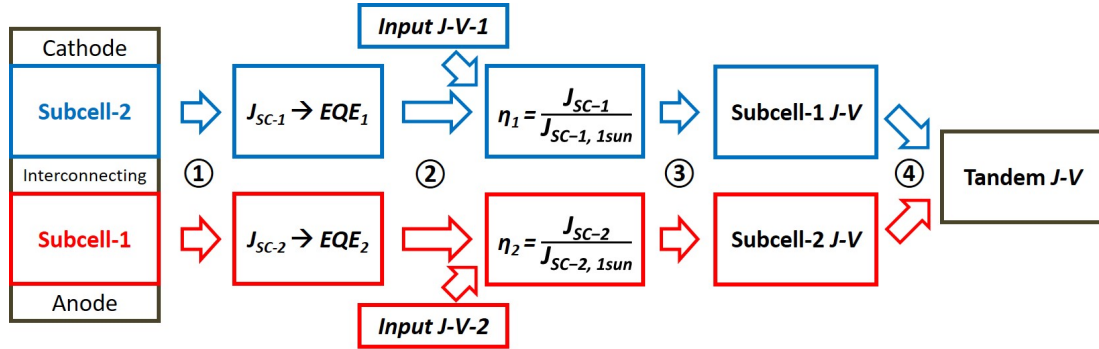
Figure 2.5: Multijunction simulation flow.

The simulation flow for multijunction cells is summarized in Fig. 2.5 containing four steps. The absorption profile of the subcells in the tandem or multijunction stack is simulated the same way as for the single junction cell. Taking a tandem cell as an example, the measured optical constants n and k for each layer are first used to calculate the J_{SC} and EQE generated in each subcell by the transfer matrix method and the relationship in Eq. 2.13. The quantum efficiency of the tandem cell is defined as the sum of EQEs of the two subcells. In order to simulate the tandem *J-V* characteristics, the *J-V* characteristic for each subcell at different light intensities

35

(several data sets between 0 and 1 sun) need to be input. As shown by step 2, the effective light intensity (η) is taken as the ratio between the calculated subcell J_{SC} in the tandem stack and the input measured 1 sun J_{SC} of the same subcell. The η value is usually between 0.5 to 0.8 sun due to the absorption overlap between the subcells. We can then get the subcell J-V characteristics in the tandem stack by interpolating the input J-V at the effective light intensities.
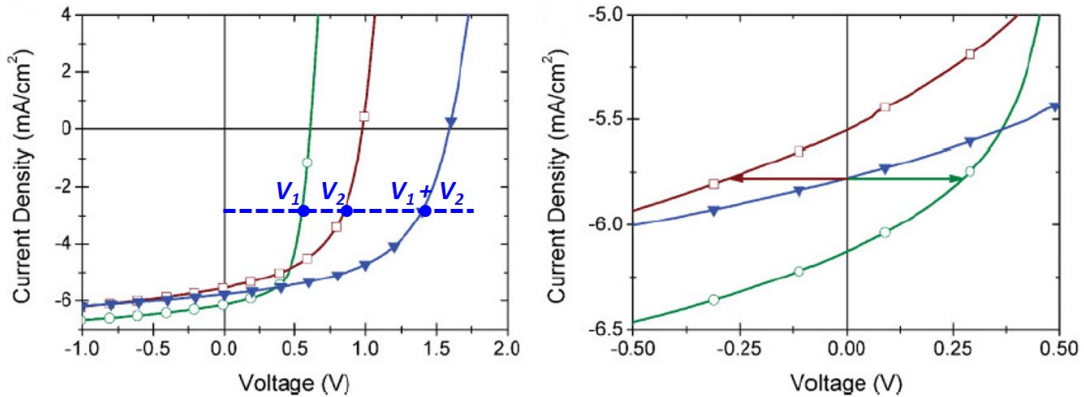
Figure 2.6: Tandem J-V characteristic simulation: (Left) Adding up the subcell voltage at each current; (Right) Zoom-in of the short-circuit region. Figures from Ref[72].

Finally, the J-V characteristic of the tandem cell is generated by adding up the subcell J-V characteristics. For the two subcells connected in series, at each current density the tandem voltage is the sum of the two subcells, as indicated by the blue dashed line in Fig. 2.6, left. The tandem parameters including efficiency can be obtained from the J-V curve. Figure 2.6 (right) shows the detailed characteristics near zero voltage. The current-limiting subcell works at a reverse voltage bias while the subcell with larger J_{SC} works at a forward bias. The tandem J_{SC} therefore usually lies in between the two subcell J_{SC} at a total voltage of 0 V. The EQE and J-V simulations of the multijunction cells with more than two subcells follow the same procedure as the tandem cell.

2.3.2 Contour algorithm
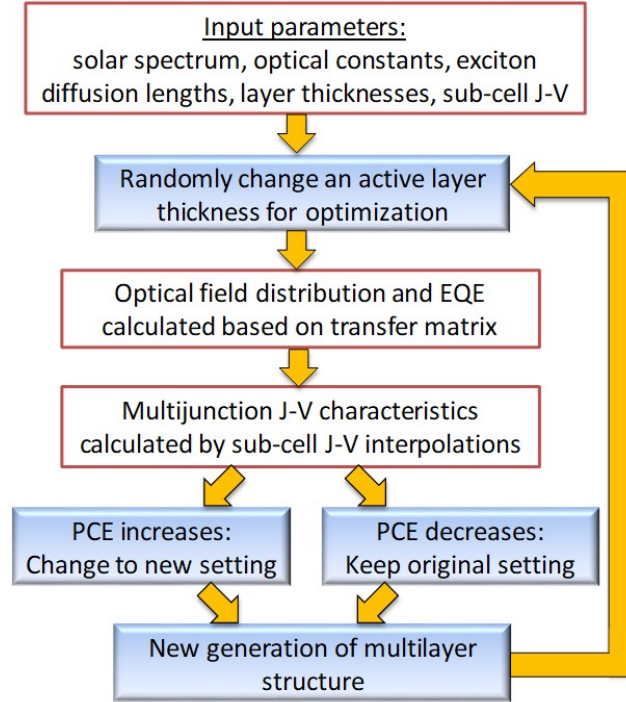
Figure 2.7: Simulation contour algorithm for optimizing multijunction cells.

The ultimate goal of the multijunction simulation is to find the approximate op-
timized layer thicknesses especially for the active layers of each subcell. It can be
done more efficiently with the contour algorithm shown in Figure 2.7. As already dis-
cussed, the solar spectrum, optical constants of all constituent layers, exciton diffusion
length and initial thickness for each layer, as well as the sub-cell *J-V* characteristics
at different light intensities are input at the beginning of the optimization cycle. An
active layer thickness in the multijunction stack is randomly changed by a value for
every calculation cycle. The optical field distribution and quantum efficiency are
calculated based on the transfer matrix method. The *J-V* characteristics of the tan-
dem or triple-junction cell are then calculated by interpolating the input sub-cell *J-V*
data. The power conversion efficiency is obtained from the calculated *J-V* curve. If
it increases compared with the previous calculated value, the structure is changed to
the new setting, otherwise they are kept at their original thickness values. The new

generation of device structure is then re-optimized through iteration, until the highest output efficiency becomes stable after hundreds of calculation cycles. The thickness step change each time is carefully designed to avoid trapping at local maxima.

2.4 An example
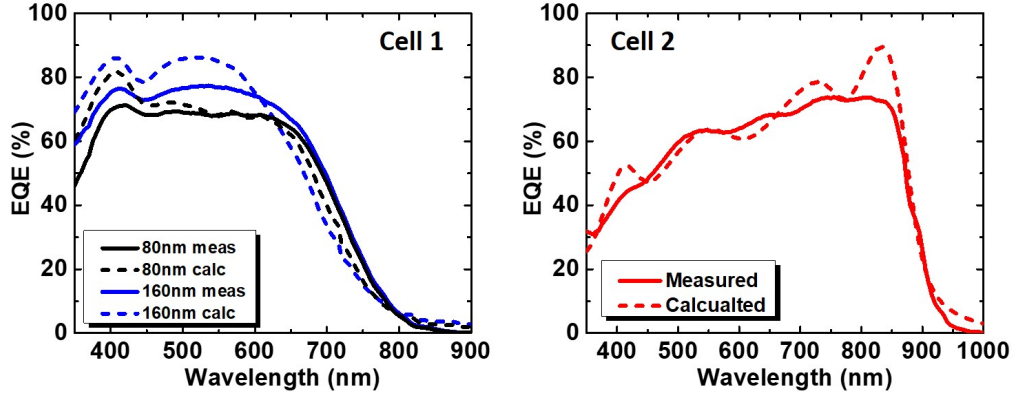
Figure 2.8: Optical simulation example of single junction cell: calculated and measured *EQE* of green- (left) and NIR-absorbing (right) single junction cells.

Here we show an example of tandem cell simulation with the above methods. The details of this tandem structure will be discussed in Chapter VI. For now, we call the green-absorbing cell "Cell 1" and the NIR-absorbing cell "Cell 2", both of which employ the M-HJ structure. The measured *EQE*s of single junction cells 1 and 2 are shown by the solid lines in Fig 2.8. With measured n and k values of each layer, the J_{SC} and *EQE* of the single junction cells are calculated based on the transfer matrix method with input charge collection efficiencies. Here the effective η_{CC}s of Cells 1 and 2 are assumed instead of measured, to match the calculated J_{SC} with measurement values. The simulated *EQE* curves of the two cells are displayed in Fig 2.8 as dashed lines.

For Cell 1 with 80 nm active layer thickness, the calculated curve almost overlaps with the measurement, except for the low wavelength below 450 nm that shows a
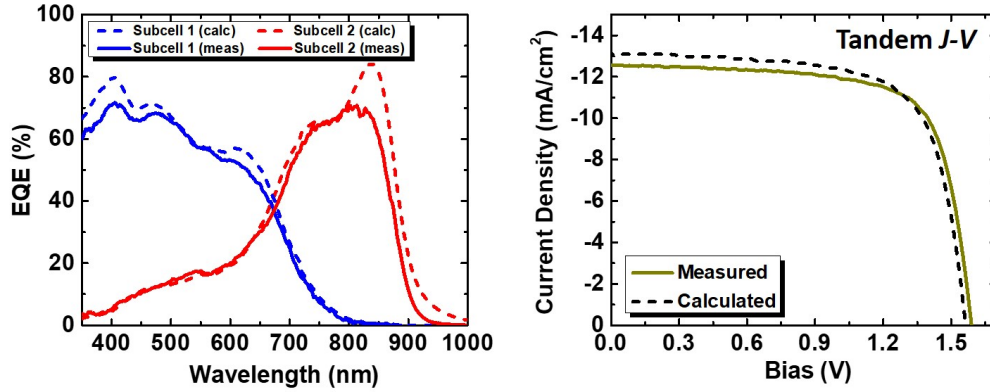
Figure 2.9: Optical simulation example of tandem cell: *EQE* and *J-V* characteristics simulation and measurement of the tandem and its subcells.

higher peak. As the thickness increases to 160 nm, the mismatch between the simulation and experiment gets larger. The simulation shows a higher photoresponse below 600 nm and a lower response above 600 nm as indicated by the blue dashed line in Fig. 2.8 left. For the NIR-absorbing cell, the calculated *EQE* roughly matches with the measured curve, except for a sharp peak from 800 to 850 nm. The device performance of the tandem cell comprising the two subcells (Cell 1 as the front cell and Cell 2 as the back cell) is than simulated with the input of the fitted η_{CC}s from the single junction calculation and the single junction *J-V* characteristics under different light intensities. Figure 2.9 on the left displays calculated and measured *EQE*s of the subcells in the tandem stack. Subcell 1 here has the active layer thickness of 160 nm. The calculated *EQE* discrepancy is smaller than the single junction shown in Fig. 2.8 left.

In the simulation, we assume isotropic materials and perfect interfaces between adjacent layers. In reality, the organic material absorptions are usually anisotropic, that the fitted optical contacts n and k may vary with different fitting models. Also, the films always have certain roughnesses, especially for ITO as well as the cathode with metal diffusing into the organic layers underneath. All of these factors account for the calculation uncertainties. The mismatch at ~ 400 nm for subcell 1 and ~ 850

nm for subcell 2 is likely due to the fitting error of the anisotropic optical constants. For subcell 1, it turns out the calculated photoresponse is also more sensitive to the active layer thickness especially with a metal reflector. The variation of actual grown film thicknesses and blend ratios can also cause the discrepancies.

Table 2.1: Simulated vs. calculated tandem cell performance.

Device	J_{SC} (mA/cm^2)	V_{OC} (V)	FF	PCE $(\%)$
Measurment	12.6 ± 0.3	1.58 ± 0.01	0.72 ± 0.01	14.3 ± 0.3
Calculation	13.1	1.57	0.70	14.5

Figure 2.9 on the right compares the simulated and measured tandem J-V characteristics with the data listed in Table 2.1. The simulation gives $\sim 4\%$ relative higher J_{SC} and lower FF, with $PCE = 14.5\%$ compared with the measured $PCE = 14.3 \pm 0.3\%$. It shows that though with small mismatches, the calculation methods of single junction and tandem cells introduced in this chapter can well predict the device performance thus provide guidance of structural designs especially for multi-juncitons. Further modifying layer parameters of the electrodes, and adjusting the anisotropic optical constant fitting models of the active layers are essential to improve the simulation accuracy.

CHAPTER III

Donor-acceptor-acceptor' (d-a-a') Small Molecule Donors with Propeller Donor Units

In this and the subsequent chapter, we present a group of vacuum-deposited small molecule donors bearing the structure of donor-acceptor-acceptor' (d-a-a'). The relatively large ground state dipole moment of the d-a-a' donors tends to enhance both the intra- and inter-molecular charge transport, improving the OPV performance compared with the traditional non-polar donor molecules. This chapter will focus on the d-a-a' molecules with propeller donor units based on triphenylamine, while Chapter 4 will discuss the d-a-a' donor molecules with coplanar donor groups.

3.1 Background

3.1.1 The emerging of d-a-a' small molecules

For vacuum deposited small molecule donors, it was once believed that the dipolar groups in the molecule were likely to generate a random electrostatic potential in the solid-state film, which hindered charge percolation due to energetic disorder.[73] However, recent works have shown that molecules with relatively large dipole moment generally lead to more favorable exciton and charge transport pathways. At the single molecule level, the electron-donating group (d) and the electron-withdrawing group

(a) can be chemically as well as specially manipulated to achieve a desired degree of intramolecular charge transfer, which determines the absorption strength and energy levels. In the bulk or at the supramolecular level, molecules with large dipolarity along the backbone tend to pack into an anti-parallel dimeric configuration with a net dipole moment of zero, which leads to a short intermolecular cofacial distance that facilitates charge-hopping.[74] It also favors the homo-aggregation of donor molecules in the mixed active layer for improved phase separation. Recently, a large number of vacuum-deposited small molecules with donor-(π-bridge)-acceptor (d-π-a) and donor-acceptor-acceptor' (d-a-a') configurations have been published with high efficiencies, most of which originated at the group of Prof. K.-T Wong at National Taiwan University. These molecules with long rod-like shapes tend to align their backbone axes parallel to the substrate surface, leading to a high in-plane extinction coefficient and efficient vertical charge transport.

In 2011, a d-π-a donor material TPDCDTS was synthetized with a coplanar diphenyl-substituted dithienosilole (DTS) π-conjugated spacer connecting the triphenylamine electron-donating block and the dicyanovinyl (DCV) electron-withdrawing block. The π-bridge enhanced the electronic coupling between 'D' and 'A' units within the molecule thus effectively lowers the energy gap. The TPDCDTS:C_{70} device with MoO$_3$ as the anode buffer exhibited $PCE = 3.8\%$.[75] Another set of triphenylamine-π-DCV small molecules, DTTh and DTTz, were reported by T.Seo and his colleagues, taking thienothiophene-thiophene and thienothiophene-thiazole as the π-conjugation linkers respectively. The thiazole unit of DTTz facilitates intramolecular charge transfer and intermolecular packing, leading to a higher device efficiency of 6.2% compare with 5.4% of DTTh.[76]

The donor molecules employing d-a-a' structures were also first reported in 2011.[77] Compared with the d-π-a structure, their double acceptors with strong electron-withdrawing feature tend to reduce the energy-gap while maintaining a deep HOMO

level. Higher absorption towards the NIR as well as a relatively large V_{OC} can therefore be obtained simultaneously. Among the d-a-a' donor molecules reported, the most efficient ones for NIR-absorbing and green-absorbing OPVs are DTDCTB and DTDCPB, respectively.

3.1.2 DTDCTB and DTDCPB

For DTDCTB, the ditolylaminothienyl and DCV were taken as the end d and a' groups. Instead of a π-block, another 2,1,3-benzothiadiazole acceptor was inserted in between as the middle bridge. As confirmed by X-ray crystallography, the thiophene in the ditolylaminothienyl unit and the benzothiadiazole rings exhibit coplanar confirmation with a small dihedral angle of 5.5°, favorable for intramolecular charge transfer. The DTDCTB cells exhibit absorption up to 900 nm, with the HOMO level lying at -5.3 eV. The device with the PM-HJ structure: ITO/MoO$_3$ (30 nm)/DTDCTB (7 nm)/DTDCTB:fullerene (1:1, 40 nm)/fullerene/BCP (10 nm)/Ag (150 nm) achieved V_{OC} = 0.80 V, PCE = 4.4% and V_{OC} = 0.79 V, PCE = 5.8% when pairing with C$_{60}$ or C$_{70}$ as the fullerene acceptor.[77] The DTDCTB devices were further optimized to obtain better performance: a thin layer of calcium was inserted in between the BCP and Ag, increasing the FF of the DTDCTB:C$_{60}$ cell from 0.50 to 0.55 with the PCE improved to 5.3%;[56] The 1,3,5-Tri(m-pyridin-3-ylphenyl)benzene (TmPyPB) was introduced as the cathode buffer with higher electron mobility compared with BCP that improved the DTDCTB:C$_{70}$ efficiency to 6.1 ± 0.2% with FF = 0.52 ± 0.01.[78] The DTDCTB is by far the most efficient NIR cell among the vacuum deposited small molecules. Together with its high V_{OC}, it has also been a red subcell candidate for multijunciton applications.[64]

The HOMO levels of the d-a-a' molecules can be effectively tuned by modifying the D unit where the HOMOs are heavily populated, while it barely affects the LU-MOs. DTDCPB were reported followed the previous work, which contains a weaker

43

ditolylaminophenyl donor block to replace the ditolylaminothienyl in DTDCTB.[79] Different from the almost coplanar confirmation between 'd' and 'a' blocks in DTD-CTB, there is a large distortion between the phenylene and benzothiadiazole rings in DTDCPB with a dihedral angle of 24.7°. The bond length between these two units as well as the bond length alternation are also longer than that of DTDCTB, indicating weaker π-delocalization and reduced quinoidal character. The DTDCPB molecule thus shows blue-shifted absorption with reduced extinction coefficients. With a better balance between current density and voltage, the DTDCPB:C_{70} (1:1.6) PM-HJ device exhibited a higher $PCE = 6.6 \pm 0.2\%$.[79]

Later Y. Zou $et\ al.$ eliminated the neat donor and acceptor layers in DTDCPB:C_{70} cells for better charge collection. The thickness of the mixed active layer was increased from 40 nm to 70 nm without affecting the FF. The champion device with the structure: ITO/MoO$_3$ (10 nm)/DTDCPB:C_{70} (1:2, 70 nm)/BCP (10 nm)/Al (100 nm) delivered $J_{SC} = 14.8$ mA/cm^2, $V_{OC} = 0.89$ V, $FF = 0.62$ and $PCE = 8.2\%$.[80] O.L.Griffith $et\ al.$ further optimized the DTDCPB:C_{70} cell with additional donor material purification and the BPhen:C_{60} compound buffer. The device with 1:1 D:A ratio and 80 nm active layer thickness achieved $PCE = 9.6\%$, the highest among vacuum deposited OPV cells with $J_{SC} = 15.8$ mA/cm2, $V_{OC} = 0.92$ V and $FF = 0.67$.[54]

The following two sections in this chapter will show our follow-up work on the two donor molecules. By device optimization, the OPV efficiencies for both molecules are further improved compared with the previously published results. The DTDCTB:C_{60} and DTDCPB:C_{70} will then be employed as the subcells in the tandem structures introduced in Chapter V and VI, respectively.

3.2 NIR-absorbing molecule DTDCTB

As we recall from Section 3.1.2 that in previous work, the molecule DTDCTB donor has been paired with both the fullerene C_{60} and C_{70} acceptor, achieving the best efficiency of 5.3% and 6.1% respectively. [56,78] Both structures exhibit similar V_{OC} ≈ 0.80 V and $FF \approx 0.55$. The main difference lies in the J_{SC}. As seen from Fig. 3.1 below, the absorption of the neat C_{70} is much higher than C_{60} along the visible spectrum below 700 nm, resulting in a higher absorption in green of the DTDCTB:C_{70} device with a higher J_{SC}. On the other hand, due to the weak absorption of C_{60}, the DTDCTB:C_{60} only shows photoresponse in the NIR region, leaving a transparent window in green. It is therefore an ideal NIR-absorbing subcell candidate for multijunction applications. This section will therefore focus on the optimization of DTDCTB:C_{60} single junction cells.

3.2.1 DTDCTB:C_{60} blend film characterization
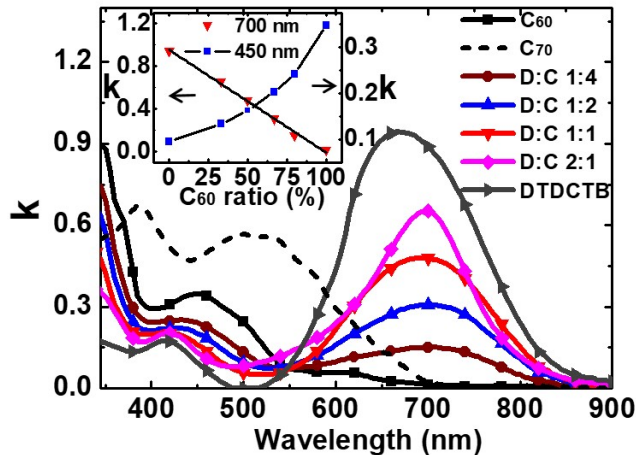
Figure 3.1: DTDCTB:C_{60} optical constants. Extinction coefficient (k) of DTDCTB:C_{60} films with different blend ratios, along with k for C_{60}, C_{70}, and DTDCTB neat films. Here, D refers to DTDCTB and C refers to C_{60}. Inset: k at $\lambda=$ 450 nm and $\lambda=$ 700 nm as a function of C_{60} percentage in the mixed film.

The extinction coefficients (k) of the DTDCTB:C_{60} films measured as functions of blend volume ratio are shown in Fig. 3.1. The DTDCTB exhibits an absorption peak at $\lambda = 700$ nm, while C_{60} shows two peaks at $\lambda = 360$ nm and 450 nm, corresponding to Frenkel-type and intermolecular CT excitations.[81] The CT feature results from electrons excited from the HOMO of one molecule to the LUMO of a nearby C_{60} molecule, and hence is sensitive to the C_{60} concentration. In contrast, the intramolecular Frenkel transition absorption strength is linearly proportional to the molecular concentration. To analyze the Frenkel and CT absorption in the DTDCTB:C_{60} mixed film, k at $\lambda = 450$ nm and $\lambda = 700$ nm as a function of the C_{60} percentage is plotted in the inset of Fig. 3.1. The DTDCTB Frenkel absorption peak at $\lambda = 700$ nm linearly decreases with C_{60} concentration, as expected. On the other hand, the C_{60} CT peak at $\lambda = 450$ nm is significantly reduced even at a modest dilution, leading to very small absorption in the green.
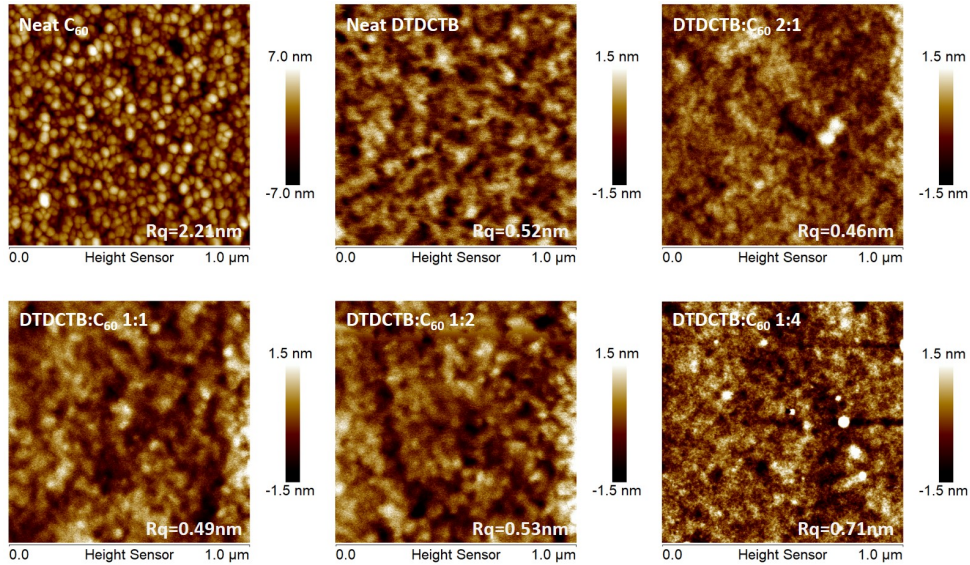
Figure 3.2: Atomic force microscopy (AFM) images of the neat C_{60}, neat DTDCTB and DTDCTB:C_{60} with different ratios. R_q refers to the root mean square roughness.

The active layer film morphology and roughness were characterized by atomic force microscopy (AFM) as shown by Fig. 3.2, with different D:A ratios. The neat

C_{60} appears to be ball shapes with diameter ~ 20 nm and a surface roughness of R_q = 2.21 nm. The neat DTDCTB, on the other hand, shows an amorphous surface with R_q = 0.52 nm. The mixed film of the donor and acceptor molecules greatly reduce the C_{60} roughness, showing amorphous feature similar with DTDCTB. The roughness also decreases at lower C_{60} concentration, with R_q = 0.71 nm at 1:4 D:A ratio and R_q = 0.49 nm for D:A=1:1.
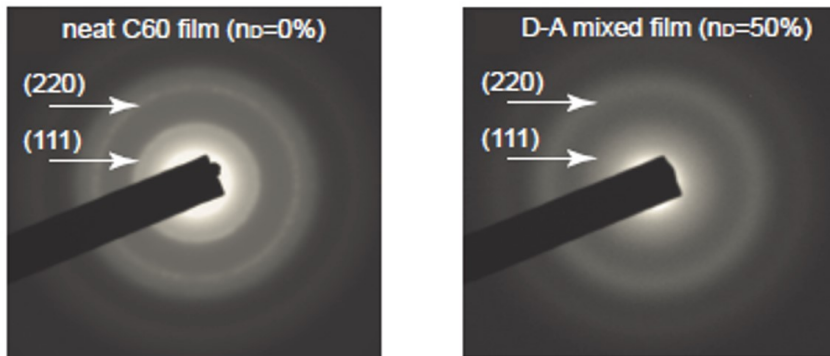
Figure 3.3: Selected area electron diffraction (SAED) patterns of the C_{60} and 1:1 DTDCTB:C_{60}.

Fig. 3.3 shows the selected area electron diffraction (SAED) patterns of the neat C_{60} and 1:1 DTDCTB:C_{60} films. The film morphology changes from granular to smooth. The C_{60} shows a polycrystalline, face centered cubic structure. The diffraction rings are relatively clear, corresponding to the (111) and (220) planes as labeled. In contrast, the SAED pattern for the DTDCTB:C_{60} mixture is diffuse, indicating a more disordered, isotropic morphology. The AFM and SAED morphology data both show that mixing the donor molecule DTDCTB with the acceptor C_{60} leads to amorphous structure and smooth surface. We will see in the following subsections that the DTDCTB:C_{60} with 1:1 ratio achieves the best device performance with the lowest trapped charge density.

3.2.2 Device optimization and performance

Devices with the P-HJ structure were first fabricated and studied, as shown in Fig. 3.4 on the left. The MoO_3 serves as the anode buffer layer due to its large work function, high transmittance, and low resistance[82], while BPhen is used as the exciton blocking buffer layer adjacent to the cathode[83]. The thickness of C_{60} active layer is fixed at 40 nm, while the DTDCTB thickness is changed from 5 nm to 15 nm. As seen from the EQE plots, the C_{60} photoresponse around 450 nm decreases with increased DTDCTB thickness. On the other hand, the EQE in the NIR region is also reduced with thicker DTDCTB up to 15 nm, showing inefficient charge extraction with layers thicker than the exciton diffusion length.
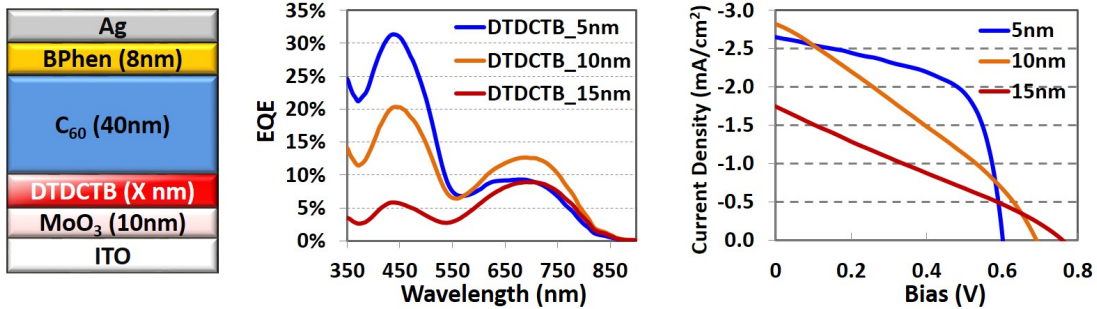
Figure 3.4: DTDCTB/C_{60} bilayer device structure and performance, including EQE and J-V characteristics with different DTDCTB thicknesses.

It is clear from the J-V plots in Fig. 3.4 that with 5 nm DTDCTB, the cell exhibits diode-like behavior, with $J_{SC} = 3.8$ mA/cm^2, $V_{OC} = 0.60$ V, $FF = 0.61$ and $PCE = 1.4\%$. As the thickness increases to 10 and 15 nm, the curves are dominated by series resistance, and the FF is reduced to ~ 0.25. On the other hand, the V_{OC} increases considerably from 0.60 V to 0.76 V, indicating the poor converage of the DTDCTB on C_{60} in the 5 nm case. Based on the results, we can therefore conclude that the DTDCTB has a very short exciton diffusion length on the order of 5 nm, which is generally the case for d-a-a' donor molecules. The active layer therefore needs to be made in a M-HJ structure to achieve better performance.
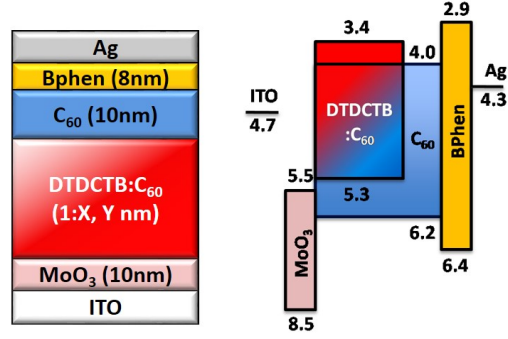
Figure 3.5: The DTDCTB:C_{60}/C_{60} PM-HJ device structure (left) and energy levels (right).

Table 3.1: DTDCTB:C_{60} (40nm) device performance with different ratios.

DTDCTB:C_{60} Ratio (40 nm thickness)	J_{SC} (mA/cm^2)	V_{OC} (V)	FF	PCE* %
1:4	7.3	0.82	0.50	3.0
1:2	9.1	0.78	0.54	3.8
1:1	10.3	0.80	0.54	**4.4**
1.5:1	10.1	0.78	0.43	3.4
2:1	8.6	0.78	0.39	2.6

* Edge effect not considered, giving $\sim$ 10% overestimation.

The device structure with mixed DTDCTB:C_{60} active layer is optimized in terms of D:A mixed ratio, layer thicknesses and buffer layers. Among the three active layer architectures: D/D:A/A, D:A/A and D:A, the mixed DTDCTB:C_{60} plus a neat layer of C_{60} gives the best balance between J_{SC} and FF. The detailed device structure is shown in Fig. 3.5 along with the energy level diagram. Again, MoO$_3$ and BPhen serve as the buffer layers respectively on the anode and cathode side. The neat C_{60} layer was fixed at 10 nm while the ratio and thickness of the DTDCTB:C_{60} mixed layer are optimized, with the results summarized in Table 3.1 and 3.2. The V_{OC} stays $\sim$ 0.8 V with different ratios, while both J_{SC} and FF reach the maximum value at 1:1, giving the highest $PCE = 4.4\%$ with active layer thickness fixed at 40 nm. The

relation between the DTDCTB:C_{60} ratio and *FF* will be discussed in the next section with the study of charge trapping density.
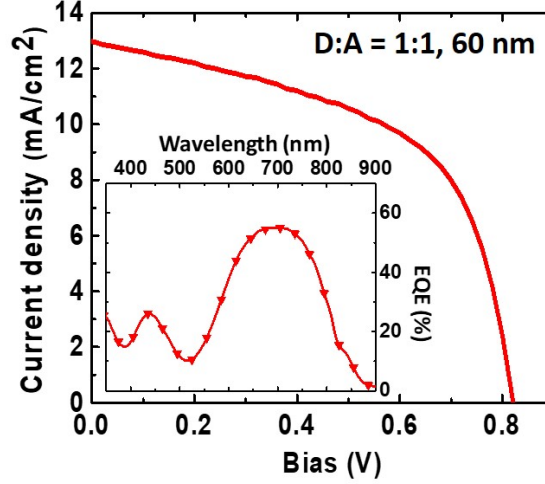
Figure 3.6: DTDCTB:C_{60}/C_{60} PM-HJ device performance: *J-V* characteristics and *Inset: EQE.*

Table 3.2: DTDCTB:C_{60} (1:1) device performance with different thicknesses.

DTDCTB:C_{60} Thickness (1:1 ratio)	J_{SC} (mA/cm^2)	V_{OC} (V)	FF	PCE* %
40 nm	9.0	0.82	0.52	3.8
45 nm	10.6	0.82	0.53	4.6
50 nm	11.3	0.82	0.53	4.8
55 nm	12.3	0.82	0.56	5.6
60 nm	12.7	0.82	0.56	**5.8**
65 nm	12.6	0.82	0.54	5.6

* Edge effect not considered, giving $\sim 10\%$ overestimation.

After optimizing the ratio, the cells with different DTDCTB:C_{60} thicknesses from 40 nm up to 65 nm were fabricated with the D:A ratio fixed at 1:1. The $V_{OC} = 0.82$ V is independent of thickness, while J_{SC} increases as the active layer gets thicker and saturates at ~ 60 nm. The reduced charge collection ability with further increased

thickness suppressed the absorption increases. The FF also increases with thickness, from $FF = 0.52$ at 40 nm to $FF = 0.56$ at 60 nm, which is likely due to improved crystallization of the DTDCTB molecule. The J-V characteristics and EQE of the optimized device with 1:1 ratio and 60 nm thickness is displayed in Fig. 3.6. It achieves $J_{SC} = 12.7$ mA/cm^2, $V_{OC} = 0.82$ V, $FF = 0.56$ and $PCE = 5.8\%$. Due to the edge effect as will be discussed later in this chapter, the J_{SC} is corrected by EQE measurement, giving $PCE = 5.3\%$. It equals to the best DTDCTB:C$_{60}$ device published in the literature[56]. As seen from the EQE plot in Fig. 3.6, it mainly absorbs between $\lambda = 500$ nm and 900 nm, with the peak value of $EQE \approx 55\%$ at $\lambda = 700$ nm. On the other hand, the EQE in the green below 500 nm is less than 30% due to the exponentially reduced C$_{60}$ CT absorption when mixing with DTDCTB, showing potential for use in the multijunciton NIR-absorbing subcells.
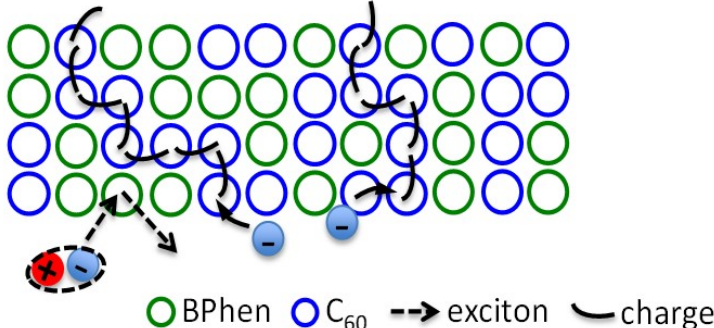
Figure 3.7: BPhen:C$_{60}$ mixed buffer working mechanism.

Different cathode buffer combinations are also tested for the optimized DTDCTB:C$_{60}$ active layer, with the performances summarized in Table 3.3. The device with BPhen serves as the reference cell, with $PCE = 5.4\%$. It has been reported that adding an ultrathin low work function metal layer like Ca between the BPhen buffer and the Ag cathode reduces the charge extraction barrier, leading to higher photocurrent.[56] Here we observed similar phenomena, that the current density is improved from 12.4 mA/cm^2 to 12.8 mA/cm^2. The PCE is also slightly improved to 5.5%. In addition, a BPhen:C$_{60}$ electron filter has been previously reported for efficient exciton blocking

Table 3.3: DTDCTB:C_{60} device performance with different cathode buffers.

Cathode Buffer	J_{SC} (mA/cm^2)	V_{OC} (V)	FF	PCE* %
BPhen	12.4	0.82	0.52	5.4
BPhen w/ Ca	12.8	0.82	0.52	5.5
BPhen:C_{60} 1:1	11.6	0.82	0.55	5.2
BPhen:C_{60}/Bphen	11.4	0.82	0.55	5.1

* Edge effect not considered, giving $\sim 10\%$ overestimation.

and electron conducting.[84] As illustrated in Fig. 3.7, the electrons conduct through the C_{60} path indicated by the blue circles, while excitons can still be blocked efficiently by BPhen with a wide energy gap. The optimal BPhen:C_{60} ratio is 1:1, exhibiting the maximum conductivity and $> 80\%$ blocking ratio.[84] The FF of DTDCTB:C_{60} cell employing the mixed buffer is improved, while the J_{SC} is decreased. The PCE is slightly reduced to 5.2%.

3.2.3 Charge trapping in mixed DTDCTB:C_{60} films

Charge trapping in the active layer of OPVs has previously been studied using methods such as impedance spectroscopy, deep-level transient spectroscopy, transient photocurrent, and thermally stimulated current. It has been found that trapping is strongly dependent on the particular combination of D-A molecules and illumination conditions employed. However, the important problem of the dependence of charge trapping on the content and concentration of D-A mixtures and on film morphology has not been thoroughly investigated previously. Here we describe a method based on the current induced by a short wavelength optical pump measured using a longer wavelength probe beam[85] that provides an accurate and quantitative determination of the trapped charge density in organic semiconductor thin films.[86]

Figure 3.8, left, shows the pump-probe set up configuration. The relatively intense
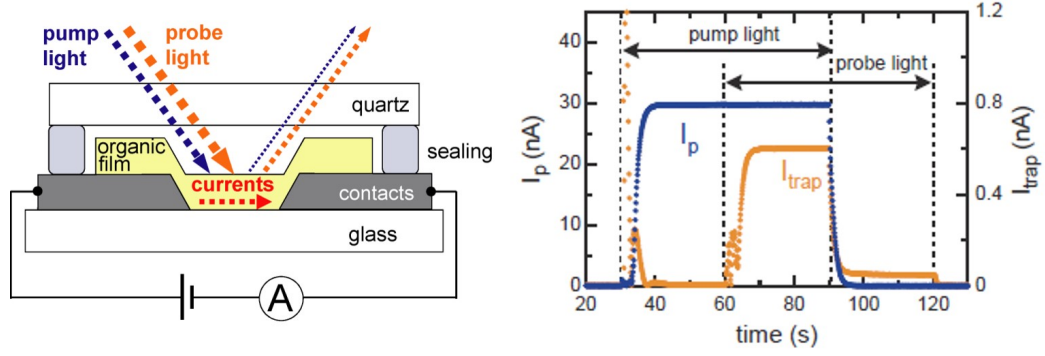
Figure 3.8: The pump-probe charge trapping measurement. Schematic of the measurement and sample configurations (left), and time evolution of the C_{60} photo- and trap-currents under pump and probe illumination (right). The film is packaged to prevent exposure to the environment. Figures from Ref.[86].

illumination of the high energy pump populates the traps with charges generated subsequent to exciton dissociation. The trapped charges are then depopulated by a delayed, low energy pulse that induces an incremental current. The currents are collected at the interdigitated contacts on the substrate. The charge generation rates from the HOMO level and the trap state are given by:

$$g_{HOMO} = n_{HOMO}\sigma_{HOMO}\Gamma_{pump};\qquad(3.1a)$$

$$g_{trap} = n_{trap}\sigma_{trap}\Gamma_{probe},\qquad(3.1b)$$

where n are the densities of electrons in HOMO level and in trap states denoted by the subscripts, HOMO and trap. σ is the photo-absorption cross-section, and Γ is the single pass photon flux generation efficiency of the pump or the probe. The trapped-to-HOMO charge density ratio can be expressed as:[86]

$$\frac{n_{trap}}{n_{HOMO}} = \left[\frac{\sigma_{HOMO}}{\sigma_{trap}}\right]\left[\frac{\Gamma_{pump}I_{trap}}{\Gamma_{trap}I_p}\right].\qquad(3.2)$$

I_p and I_{trap} are the free charge and trap induced currents. During the measurement we assume the cross sections are equal: $\sigma_{HOMO} = \sigma_{trap}$. Figure 3.8, right, shows the

time evolution of I_p and I_{trap} for a neat C$_{60}$ film as an example. I_{trap} is significant only when the pump is present, between $t = 60$s and 90s. Once the pump illumination is terminated, $I_{trap} \rightarrow 0$, indicating that I_{trap} is due only to carriers excited from trapping sites. An offset in I_{trap} observed following the pump illumination ($t = 90$ - 120s) is due to thermal emission of residual trapped charge that vanishes once the probe is turned off.

The I_{trap} is found to saturate at high pump power (P_{pump}), whereas I_p increases linearly with P_{pump}, i.e. $I_p \propto P_{pump}$, suggesting an intensity-independent photo-generation efficiency. Correspondingly, n_{trap}/n_{HOMO} determined from Eq. 3.2 also saturates at high P_{pump} due to nearly complete occupation of the trap sites. The n_{trap}/n_{HOMO} ratio is measured to be 10^{-4} at high P_{pump}. By assuming $n_{HOMO} = 10^{21}$ cm^{-3} corresponding to the approximate acceptor molecular density, the trap density is therefore $n_{trap} = 10^{17}$ cm^{-3}.
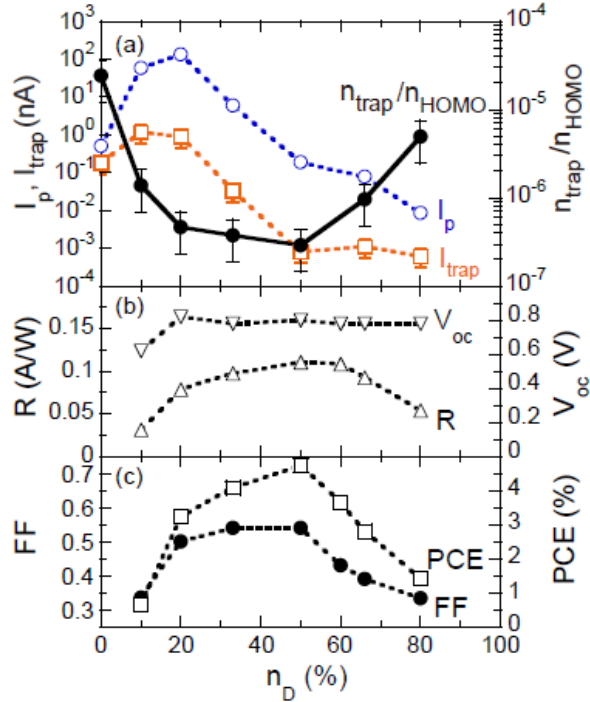
Figure 3.9: Charge trapping characteristics and DTDCTB:C$_{60}$ device performance as functions of donor concentration n_D.

With the same method, the I_{trap}, I_p and n_{trap}/n_{HOMO} of DTDCTB:C_{60} mixed films are measured as a function of the DTDCTB donor concentration, n_D (see Fig. 3.9a). Fig. 3.9b and c display the device parameters as a function of n_D, which have been discussed in the previous subsection for device optimization. Interestingly, n_{trap}/n_{HOMO} is reduced by a factor of ten as n_D is increased from 0% (neat C_{60}) to 20% (C_{60}-rich mixed film). When n_D is increased to 50%, that is the 1:1 DTDCTB:C_{60} film, n_{trap}/n_{HOMO} reaches a minimum of $3 \pm 1.5 \times 10^{-7}$, and thereafter, monotonically increases. On the other hand, the highest PCE is achieved at $n_D \approx 50\%$. Further, I_p increases with n_D at smaller concentration due to efficient exciton dissociation in the mixtures, as expected. The maximum I_p is obtained at $n_D \approx 20\%$. The efficiency variation with doping density directly follows changes in FF, while FF decreases monotonically, from 0.54 ± 0.01 to 0.33 ± 0.01, as n_{trap}/n_{HOMO} increases from $3 \pm 1.5 \times 10^{-7}$ to $5 \pm 2.5 \times 10^{-6}$, as shown in Fig. 3.10. It provides direct evidence that D-A interface recombination leads to the commonly observed dependence of FF in mixed heterojunction OPV devices on the mixture ratio.
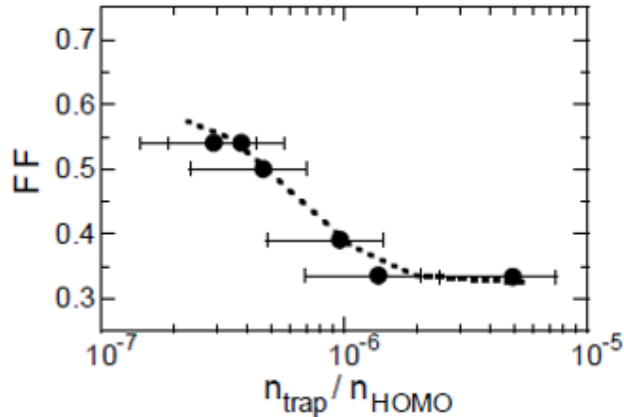
Figure 3.10: FF vs. n_{trap}/n_{HOMO}: as n_{trap}/n_{HOMO} increases, FF monotonically decreases. The dotted line is a guide to the eye.

The high n_{trap}/n_{HOMO} in the neat C_{60} film suggests that charges are trapped at the grain boundaries as illustrated by Fig. 3.11a. As shown in Fig. 3.9, n_{trap}/n_{HOMO} is U-shaped relative to the donor concentration in the blend film, with a minimum at n_D

$\approx 50\%$. This suggests that charge trapping occurs at the D-A nanocrystalline domain boundaries in the mixed films. For DTDCTB:C_{60} mixtures, the D-A interfaces form a transport barrier of 0.56 eV for electrons and 0.9 eV for holes as calculated from the LUMO and HOMO energy offsets between these molecules. Hence, electron transport across C_{60} domains is blocked by donor domains at high n_D, whereas the transport of holes is blocked by acceptor molecules at low n_D, as illustrated in Figs. 3.11b and c. These boundaries are minimized (along with n_{trap}/n_{HOMO}) for approximately equal concentrations of donor and acceptor molecules, at which point continuous percolating pathways are formed that transport holes and electrons, respectively, resulting in the best device performance especially in FF.
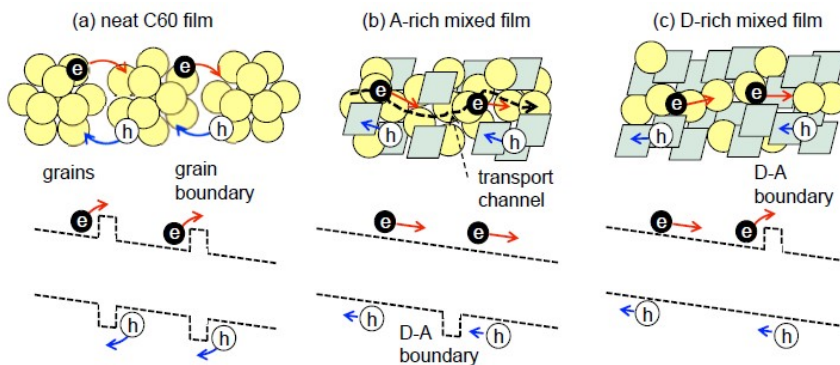
Figure 3.11: Charge carrier transport (upper figures) and energy band diagram (lower figures): (a) Neat, granular C_{60}, (b) uniform smooth acceptor-rich mixed films, (c) uniform smooth donor-rich mixed films.

3.3 Green-absorbing molecule DTDCPB

3.3.1 Device performance

In addition to DTDCTB, the OPV devices with the d-a-a' molecule DTDCPB with the propeller diethylaminoethyl donor block are fabricated and optimized. As introduced in the background section, the twisting angle between the 'd' and central 'a' unit of DTDCPB is as large as 24.7°compared with the 5.7°of DTDCTB (Fig. 3.12, left). Due to the weaker electron donating ability, the DTDCPB exhibits reduced

intramolecular charge transfer and blue shifted absorption, as shown by Fig. 3.12 (right). The DTDCPB solid state film mainly absorbs from $\lambda = 450$ nm to 750 nm, with a peak extinction coefficient (k) value of ~ 0.5 compared with 0.9 for DTDCTB. We therefore pair it with the acceptor C_{70} with much higher absorption in the visible than C_{60} to achieve the high efficiency OPV cell.
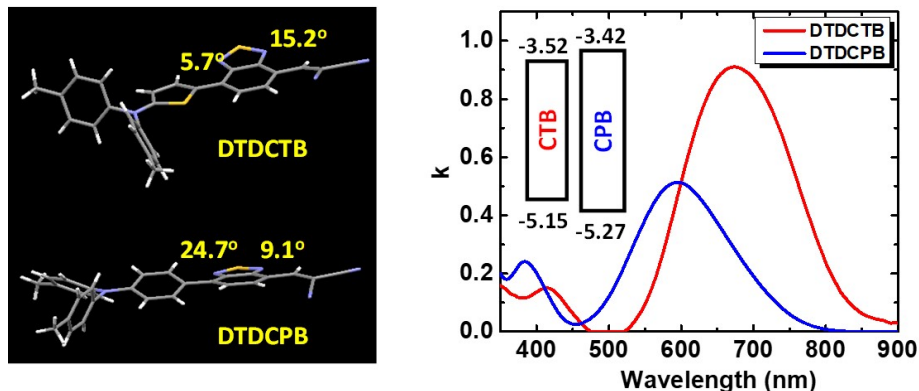
Figure 3.12: Single crystal molecular structures (left) and extinction coefficients (right) of DTDCTB and DTDCPB film.
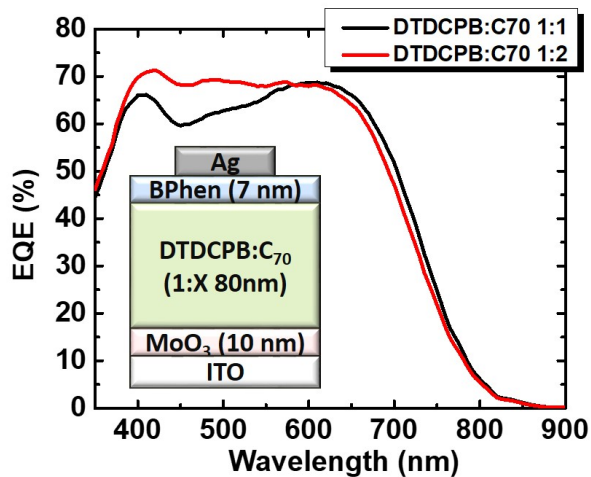
Figure 3.13: DTDCPB:C_{70} single junction *EQE* with 1:1 and 1:2 ratios. *Inset:* device structure.

The DTDCPB:C_{70} device structures are optimized in the same way as the DTD-CTB:C_{60} cells. The active layer with M-HJ structure (without the neat layer) gives

the best performance. The device structure and EQE with 80 nm active layer thickness and 1:1 or 1:2 D:A ratio are displayed in Fig. 3.13, with the performances summarized in Table 3.4. From the EQE curves we can see that both cells have the peak value $\sim 70\%$, while the 1:2 ratio exhibits higher photoresponse in the visible region below 600 nm and slightly lower absorption in NIR. The device with 1:2 ratio achieves slightly higher J_{SC} and FF than the 1:1 ratio, while the V_{OC} is reduced from 0.92 V to 0.90 V. The optimized DTDCPB:C$_{70}$ (80 nm) cell achieves $FF = 0.70$ and $PCE = 9.5\%$, which is the highest efficiency among the vacuum-deposited OPV cells to date.

Table 3.4: DTDCPB:C$_{70}$ device performance with 1:1 and 1:2 ratios.

D:A ratio (80 nm thickness)	J_{SC} (mA/cm^2)	V_{OC} (V)	FF	PCE %
1:1	14.8	0.92	0.69	9.4
1:2	15.0	0.90	0.70	9.5

3.3.2 Thick active layer

The vacuum-deposited small molecule OPV cells generally possess the active layers thinner than 100 nm, for example, 60 nm for DTDCTB:C$_{60}$ and 80 nm DTDCPB:C$_{70}$. Thicker active layers could increase the bimolecular recombination probability of the dissociated polarons, leading to reduced FF. The absorption coefficient peak values of the small molecule D:A blends is mostly between $\alpha = 1 \times 10^5$ cm^{-1} and 2×10^5 cm^{-1}. The intensity of light transmitted through the film is:

$$I = I_0 e^{-\alpha d}, \tag{3.3}$$

where I_0 is the incident light intensity, and d is the film thickness. Therefore it requires $d \sim 100$ - 200 nm to achieve 90% absorption of the peak wavelength. The

wavelength off the peak value needs even thicker film for efficient absorption.

For opaque single junction cells, the incident light travels in the device for roughly twice the film thickness due to metal cathode reflection like Ag, that the active layer under 100 nm can be sufficient for absorption. For applications like semitransparent solar cells as well as the multijunction front cell where the cathode is transparent or far away, the cell requires much thicker active layer to generate the same amount of current as the opaque single junction cell. Here, we demonstrate a thick DTDCPB:C_{70} cell with the active layer thickness up to 180 nm and $PCE > 10\%$.
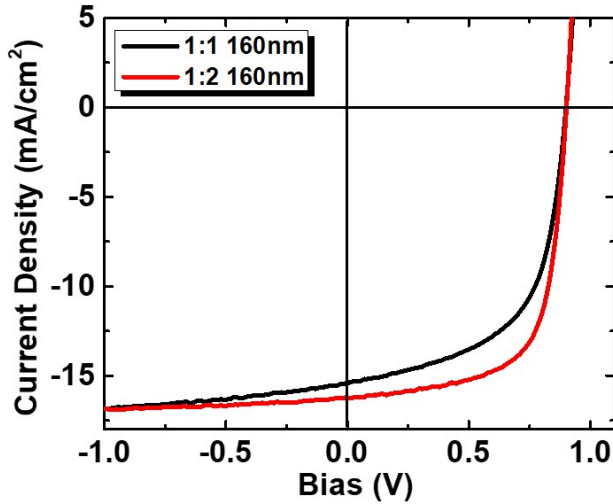
Figure 3.14: *J-V* characteristics of DTDCPB:C_{70} cell (1:1 and 1:2) with 160 nm active layer thickness.

The DTDCPB:C_{70} cell with 1:1 ratio has been reported, with the highest efficiency of 9.6%.[54] The device with 1:1 ratio and 80 nm active layer thickness achieved comparable $PCE = 9.4\%$ as presented in previous subsection. However, as the thickness goes to 160 nm, the *FF* falls from 0.69 to 0.59. Though J_{SC} increases from 14.8 to 15.4 mA/cm^2, the efficiency is reduced to only 8.2%. Interestingly, as the D:A ratio changes from 1:1 to 1:3 with the thickness fixed at 160 nm, the *FF* is improved as listed in Table 3.5. It reaches the maximum value of 0.67 at 1:2 ratio. The J_{SC} also increases to > 16 mA/cm^2 at higher D:A ratios.

59

Figure 3.14 compares the J-V characteristics of the 1:1 and 1:2 ratio devices with 160 nm thickness. The current density of both cells converge to 16.8 mA/cm^2 at -1 V reverse bias with sufficient charge exaction, indicating similar absorption and charge generation. However, the 1:1 cell shows a much faster current drop towards 0 V and foward bias while the cell with 1:2 D:A ratio stays relatively flat. It therefore indicates a more ideal charge transport path of electrons and holes in the 1:2 film than that of the 1:1 film, promoting more efficient charge extraction thus higher J_{SC} and FF. The 1:2 cell with 160 nm thickness achieves $PCE = 9.8\%$, improved from the 80 nm cell. As we can see from Table 3.5, increasing the active layer thickness to 170 nm further increase the J_{SC} to 17.0 mA/cm^2 while the FF is slightly reduces to 0.66, giving a higher $PCE = 10.2\%$. Further increase in thickness to 180 nm reduces all the performance parameters, indicating inefficient charge extraction. The DTDCPB:C$_{70}$ cell with the thick active layer will be further discussed in Chapter VI for tandem applications.

Table 3.5: DTDCPB:C$_{70}$ device performance with thick active layers.

$DTDCPB{:}C_{70}$ Device	J_{SC} (mA/cm^2)	V_{OC} (V)	FF	PCE %
1:1 (160nm)	15.4	0.90	0.59	8.2
1:1.5 (160nm)	16.5	0.90	0.65	9.6
1:2 (160nm)	16.2	0.90	0.67	9.8
1:3 (160nm)	16.3	0.91	0.65	9.6
1:2 (170nm)	17.0	0.91	0.66	10.2
1:2 (180nm)	16.8	0.89	0.65	9.7

3.4 Edge effects

Organic materials generally possess low charge mobilities ($< 10^{-2}$ cm^2/V·s) due to charge hoping conduction characteristics. Their commonly assumed lateral charge diffusion lengths < 1 μm is much shorter than the millimeter to centimeter OPV device dimensions. Therefore, the device area is often defined by the overlap between anode and cathode. However, we find that under certain structural circumstances, the fullerene molecules in the OPV cells exhibit centimeter-scale electron diffusion, orders of magnitude longer than what expected for organics. Both DTDCTB and DTDCPB devices can generate current outside the device edge identified by the electrodes, the so-called 'edge effect'.[87]
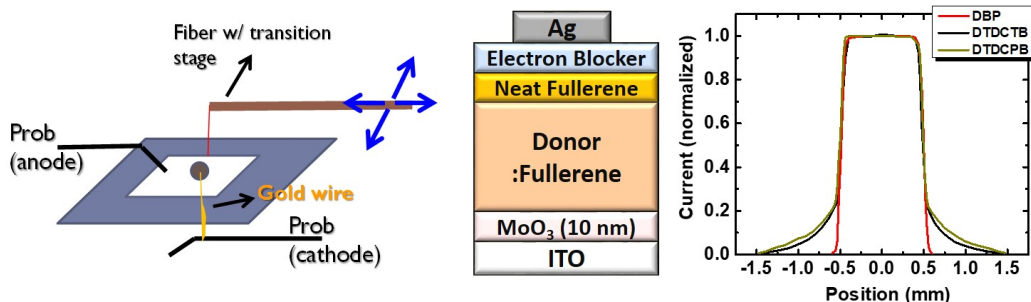
Figure 3.15: Line scan of the OPV devices comprising different donor materials, showing the setup (left), device structure (middle) and scan profiles (right).

The device structure exhibiting edge effects measured by line scan is shown in Fig. 3.15. The active layer contains the mixed donor:fullerene heterojunction capped by a neat fullerene layer, sandwiched in between the MoO$_3$ anode buffer and the electron blocker such as BPhen. For the measurement, as shown on the left, the white light being chopped at ~ 200 Hz is incident from the glass substrate through a fiber with a ~ 20 μm core size. The current generated from the cell is read by a lock-in amplifier, and it is measured as a function of fiber position both outside and inside the device area. As shown in Fig. 3.15 on the right, both the DTDCTB:C$_{60}$ and DTDCPB:C$_{70}$ devices with a C$_{60}$ neat layer show signal with the fiber illuminated outside the cells.

They are grown on unpatterned ITO with the area defined by the 1 mm diameter circular Ag cathode. The cell position is from -0.5 mm to 0.5 mm, while the signal extends up to $\pm$ 1.5 mm. The relatively large signal drop at the device edge ($\pm$ 0.5 mm) is primarily due to the lack of cathode reflection as well as the smaller built-in field outside the contact area that reduces the charge collection efficiency. The current signal of the DBP:C_{70} cell with the same device structure, however, drops to zero immediately outside the Ag cathode. The edge effect of DTDCTB:C_{60} and DTDCPB:C_{70} can be explained by electron diffusion in the neat fullerene cap layer confined by energy barriers on both sides almost free of recombinations. It is enabled by the energy level shift $\sim$ 0.3 eV of the fullerene molecule in the mixed active layer as compared with the neat layer.[87] A surprisingly long $L_D = 3.5$ cm is estimated for C_{60} under such device architecture.
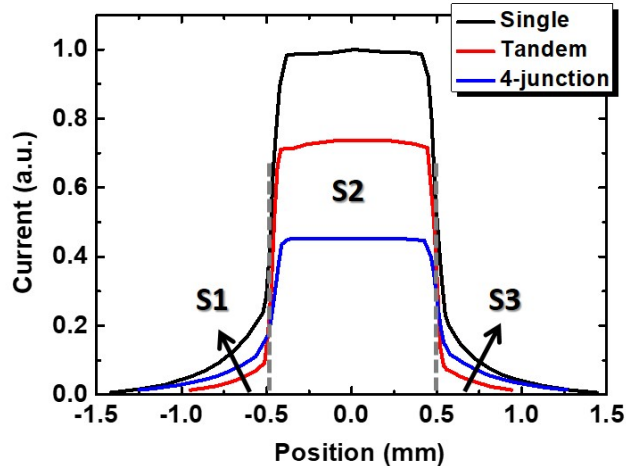
Figure 3.16: Line scan profile of single, tandem and 4-junction cells. S1, S2, S3 refers to the area under the curve with the position < -0.5 mm, -0.5mm - 0.5 nm and > 0.5 nm.

The edge effect for OPV cells can lead to the overestimation of J_{SC} and *PCE*. So far it has only been found in DTDCTB and DTDCPB PM-HJ devices with a neat fullerene layer. The performances of the DTDCTB:C_{60} cell in this chapter as well as the multijunction cells in Chapter V therefore both have edge effects. Figure 3.16

Table 3.6: Edge effect correction of J_{SC} with single, tandem and 4-junction structures.

*Device**	*S2:(S1+S2+S3)*	*2D integration*	$J_{SC,actual}:J_{SC,measured}$
Single	10 : 11	5 : 6	10 : 11
Tandem	13 : 14	6 : 7	8 : 9
4-junction	5 : 6	2 : 3	5 : 6

* Single junction refers to the DTDCPB:C_{60} cell with neat C_{60} layer; Tandem and 4-junction cells comprise DTDCPB:C_{60} and DBP:C_{70} subcells (details see Chapter V).

plots the line scan profiles of the single junction DTDCPB:C_{60} as well as the tandem and quadruple-junction cells with 1 mm diameter circular device area (see Chapter V for structural details). The ratio (either 1-Dimension or 2-D integration) between the area under the curve inside the device (S_2) and the total area ($S_1+S_2+S_3$) is summarized in Table 3.6. The quadruple-junction cell exhibits more intense edge effect than the tandem and single junction cell. It is likely due to its smaller current density and the very thick stack that the area outside the device without metal reflector can still generate relatively large current.

The line scan profile can only give a rough estimation of the current generated outside the device, due to the relatively large fiber light spot and the non-standard incident white light spectrum. All $J_{SC,actual}:J_{SC,measured}$ ratios lie in between the 1-D and 2-D integrations. The single junction DTDCPB:C_{60} generates $\sim 10\%$ current outside the device area. It can be corrected directly by taking the integrated EQE as J_{SC} as mentioned in Section 3.2.2. The ratio between the tandem cell J_{SC} measured without and with elimination the edge effect is 8:9, while it is 5:6 for the quadruple-junction cell, showing the overestimation can be as large as 20%. An accurate J-V measurement for multijunciton cells therefore should be conducted using a shadow mask underfilling the device that confines the illumination area. The d-a-a' molecules besides DTDCTB discussed in this dissertation all employ M-HJs structures without the neat acceptor layer, therefore are not affected by this phenomenon.

CHAPTER IV

D-a-a' Small Molecule Donors with Coplanar Donor Units

In the previous chapter, we discussed two d-a-a' small molecule donors, DTDCTB and DTDCPB, with the ditolylaminothienyl and ditolylaminophenyl propeller shape donor units. The DTDCPB:C_{70} device is able to achieve $PCE > 10\%$, so far the most efficient vacuum deposited OPV. In this chapter, a new set of molecules bearing coplanar donor groups with reduced rotational freedom are designed and characterized, achieving comparable device performance with DTDCPB.

4.1   Background

The electron-donating coplanar dithieno[3,2-b:2,3-d]pyrrole (DTP)-based groups have been introduced to vacuum deposited d-a-a' molecules.[88] Though lacking direct nitrogen contributions to the conjugated backbones that leads to blue-shifted absorption, the DTP-based molecules generally exhibit larger absorption coefficient with higher photocurrent. H. Lu *et al.* synthesized and characterized a set of molecules in 2014 with DTP or aryl-substituted DTP as the donor block and benzothiadiazole-DCV (molecules DBT, TDBT, ADBT) or pyrimidine-DCV (molecules DPT, TDPT, ADPT) as the a-a' units.[88] The donor with DBT showed longer wavelength absorp-

tion than DPT due to better quinoidal behavior of benzothiadiazole than pyrimidine. On the other hand, molecules with terminal aryl substitutions on the α position of DTP displayed improved chemical stability as well as red-shifted absorption with an extended conjugation length. The PM-HJ devices were prepared with 1:2 donor:C_{70} ratio. Among all the six donors, the TDPM with the p-tolyl-substituted DTP-pyrimidine-dicyanovinylene configuration showed the highest $PCE = 5.6\%$. However, the conformational flexibility between DTP and the terminal aryl substitution may subtly influence the intermolecular interactions that are crucial for OPV performance.

Here we synthesize and characterize a set of d-a-a' donor molecules with the benzene ring fused onto the DTP unit that forms a heterotetracene to reduce rotational disorder. Molecules with different conjugation lengths and side chain configurations are studied to further clarify their structure-property-performance relationships in OPVs.[55,89]

4.2 Cross-conjugation effects of d-a-a' donors on V_{OC}

4.2.1 Intramolecular charge transfer

The d-a-a' molecules, antiBTDC and synBTDC are first synthesized to understand the cross-conjugation effect, which refers to the condition where one of the three π-bonds in a set is excluded from interaction that interrupts the electron delocalization. Two asymmetric heterotetracenes with different thienyl ring arrangements are introduced to couple with benzothiadiazole-dicyanovinylene, yielding the isomeric d-a-a' structures of antiBTDC and synBTDC, as shown by Fig. 4.1 on the left. Compared to previously reported DTP-based molecules[88], instead of introducing an aryl end-capping group, these d-a-a' molecules employ a terminal benzene ring that is fused with the electron-donating DTP unit to give a coplanar structure with reduced conformational variations.
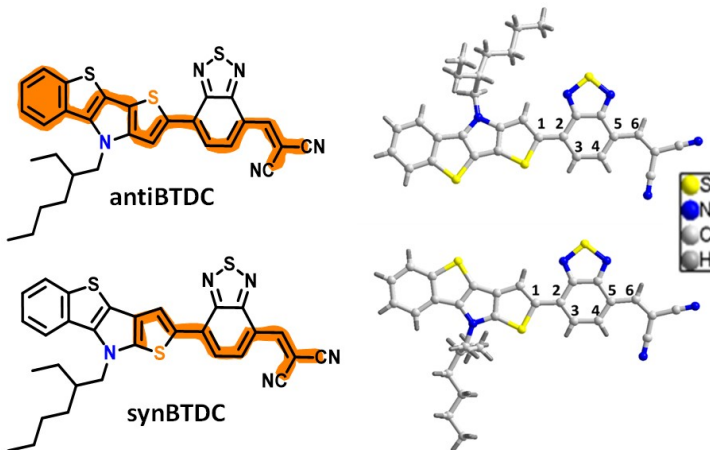
Figure 4.1: Molecular chemical structure and X-ray characterized crystal structure of antiBTDC and synBTDC d-a-a' molecules, with specific labeling of carbons.

Table 4.1: Bond lengths and bond length alternations (BLA).

Dye	C_1-C_2 (Å)	C_2-C_3 (Å)	C_3-C_4 (Å)	C_4-C_5 (Å)	C_5-C_6 (Å)	BLA^a (Å)
antiBTDC	1.426	1.398	1.417	1.375	1.433	0.031
synBTDC	1.450	1.374	1.420	1.375	1.450	0.046

[a] Calculated as $(C_3$-$C_4)$-$[(C_2$-$C_3)+(C_4$-$C_5)]/2$.

The crystal structures of antiBTDC and synBTDC characterized by X-ray diffraction are shown in Fig. 4.1, right. The bond lengths of the labeled carbon atoms are listed in Table 4.1. Bond length alternation (BLA) is defined as the difference between C3-C4 bond length and the average of C2-C3 and C4-C5 bond lengths of the benzothiadiazole acceptor.[90] We find that antiBTDC has a smaller BLA = 0.031 Å compared to 0.046 Å for synBTDC, as well as a decreased C1-C2 bond length.

The electronic density plots in Fig. 4.2 can be used to predict the transition characteristics for each molecular orbital (MO) composition, with the calculated values listed in Table 4.2. Compared to synBTDC, a bathochromic absorption shift together with a four-fold increase in the oscillator strengths (f) of the lowest energy singlet ground-to-excited state transition ($S_1 \leftarrow S_0$) was found for antiBTDC. The
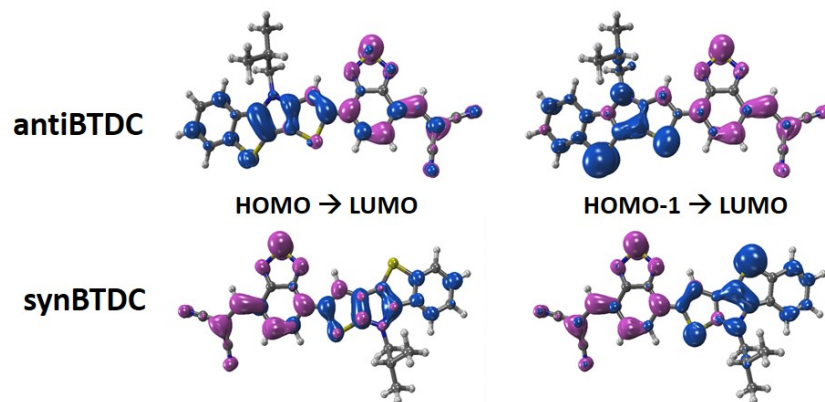
Figure 4.2: antiBTDC and synBTDC charge densities of the lowest energy singlet excitations ($S_1 \leftarrow S_0$), with the given molecular orbital (MO) transitions where blue denotes occupied, and purple symbolizes unoccupied MOs.

$S_1 \leftarrow S_0$ of antiBTDC and synBTDC comprise two MO transitions (HOMO→LUMO, and HOMO-1→LUMO) with different weighting. The HOMOs are delocalized over the molecular backbone while the LUMOs are localized on the electron-deficient benzothiadiazole-dicyanovinylene fragments. The HOMO-1 is primarily populated on the electron-rich heterotetracene unit. The lowest energy transitions of antiBTDC and synBTDC comprise both π-π* and charge transfer character. The MO spatial overlap for $S_1 \leftarrow S_0$ is calculated to be 43% and 27% for antiBTDC and synBTDC, respectively. The internal dipole moments of the ground states (μ_g) and the excited states (μ_e) are listed in Table 4.3, together with the transition dipole moments (μ_{tr}) and the total dipole moments change (μ_{ge}). Both $\mu_g = 15.42$ D and $\mu_e = 16.48$ D of antiBTDC are slightly larger than those of synBTDC ($\mu_g = 14.84$ D, $\mu_e = 13.77$ D), along with the larger $\mu_{tr} = 5.00$ D.

Compared with previously reported DTP-based d-a-a' molecules,[88] the electroactive carbon of the thiophene in DTP donor unit of antiBTDC and synBTDC is blocked by fusing a phenylene ring. The smaller BLA and shorter C1-C2 bond length of antiBTDC compared to those of synBTDC indicates a stronger electronic coupling between donor and acceptor units, which leads to larger absorption oscillator strength

Table 4.2: Computed lowest-energy electronic transition ($S_1 \leftarrow S_0$) parameters.

Molecule	λ_{calc} (nm) [a]	HUMO/ LUMO (eV) [a]	f [b]	MO composition (Λ) [c]
antiBTDC	676	-5.36/-3.33	1.12	98% HOMO → LUMO [43%] 2% HOMO1 → LUMO [16%]
synBTDC	652	-5.50/-3.29	0.25	66% HOMO ⟶ LUMO [30%] 34% HOMO-1 ⟶ LUMO [22%]

[a] Calculated with $S_1 \leftarrow S_0$.
[b] Oscillator strength.
[c] Molecular orbital (MO) overlap (Λ).

Table 4.3: Computed $S_1 \leftarrow S_0$ dipole moments.

Molecule	μ_g (D)[a]	μ_e (D)[b]	μ_{ge} (D)[c]	μ_{tr} (D)[d]
antiBTDC	15.42	16.48	1.08	5.00
synBTDC	14.84	13.77	1.07	2.31

[a] Total dipole moment at S_0.
[b] Total dipole moment at S_1.
[c] Total dipole moment change between S_0 and S_1.
[d] Total transition dipole moment between S_0 and S_1.

and fewer changes in bond length upon photoexcitation. Thus, conjugation of the donor moiety in antiBTDC can facilitate π-electron delocalization and promote intramolecular charge transfer transitions, resulting in a tendency to form mesomeric structures of the BT unit.[91] For synBTDC, however, π-electron delocalization is suppressed over the molecular backbone due to cross-conjugation regardless of the presence of the highly electronegative N atom. The density functional theory (DFT) calculations further confirm the electronic characteristics of these two molecules. We find that antiBTDC has a larger MO spatial overlap and μ_{tr}, leading to a higher electronic transition probability[92] and a larger oscillator strength associated with the $S_1 \leftarrow S_0$ transition.
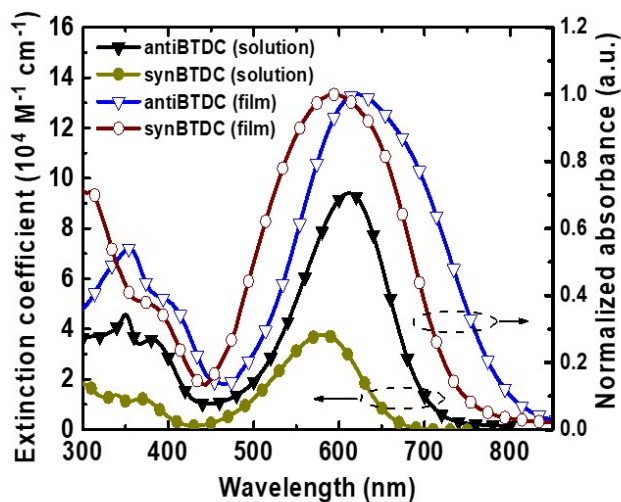
Figure 4.3: Extinction coefficient and normalized absorbance of antiBTDC and synBTDC in solution and solid state.

Table 4.4: Physical parameters of antiBTDC and synBTDC.

Dye	$\lambda_{max,solution}$ (nm)[a]	$\lambda_{max,film}$ (nm)	$E_{g,opt}$ (eV)[b]	ΔE_{CV} (eV)[c]	HOMO (eV)[d]	LUMO (eV)[e]	T_d (°C)[f]
antiBTDC	612	619	1.52	1.52	-5.4 ± 0.05	-3.9	331
synBTDC	581	594	1.66	1.63	-5.5 ± 0.05	-3.8	319

[a] Measured in CH_2Cl_2 solution.
[b] Optical gap estimated from the absorption onset of the thin films.
[c] Difference between E_{ox} and E_{red}.
[d] Highest occupied molecular orbital (HOMO) level determined by ultraviolet photoelectron spectroscopy (UPS).
[e] LUMO = HOMO + $E_{g,opt}$.
[f] Decomposition temperature obtained from thermogravimetry analysis (TGA).

The single crystal and calculated intramolecular charge transfer results above agree well with the measured molecular extinction coefficients in dichloromethane solution and their normalized thin film absorbances, as shown by Fig. 4.3. Compared with antiBTDC, the thin film absorption onset of synBTDC is hypsochromically shifted from a wavelength of $\lambda = 820$ nm to 750 nm. The full width at half maxima (FWHM) of the absorption spectra of both films are broadened by ~ 70 nm with a

10 nm red shift compared with their solution spectra. Compared with antiBTDC, the optical energy gap of synBTDC is increased from 1.52 ± 0.03 eV to 1.66 ± 0.04 eV, while the measured HOMO level is shifted from -5.4 ± 0.05 eV to -5.5 ± 0.05 eV. The detailed photophysical and electrochemical parameters of these two donors are summarized in Table 4.4.

4.2.2 Intermolecular charge transfer and mobility
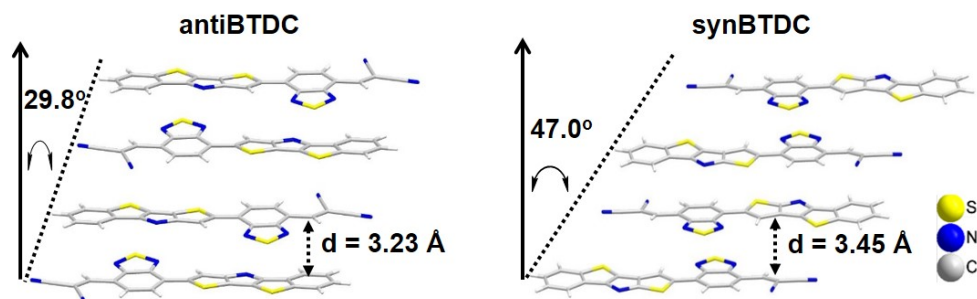
Figure 4.4: Crystal packing configurations of antiBTDC and synBTDC. Side chains are omitted for clarity.

The large ground state dipole moments of antiBTDC and synBTDC lead to an antiparallel molecular arrangement along their long backbone axes, as shown by the crystal packing configurations in Fig. 4.4. The antiBTDC molecule has a dihedral angle of 8.8° between the thienoacene donor and benzothiadiazole acceptor with an intermolecular interfacial distance of 3.23 Å. In contrast, synBTDC shows an almost perfect coplanar conformation with a dihedral angle of 1.9° between 'd' and central 'a' units, but a larger interfacial distance of 3.45 Å. Also seen from Fig. 4.4, antiBTDC exhibits a co-facial π-stacking with a pitch angle of 29.8°, while synBTDC forms a staircase-like arrangement with a much larger pitch angle of 47.0°. DFT calculations were performed to visualize the electrostatic potential of monomers and dimers (Fig. 4.5) found in the crystal structure. The antiparallel dimeric pairs show a reduced polarized electrostatic potential as compared to that of the monomers. The antiBTDC dimer exhibits a more homogeneous electron density distribution over the

molecular backbone as compared to the synBTDC dimer due to its compact stacking arrangement where each molecular donor unit is more closely positioned to an acceptor unit.
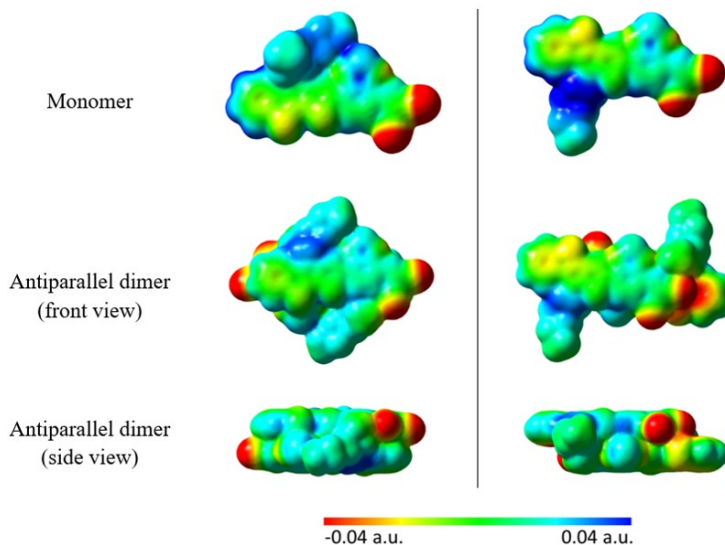
Figure 4.5: antiBTDC (left) and synBTDC (right) dimers surface electrostatic potential, calculated from the crystal geometry of dyes taking an isovalue of 0.0004.

Due to intimate intermolecular π-π stacking, the thin film absorption spectra of both isomers are broadened and red-shifted compared with their solution spectra, as shown in Fig. 4.3. The antiparallel arrangement assembles into centrosymmetric π-stacked dimers, resulting in a net dipole moment of zero.[54] Compared with synBTDC, the closer stacking of antiBTDC results in stronger intermolecular π-π interactions that facilitate charge transport, and hence a higher film conductivity and fill factor.[93] Together with a smaller pitch angle, the molecular arrangement of antiBTDC shows a diminished molecular dipole indicated by its more homogeneous electron density distribution that further improves charge transport.

In addition, the mobilities of the vacuum deposited antiBTDC and synBTDC films are measured by the methods of metal insulator semiconductor-charge extraction by linearly increasing voltage (MIS-CELIV)[94,95] as well as space charge limited current (SCLC)[96]. The MIS-CELIV sample structure is: ITO/d-a-a' donor (40 nm) /MgF$_2$

71

(15 nm)/Al. A waveform generator is used to shape the triangular voltage pulse that increases by 2 V in 200 μs, with an initial negative offset between 0 V and -4 V. The transient current is recorded by a digital oscilloscope. The signals of the antiBTDC and synBTDC samples are shown in Fig. 4.6a and b, that the extracted mobility for both donors are $3 \pm 2 \times 10^{-6}$ cm^{2}V^{-1}s^{-1}. The SCLC measurement of these two donors is then performed to fit the trap density of states (N_t) from the trap limited current and the conductivity (σ) obtained from the ohmic regime (Fig. 4.6c), with the sample structure: ITO/MoO$_3$ (15 nm)/d-a-a' donor (40 nm)/MoO$_3$ (15 nm)/Al.
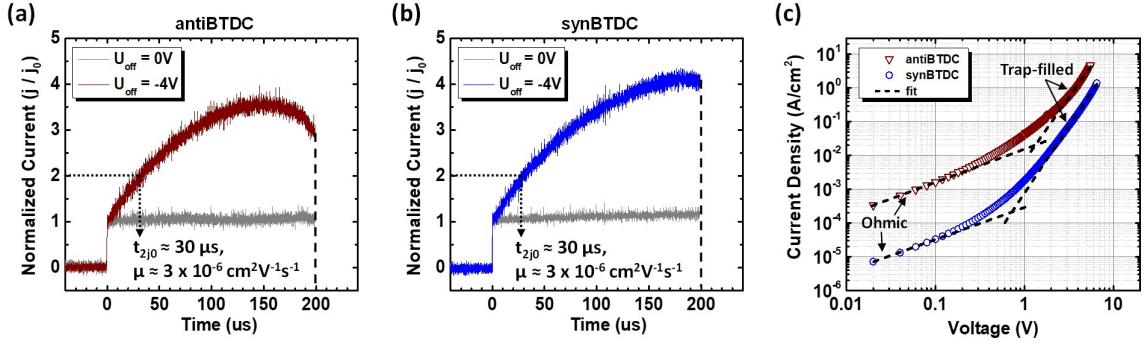
Figure 4.6: Hole mobility measurements of antiBTDC and synBTDC. (a) / (b) MIS-CELIV measurement. (c) SCLC measurement with the fit to the ohmic and trap-filled limit regimes.

In the ohmic regime indicated in Fig. 4.6c, there is linear relationship between current and voltage:

$$J_{ohm} = qp\mu \frac{V}{d}. \tag{4.1}$$

Here, p is the free carrier density, μ is the hole mobility, and d is the sample thickness. Assuming an exponential distribution of traps, the trap limited current is:[96]

$$J_{TFL} = q\mu N_v \left[\frac{\varepsilon m}{q(m+1)N_t} \right]^m \left[\frac{2m+1}{m+1} \right]^{m+1} \frac{V^{m+1}}{d^{2m+1}}, \tag{4.2}$$

where N_V is the HOMO density of states, N_t is the density of traps, $m = T_t/T$ where T_t is the characteristic trap temperature. N_V is set to 10^{21} cm^{-3}, a typical

value for organics; $\mu = 3 \times 10^{-6}$ cm^{2}V^{-1}s^{-1} as measured by MIS-CELIV. With Eq. 4.1 and 4.2, we fit the ohmic and the trap-filled limit current respectively of the two donor materials. The parameters obtained from the fits are listed in Table 4.5. The neat antiBTDC and synBTDC show similar $N_t \approx 8 \times 10^{18}$ cm^{-3} and 1×10^{19} cm^{-3} respectively, while synBTDC has more than one order of magnitude lower conductivity ($\sigma \approx 2 \times 10^{-9}$ S/cm) than antiBTDC ($\sigma \approx 5 \times 10^{-8}$ S/cm). As will see from the next section, it results in higher series resistance and hence lower FF of the synBTDC:C$_{70}$ cell than that of the antiBTDC:C$_{70}$ cell.

Table 4.5: Fitted parameters from SCLC mobility measurement.

Molecules	m	$N_t\ (cm^{-3})$	$p\ (cm^{-3})$	$\sigma\ (S/cm)$
antiBTDC	2.7 ± 0.1	8×10^{18}	1×10^{17}	5×10^{-8}
synBTDC	2.6 ± 0.3	1×10^{19}	3×10^{15}	2×10^{-9}

4.2.3 Device performance
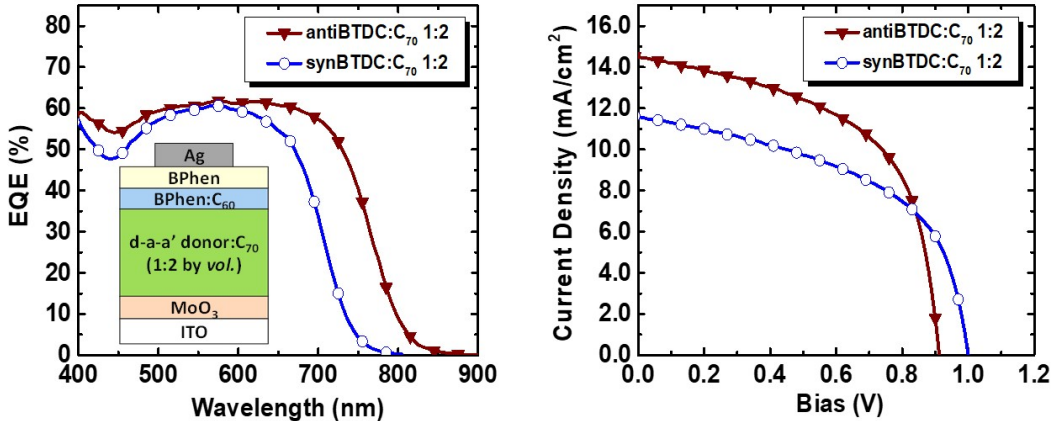
Figure 4.7: *EQE* and *J-V* characteristics of the optimized antiBTDC:C$_{70}$ and synBTDC:C$_{70}$ devices. *Inset*: device structure.

To examine the photovoltaic performance of the two regioisomeric donors, we mixed them with C$_{70}$ to form the active layer of the vacuum deposited OPV cells.

The optimized device structure as shown in Fig. 4.7, inset, is configured as follows: ITO/MoO$_3$ (10 nm)/d-a-a' donor:C$_{70}$ (1:2 ratio by vol.)/BPhen:C$_{60}$ (1:1 ratio by vol., 10 nm)/ BPhen (5 nm)/Ag (100 nm). Similar with the DTDCTB and DTDCPB cells, MoO$_3$ serves as the anode buffer. While the transparent exciton blocking and electron conducting buffer consists of a BPhen:C$_{60}$ (1:1) mixed layer capped with a neat BPhen layer adjacent to the cathode.[84] Both antiBTDC and synBTDC are mixed with C$_{70}$ with 1:2 ratio to achieve the highest *PCE*, with different optimized active layer thicknesses (60 nm and 50 nm thick, respectively). Atomic force microscopy (AFM) images of the d-a-a' donor:C$_{70}$ 1:2 mixtures are shown in Fig. 4.8. The two films exhibit similar surface morphologies, although synBTDC:C$_{70}$ shows a higher mean square roughness (R_q).
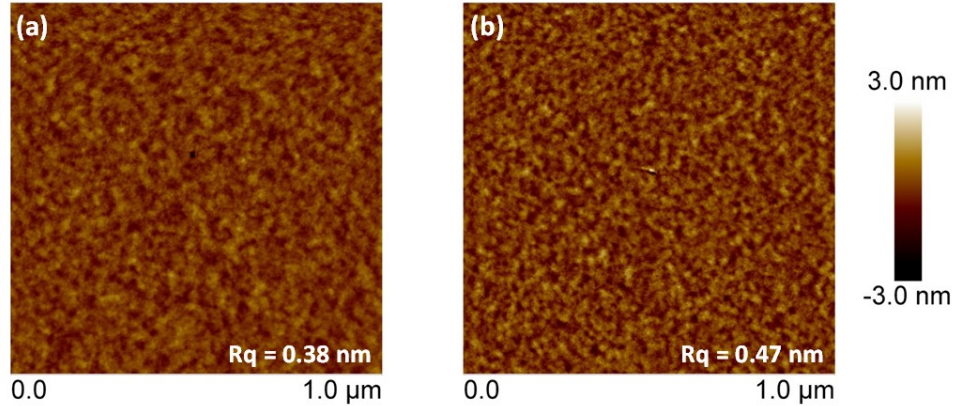
Figure 4.8: Atomic-force microscopy (AFM) images of (a) antiBTDC:C$_{70}$ 1:2 and (b) synBTDC:C$_{70}$ 1:2 blends. R_q refers to the mean square roughness.

The *EQE* vs. wavelength of OPVs employing these two donors are shown in Fig. 4.7 left. The antiBTDC:C$_{70}$ cell shows absorption extending to $\lambda = 820$ nm, while synBTDC:C$_{70}$ cell is blue shifted to $\lambda = 750$ nm. Figure 4.7 (right) shows the fourth quadrant *J-V* characteristics, with detailed device parameters listed in Table 4.6. The antiBTDC:C$_{70}$ cell exhibits $J_{SC} = 14.2 \pm 0.7$ mA/cm^2, $V_{OC} = 0.91 \pm 0.01$ V, $FF = 0.56 \pm 0.01$, and $PCE = 7.2 \pm 0.3\%$ under 1 sun intensity, AM 1.5G simulated solar illumination. The cross-conjugated synBTDC has reduced performance compared to

that of antiBTDC with $J_{SC} = 11.6 \pm 0.6$ mA/cm^2, $FF = 0.52 \pm 0.01$, and PCE = 6.1 $\pm$ 0.3%. However, the $V_{OC} = 1.01 \pm 0.01$ V of the synBTDC-based device is 0.1 V higher than that of its antiBTDC-based counterpart, due to the lower HOMO energy of the former.

Table 4.6: Device performance of antiBTDC, synBTDC and PYDC OPV cells.

Device	R_S ($\Omega \cdot cm^2$)	J_{SC} (mA/cm^2)	V_{OC} (V)	FF	PCE (%)
antiBTDC:C$_{70}$ (1:2, 60nm)	1.42 $\pm$ 0.04	14.2 $\pm$ 0.7	0.91 $\pm$ 0.01	0.56 $\pm$ 0.01	7.2 $\pm$ 0.3
synBTDC:C$_{70}$ (1:2, 50nm)	1.86 $\pm$ 0.04	11.6 $\pm$ 0.6	1.01 $\pm$ 0.01	0.52 $\pm$ 0.01	6.1 $\pm$ 0.3
PYDC:C$_{70}$ (1:2, 50nm)	3.26 $\pm$ 0.07	10.1 $\pm$ 0.5	1.06 $\pm$ 0.01	0.48 $\pm$ 0.01	5.1 $\pm$ 0.2

The peak EQE of 60% for both antiBTDC:C$_{70}$ and synBTDC:C$_{70}$ cells indicates similar charge collection efficiencies, which implies that the differences in morphologies of the two blends are not critical to the differences in their current densities. The cross-conjugation of synBTDC results in reduced inter- and intra-molecular charge transfer, and a larger energy gap compared with antiBTDC. Consequently, its HOMO level shifts to lower energy, thereby increasing V_{OC}. The lower efficiency of the synBTDC:C$_{70}$ cell primarily resulting from the lower current density is therefore due to its absorption cutoff that does not extend as deeply into the NIR. The PCE = 6.1 $\pm$ 0.3%, however, is one of the highest efficiencies achieved among OPVs with $V_{OC} > 1.0$ V, which is advantageous for applications in high voltage multi-junction photovoltaic cells.

We have shown that the cross conjugation effect of antiBTDC and synBTDC determine, to a limited extent, V_{OC} of heterojunctions comprising C_{70}. To further examine the influence of molecular structure on V_{OC}, a d-a-a' donor PYDC (see
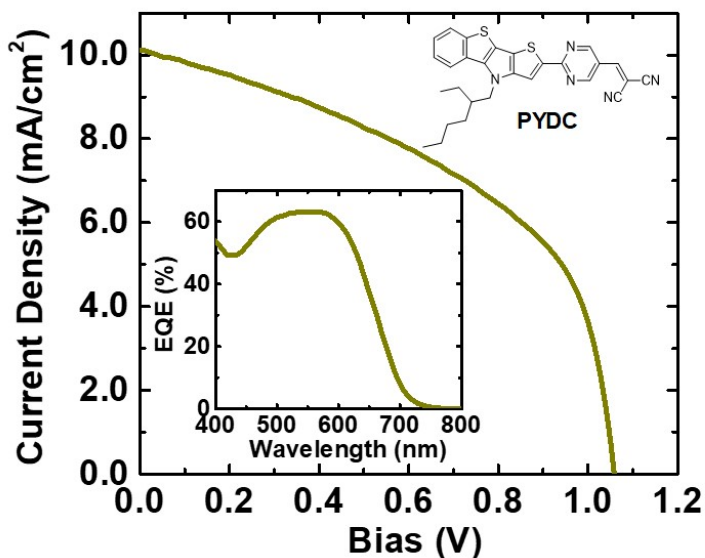
Figure 4.9: PYDC:C$_{70}$ 1:2 OPV cell *J-V* characteristics. *Inset:* Molecular structural formula of PYDC, and its *EQE* spectrum.

Fig. 4.9, inset) was synthesized. In this molecule, the benzothiadiazole block in antiBTDC is replaced with a pyrimidine unit. Due to the reduced quinoidal character of pyrimidine, the absorption of PYDC shifts to shorter wavelengths with an onset at $\lambda = 600$ nm, indicating an increased optical energy gap of 2.05 ± 0.05 eV. The PYDC:C$_{70}$ cell employs the same structure as antiBTDC:C$_{70}$ and synBTDC:C$_{70}$, with an active layer thickness of 50 nm. The *EQE* spectrum and *J-V* characteristics are shown in Fig. 4.9, with device parameters summarized in Table 4.6. The PYDC:C$_{70}$ cell exhibits a relatively narrow absorption spectrum, leading to the lowest $J_{SC} = 10.1 \pm 0.7$ mA/cm^2 among the three donor molecules. However, with the central pyrimidine unit, the PYDC-based OPV achieves a higher $V_{OC} = 1.06 \pm 0.01$ V, with $FF = 0.48 \pm 0.01$ and $PCE = 5.1 \pm 0.2\%$. The series resistances (R_S) of the devices with different donors obtained from the *J-V* characteristics are also listed in Table 4.6, which accounts for the trends observed in *FF*; *i.e.* as R_S increases, *FF* decreases.

4.2.4 Photoluminescence (PL)
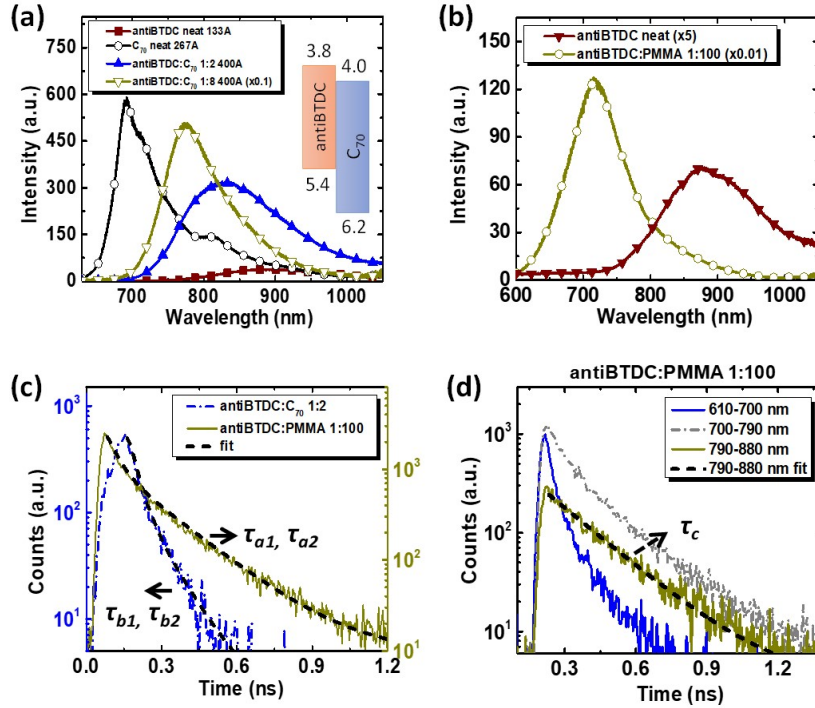
Figure 4.10: Steady-state and transient photoluminescence (PL) of antiBTDC neat and mixed films. a) Steady-state PL spectra of antiBTDC neat donor, donor:C_{70} blends, and neat C_{70}. b) PL spectra of 1% antiBTDC diluted in a PMMA matrix, and as a neat film. c) Time-resolved transient PL of antiBTDC:PMMA 1:100, and antiBTDC:C_{70} 1:2 blends. d) Wavelength-resolved transient PL of antiBTDC:PMMA. All measurements are conducted at room temperature. The time constants obtained from the fits (dashed lines) are: $\tau_{a1} = 40 \pm 10$ ps, $\tau_{a2} = 200 \pm 20$ ps; $\tau_{b1} = 30 \pm 10$ ps, $\tau_{b2} = 120 \pm 10$ ps; $\tau_c = 210 \pm 20$ ps.

Steady-state PL spectra of antiBTDC and synBTDC are shown in Fig. 4.10 and Fig. 4.11, respectively, along with their HOMO and LUMO energies relative to those of C_{70} (insets). The neat C_{70} emission spectrum is also depicted in Fig. 4.10a for reference. When excited at $\lambda = 442$ nm, the antiBTDC film exhibits a NIR emission peak at $\lambda = 870$ nm, while the synBTDC film emits with the peak at $\lambda = 800$ nm. In both cases, the PL emission from the C_{70} blends are blue shifted by approximately 50 nm with several times higher intensity compared with the neat donor film. As we increase the antiBTDC:C_{70} blend ratio from 1:2 to 1:8, the emission is further blue-
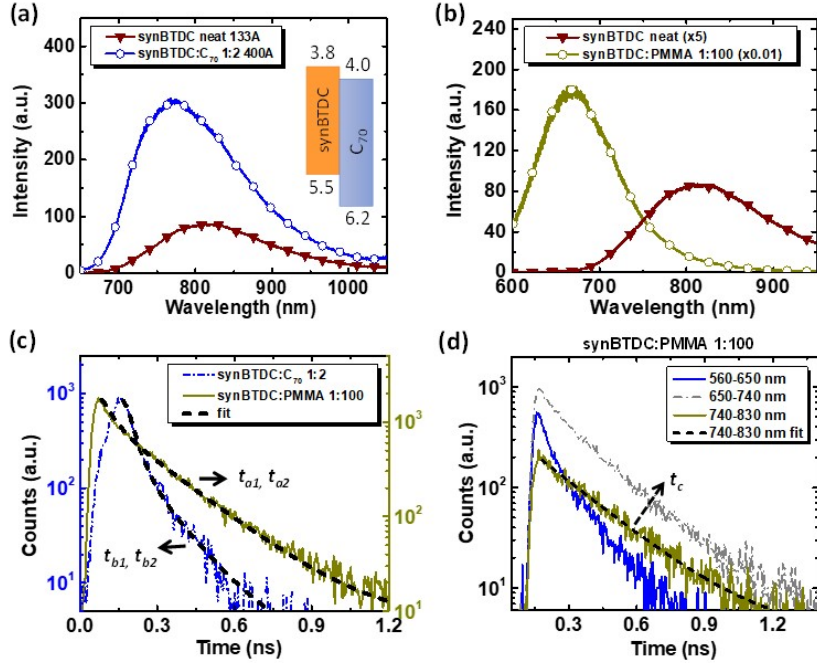
Figure 4.11: Steady-state and transient PL of synBTDC neat and mixed films, at room temperature. Details are the same with the above figure for antiBTDC. The time constants obtained from the fits (dashed lines) are: $t_{a1} = 50 \pm 10$ ps, $t_{a2} = 200 \pm 20$ ps; $t_{b1} = 30 \pm 10$ ps, $t_{b2} = 130 \pm 10$ ps; $t_c = 230 \pm 20$ ps.

shifted and the intensity increases by more than ten times (Fig. 4.10a). To understand this phenomenon, antiBTDC and synBTDC are diluted in poly(methyl methacrylate) (PMMA) with a 1:100 weight ratio to suppress intermolecular interactions. As shown in Fig. 4.10b, the emission wavelength of the antiBTDC:PMMA film is 150 nm shorter as compared to that of the neat antiBTDC film along with two orders of magnitude higher intensity. Similarly, there is a 150 nm blue shift in the case of synBTDC:PMMA film emission (Fig. 4.11b).

The time-resolved transient PL of antiBTDC-based films blended with PMMA (1:100) and C_{70} (1:2), respectively, were examined and then fit to biexponential time decays as shown in Fig. 4.10c. The time constants of antiBTDC:PMMA emission obtained from the fits are $\tau_{a1} = 40 \pm 10$ ps and $\tau_{a2} = 200 \pm 20$ ps, while the parameters for antiBTDC:C_{70} are $\tau_{b1} = 30 \pm 10$ ps and $\tau_{b2} = 120 \pm 10$ ps. The neat antiBTDC donor film, on the other hand, shows a single exponential time decay of

78
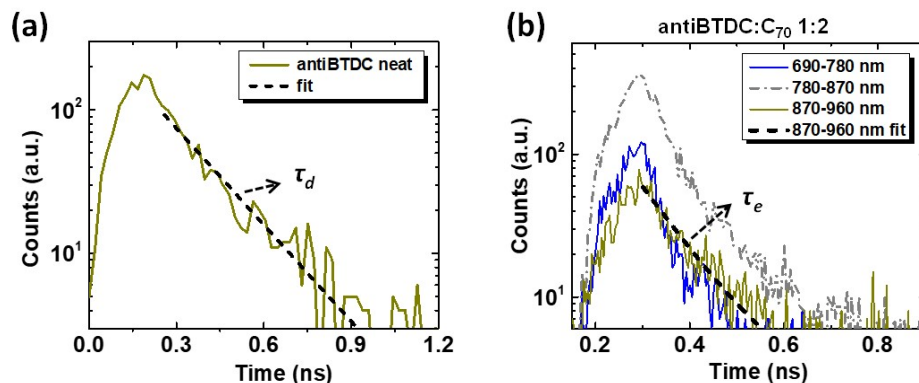
Figure 4.12: Transient PL emissions of antiBTDC. a) Transient PL emission of an antiBTDC film with a single exponential fit (dashed line). b) Wavelength-resolved transient PL of antiBTDC:C_{70} 1:2 blend film. Measurements are conducted at room temperature. Time constants obtained from the fits: $\tau_d = 190 \pm 30$ ps, $\tau_e = 100 \pm 20$ ps.

$\tau_d = 190 \pm 30$ ps (Fig. 4.12a). Figures 4.10d and 4.12b depict the transient emission of antiBTDC:PMMA and antiBTDC:C_{70} films at different wavelength intervals. The decay becomes slower at longer wavelengths. As indicated by the dashed line in Fig. 4.10d, the antiBTDC:PMMA emission between $\lambda = 790$ to 880 nm has a single exciton lifetime of $\tau_c = 210 \pm 20$ ps. The films of synBTDC mixed with PMMA and C_{70} showed similar transient behaviors (see Fig. 4.11c and d).

Mixing of the d-a-a' donor compounds in the non-polar PMMA matrix eliminates solvation effects in the molecular emission spectra.[97] We therefore deduce that the hypsochromic shifts of the fluorescence in Fig. 4.10b and Fig. 4.11b of antiBTDC or synBTDC diluted in PMMA, respectively, are due to the emergence of monomer, in contrast to excimer emission in neat d-a-a' thin films. The blue-shifted PL of the antiBTDC:C_{70} 1:8 blend compared with the 1:2 blend shown in Fig. 4.10a suggests singlet emission with two possibilities: (i) more pronounced antiBTDC monomer vs. excimer emission as it is diluted in the blend; or (ii) direct emission from C_{70}. As seen from the energy level diagram in the insets of Figs. 4.10a and Fig. 4.11a, the large differences in HOMO energies between antiBTDC or synBTDC and C_{70} facilitates efficient dissociation of excitons injected from the C_{70} side of the heterojunction.

However, their similar LUMO energies with an offset smaller than 0.3 eV is insufficient to result in efficient exciton dissociation, causing back charge transfer to the d-a-a' molecule followed by donor fluorescence. We conclude, therefore, that the singlet emission observed from the blends originates from the donor itself.

The transient PL further clarifies the origin of the spectral features in the PMMA and C_{70} blends. The antiBTDC:PMMA emission at $\lambda = 790$ to 880 nm corresponds to antiBTDC excimer fluorescence as observed in the neat antiBTDC film. It shows an exponential decay with the characteristic exciton lifetime of $\tau_c = 210 \pm 20$ ps (Fig. 4.10d dashed line), which matches the $\tau_{a2} = 200 \pm 20$ ps obtained from the antiBTDC:PMMA transient PL. It is also nearly identical to the neat antiBTDC lifetime of $\tau_d = 190 \pm 30$ ps as shown in Fig. 4.12a. The emission from antiBTDC:PMMA therefore contains both monomer and excimer emission components, contributing to the shorter τ_{a1} and the longer τ_{a2}, respectively, in Fig. 4.10c. The PL emission of antiBTDC:C_{70}, on the other hand, decays faster than antiBTDC:PMMA and is dominated by the shorter lifetime component of $\tau_{b1} = 30 \pm 10$ ps, very close to that for antiBTDC monomer emission, τ_{a1}. In Fig. 4.12b we show the existence of long-wavelength emission with $\tau_e = 100 \pm 20$ ps, corresponding to $\tau_{b2} = 120 \pm 10$ ps in Fig. 4.10c. It is due to both antiBTDC excimer (τ_{a2}) and charge transfer state (CT) emission at the donor-acceptor interfaces (τ_{CT}), i.e.:

$$\frac{1}{\tau_{b2}} = \frac{1}{\tau_{a2}} + \frac{1}{\tau_{CT}}. \tag{4.3}$$

Now τ_{b2} is approximately 0.5 τ_{a2}, giving $\tau_{CT} \approx \tau_{a2} \approx 200$ ps. The emission intensities, however, are lower than the monomer donor emission even in the donor-acceptor blend.

The considerable donor emission from the donor:C_{70} blends suggests incomplete exciton dissociation at the donor-acceptor interfaces, with charge back-transferring to the donor molecule. This results in exciton dissociation within the donor domains,

which reduces the cell shunt resistance (R_{sh}). Therefore a linear increase of photocurrent under reverse bias is observed in the J-V characteristics, resulting in $R_{sh} \approx 500$ $\Omega \, cm^2$ and $FF < 0.60$ for both antiBTDC and synBTDC devices.[98] A higher LUMO energy for more efficient exciton dissociation is expected to improve the FF, although the current density may be reduced.

4.2.5 Conjugation length *vs* V_{OC}
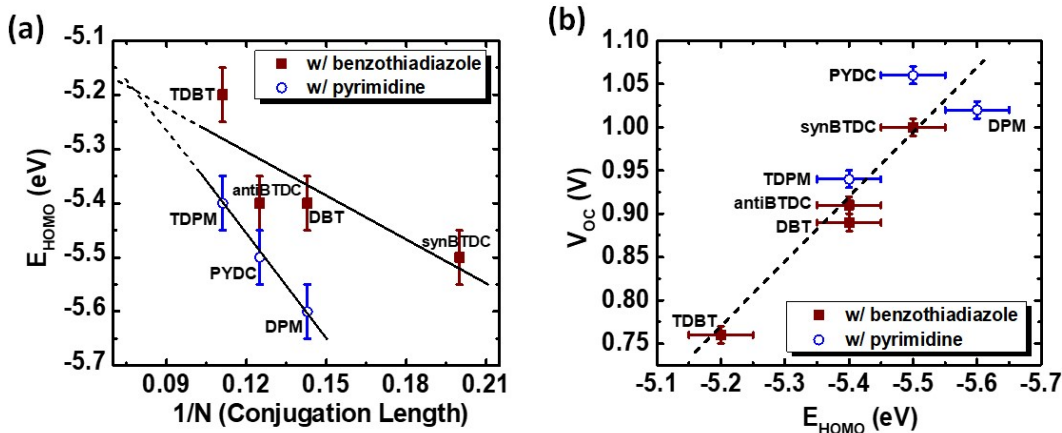
Figure 4.13: Conjugation length *vs.* V_{OC}. a) Highest occupied molecular orbital energy (E_{HOMO}) *vs.* reciprocal of the backbone conjugation length (1/N) of a series of DTP- and heterotetracene-based d-a-a' donor molecules. b) V_{OC} vs. donor E_{HOMO} for d-a-a':C_{70} heterojunctions.

The heterotetracene-based d-a-a' donors discussed above and the previously reported DTP-based d-a-a' donor molecules[88] all contain a benzothiadiazole or pyrimidine central electron-withdrawing block, bridging the a' unit of dicyanovinylene and an electron-donating aryl-substituted or benzene-fused DTP group. The molecular conjugation length (N) is defined as the number of double bonds along the shortest path connecting the terminal carbon atoms of the backbone[99], that varies from 5 to 9 with the molecules we analyzed. Figure 4.13a summarizes the HOMO energies (E_{HOMO}) of these molecules as a function of *1/N*. The molecules with benzothiadiazole is shown by solid squares, while those with pyrimidine are shown by open circles.

Here, E_{HOMO} is chosen instead of commonly used electron transition energies since the conjugation length of both molecular groups is only adjusted by modifying their electron-donating unit that primarily affects the HOMO energy. An approximately linear relationship is observed between E_{HOMO} and $1/N$ that can be explained by the free electron model.[100] The longer conjugation (smaller *1/N*) leads to more extended π-electron orbitals, resulting in red-shifted absorption and a shallower HOMO. With reduced quinoidal character, the molecules with pyrimidine generally exhibit larger energy gaps and deeper HOMO levels than their benzothiadiazole counterparts with the same N (PYDC-antiBTDC; DPM-DBT; TDPM-TDBT), and their HOMO levels are more sensitive to changes in conjugation, as indicated by the larger fitted slope. The crossing point of the two fits at $N = 13$ (Fig. 4.13a) indicates an upper limit of $E_{HOMO} = $ -5.2 eV. Like polymers, extended molecules are subject to kinetically induced disruptions (e.g. twists or kinks) in the backbone, limiting the spatial extent of the orbitals in excited state. Nevertheless, it is apparent that further tuning of the E_{HOMO} energy is possible for $N > 9$ reported here, which offers a design approach for achieving NIR absorbing donor molecules.

From Fig. 4.13b, a deeper HOMO (*i.e.* smaller N) generally leads to an increased V_{OC}. The π-conjugation of antiBTDC is reduced compared with TDBT, with V_{OC} increased from 0.76 ± 0.01 V to 0.91 ± 0.01 V. With a fused benzene ring on the DBT molecule, antiBTDC achieves closer packing motifs than TDBT, resulting in a decreased transfer energy, and hence an increase in *FF*, from 0.46 ± 0.01 to 0.56 ± 0.01. Similar to antiBTDC, PYDC benefits from the improved molecular stacking over TDPM. It also achieves a higher $V_{OC} = 1.06 \pm 0.01$ V. Further, DPM, with a relatively small $N = 7$, has the largest $E_{HOMO} = $ -5.6 $\pm$ 0.05 eV of this group. However, the low $FF = 0.33 \pm 0.01$ indicates poor charge transfer due to the unprotected electroactive carbon that limits V_{OC} compared with PYDC. The synBTDC-based device has $V_{OC} = 1.01 \pm 0.01$ V, which is 0.1 V higher than antiBTDC and the smallest $N = 5$ achieved

by interrupting the antiBTDC conjugation with the flipped thiophene unit within the molecular backbone. Such cross conjugation effectively reduces the molecular conjugation and leads to a higher V_{OC}. Among all of the molecules discussed, the slope of the expected linear relationship of V_{OC} to E_{HOMO} energy is 0.75 ± 0.13 C^{-1}, as indicated in Fig. 4.13b.
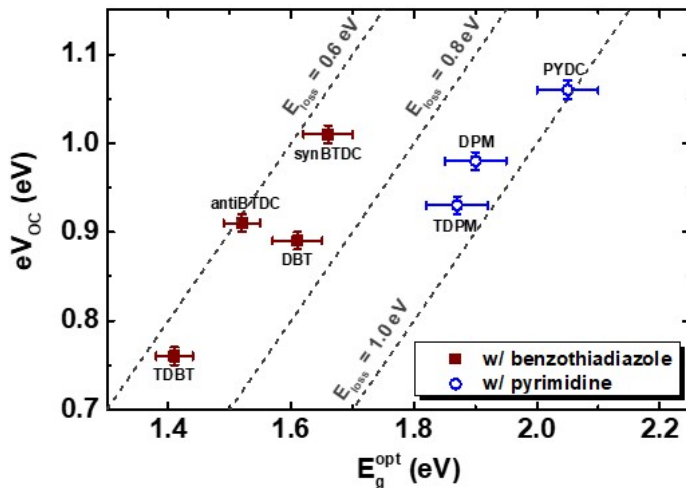
Figure 4.14: eV_{OC} *vs.* E_g^{opt} (optical energy gap) of the d-a-a' molecules, estimated from the absorption onset of the thin films. The dashed lines indicate E_{loss} (*i.e.* E_g^{opt} - eV_{OC}) of 0.6, 0.8 and 1.0 eV respectively.

The photon energy loss, E_{loss}, which is the difference between eV_{OC} and the lowest absorbed photon energy of the devices employing these donors is shown in Fig. 4.14. The E_{loss} of the donors with benzothiadiazole central 'a' unit all fall into the region between 0.6 and 0.8 eV, while the molecules with pyrimidine show E_{loss} between 0.8 and 1.0 eV. The antiBTDC and synBTDC exhibit $E_{loss} < 0.7$ eV, which is relatively small for organic solar cells.

4.2.6 Summary

In conclusion, the above analysis in this section elucidated the structure-property-performance relationships of highly dipolar d-a-a' small molecules used in organic donor-acceptor heterojunctions. Specifically, the molecules introduced with anti and

syn asymmetric heteroacenes as coplanar donors of BTDC were used to investigate molecular regioisomeric effects on photogeneration efficiency when blended with fullerene acceptors. Both molecules pack in an antiparallel arrangement to achieve a centroymmetric dimer, leading to a net dipole moment of zero. The synBTDC with a shorter backbone conjugation length exhibits a larger bond length alternation (BLA), a higher angle slipped staircase-like crystal stacking and reduced intra- and intermolecular charge transfer compared with antiBTDC. An optimized OPV based on antiBTDC:C_{70} blend achieves $V_{OC} = 0.91 \pm 0.01$ V, $FF = 0.56 \pm 0.01$ and PCE = $7.2 \pm 0.3\%$. Despite the reduced charge transfer and blue-shifted absorption which lead to smaller J_{SC}, synBTDC shows a lower HOMO energy with higher $V_{OC} = 1.01 \pm 0.3$ V, with a power conversion efficiency of $6.1 \pm 0.3\%$. The design of PYDC leads to a further enhanced $V_{OC} = 1.06 \pm 0.01$ V due to the reduced quinoidal character of pyrimidine.

It is found that the V_{OC} of the d-a-a donor:C_{70} devices is a function of the donor conjugation length: a reduction of backbone conjugation lowers the HOMO level for both groups of molecules with embedded benzothiadiazole or pyrimidine central 'a' unit, leading to an enlarged donor-acceptor HOMO-LUMO gap and a larger V_{OC}. The OPVs with antiBTDC and synBTDC donors show a photon energy loss < 0.7 eV, while the singlet donor PL emission in blends with C_{70} implies inefficient exciton dissociation at the donor-acceptor interface and possible back transfer resulting in relatively low FFs. Shortening the alkyl chains, or raising their LUMO energy for more complete exciton dissociation may lead to further improvements in FF, and ultimately the device performance. In the next section, we will study a group of d-a-a' donors with different side chain configurations, that the device performance is improved to $PCE > 9.0\%$.

4.3 Side-chain effects of d-a-a' donors

In the previous section we described the effects of cross-conjugation of d-a-a' small molecule donors on the open circuit voltages (V_{OC}) of fullerene-based OPVs. Modification of the side chain length also serves as an effective approach to optimize the small molecule OPV performance. For example, Bäuerle *et al.* altered the side chains linked to the donor moiety of a-d-a configured molecules with propyl, hexyl and p-tolyl groups.[101] The changes induced in morphology led to an increase in *PCE* from 3.7% to 5.6% as the alkyl chain lengths decreased (hexyl vs. propyl). Moreover, it has been reported that subtle variations of molecular alkyl substitutions affects the tendency for crystallization.[102] Yet, molecules with shortened side chains are difficult to purify by column chromatography because of their insufficient solubility in common organic solvents. Therefore, there is a trade-off between desired material properties and processability. This section will introduce two d-a-a' small molecules that possess the same backbone structure as antiBTDC, to analyze the effects of side chains on device performance.

4.3.1 Molecular crystal structures

The molecules iBuBTDC and nBuBTDC are shown in Fig. 4.15. They share the same backbone structure as antiBTDC, while iBuBTDC possesses a shorter branched isobutyl chain and nBuBTDC has an n-butyl chain. The alkyl chains of iBuBTDC and nBuBTDC are smaller than antiBTDC but still provide sufficient solubility during column chromatography purification.

The different lengths and shapes of the side chains of antiBTDC, iBuBTDC and nBuBTDC shown in Fig. 4.15 (indicated by red circles) result in different molecular conformations between the central thiophene and the benzothiadiazole acceptor units along the intervening C-C single bond that connects them. The antiBTDC exhibits a s-trans arrangement (Fig. 4.15a, blue circles), while iBuBTDC and nBuBTDC are
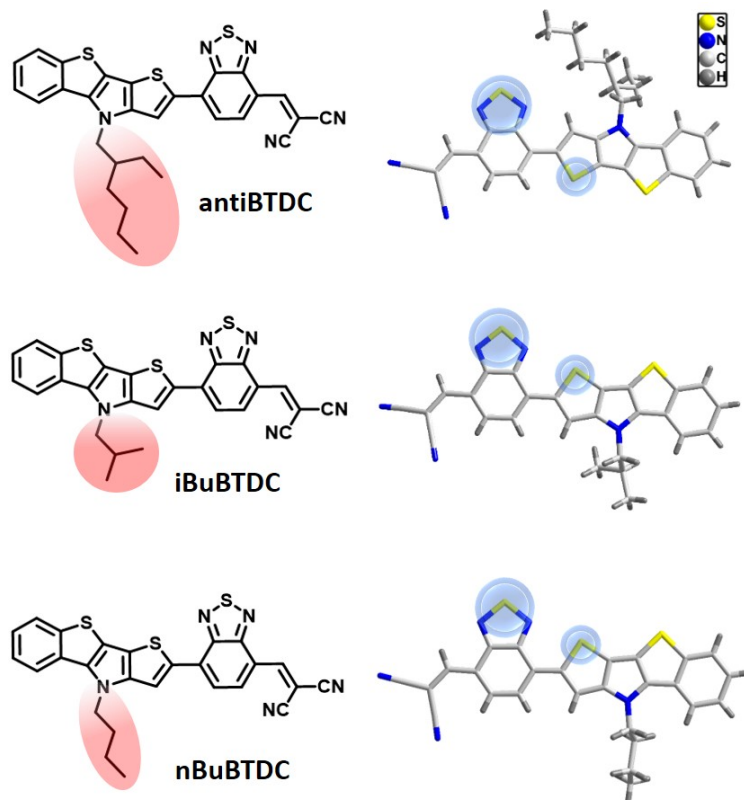
Figure 4.15: (left) Molecular structural formula and (right) atomic arrangements of antiBTDC, iBuBTDC and nBuBTDC.

s-cis conformation (Fig. 4.15b and c). The electronic transition parameters computed from DFT are listed in Table 4.7. The three donors possess similar HOMO and LUMO energies, and lowest energy singlet ground-to-excited state transition ($S_1 \leftarrow S_0$) molecular orbital (MO) compositions (98% HOMO→LUMO, plus 2% HOMO-1→LUMO). The oscillator strengths (f) of the $S_1 \leftarrow S_0$ transition are also similar, with $f \sim 1.1$.

The antiparallel arrangement of centrosymmetric dimer stacks is observed in crystals of all three molecules due to the large ground state dipole moment of > 10 D. Figure 4.16 shows the packing configurations of the donor molecules with structural parameters summarized in Table 4.8. The molecules with different side chains show similar average intermolecular π-π distances of between 3.44 to 3.49 $\mathring{A}$. A dihedral angle of 8.8° between the thienoacene donor and benzothiadiazole acceptor is observed in antiBTDC, while both iBuBTDC and nBuBTDC present almost perfect copla-

Table 4.7: Computed $S_1 \leftarrow S_0$ parameters of antiBTDC, iBuBTDC and nBuBTDC.

Molecule	λ_{calc} (nm) [a]	HUMO/ LUMO (eV) [a]	f [b]	MO composition (Λ) [c]
antiBTDC	676	-5.36/-3.33	1.12	98% HOMO→LUMO 2% HOMO-1→LUMO
iBuBTDC	676	-5.33/-3.33	1.09	98% HOMO→LUMO 2% HOMO-1→LUMO
nBuBTDC	678	-5.33/-3.33	1.10	98% HOMO→LUMO 2% HOMO-1→LUMO

[a] Calculated from the $S_1 \leftarrow S_0$ transition.
[b] Oscillator strength.
[c] Molecular orbital (MO) compositions in terms of the corresponding contribution.
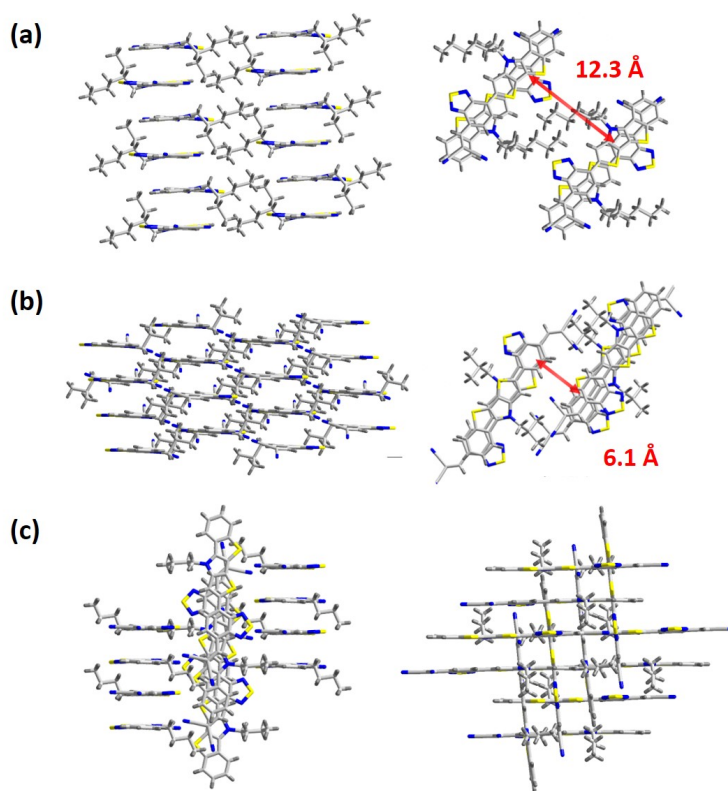
Figure 4.16: Crystal packing configurations of a) antiBTDC, b) iBuBTDC and c) nBuBTDC. The intermolecular interplanar spacings of antiBTDC and iBuBTDC are indicated by the red arrows.

Table 4.8: Crystal packing parameters of antiBTDC, iBuBTDC and nBuBTDC.

Crystal parameter	antiBTDC	iBuBTDC	nBuBTDC
Crystal system	Triclinic	Triclinic	Monoclinic
Dihedral angle (°)	8.8	3.4	2.0
Average intermolecular π-π distance ($\overset{\circ}{A}$)	3.47	3.44	3.49
Packing density (g/cm^3)	1.407	1.496	1.469

nar conformations with dihedral angles of 3.4° and 2.0° , respectively. The longer alkyl chain of antiBTDC separates the adjacent π-π stacks with a distance of 12.3$\overset{\circ}{A}$ (Fig. 4.16a), while iBuBTDC tends to pack more compactly, with a distance of 6.1$\overset{\circ}{A}$ between adjacent stacks (Fig. 4.16b). The nBuBTDC, however, forms orthogonal stacks, as shown in Fig. 4.16c. The packing densities of iBuBTDC and nBuBTDC are 1.496 g/cm^3 and 1.469 g/cm^3, respectively, which is considerably higher than that of antiBTDC (1.407 g/cm^3).

The results above lead to the conclusion that the d-a-a' molecules with different side chain configurations lead to different optical and electrical properties in their thin films. The smaller isobutyl and n-butyl chains attached to the backbones of iBuBTDC and nBuBTDC, respectively, provide less steric hindrance then the 2-ethylhexyl chain of antiBTDC, resulting in smaller dihedral angles between the benzothiadiazole acceptor group and the thienoacene donor unit. The same calculated oscillator strength associated with the $S_1 \leftarrow S_0$ transition of the three donor molecules, however, indicates a similar degree of molecular orbital overlap. This confirms that the side chains do not have a direct impact on the electronic coupling between the donor and acceptor units along the molecular backbone, and thus on the intramolecular charge transfer. The cyclic voltammograms of iBuBTDC and nBuBTDC are similar to that of antiBTDC, suggesting that the electrochemical properties are also not significantly affected by the side chains. The differences in absorption coefficient as well as device

performance, therefore, are more closely related to intermolecular charge transfer and the packing morphologies.

4.3.2   Physical parameters
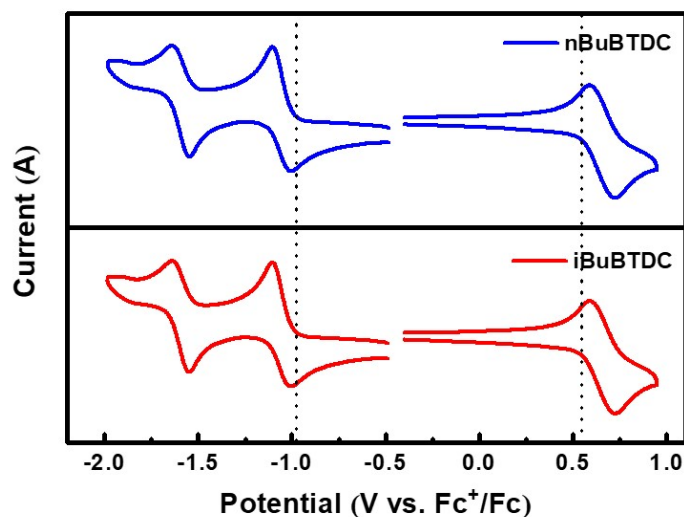
Figure 4.17: Cyclic voltammograms (CV) of nBuBTDC and iBuBTDC. It is referenced to the Ferrocenium/Ferrocene (Fc$^+$/Fc) redox couple, where the HOMO of Fc is assigned to be -4.8 eV relative to the vacuum level.

Table 4.9: Physical parameters of antiBTDC, iBuBTDC and nBuBTDC.

Molecules	$\lambda_{onset,film}$ (nm)	$E_{g,opt}$ (eV)^a	ΔE_{CV} (eV)^b	HOMO (eV)	LUMO (eV)	T_d (˚C)^f
antiBTDC	815	1.52	1.52	-5.40^c	-3.88^d	331
iBuBTDC	809	1.53	1.52	-5.35^e	-3.83^e	339
nBuBTDC	809	1.53	1.52	-5.35^e	-3.83^e	341

^{a} Optical bandgap estimated from the film absorption onset.
^{b} Electrochemical bandgaps, calculated from CV.
^{c} HOMO level measured in CH_2Cl_2.
^{d} LUMO Measured in THF.
^{e} Measured in CH_2ClCH_2Cl.
^{f} Decomposition temperature, obtained by thermogravimetric analysis (TGA).

Cyclic voltammograms (CV) of iBuBTDC and nBuBTDC are shown in Fig. 4.17. The HOMO and LUMO energies for both iBuBTDC and nBuBTDC based on the

oxidation potential and the first reduction potential are -5.35 eV and -3.83 eV, respectively. Figure 4.18 presents the absorption coefficients of the donor films. The molecules all show absorption between wavelengths of $\lambda = 450$ and 800 nm, with a peak at $\lambda = 620$ nm. This is consistent with the energy gap of 1.52 eV measured by CV (Table 4.9). The absorption coefficient of iBuBTDC is slightly larger than nBuBTDC, both of which are about 20% higher than antiBTDC (Fig, 4.18), which can be attributed to the higher packing density of the former molecules. In addition, all the molecules have thermal decomposition temperatures (T_d, corresponding to 5% weight loss) of 340-350 °C measured by thermogravimetric analysis. The detailed photophysical and electrochemical parameters of the molecules are summarized in Table 4.9.
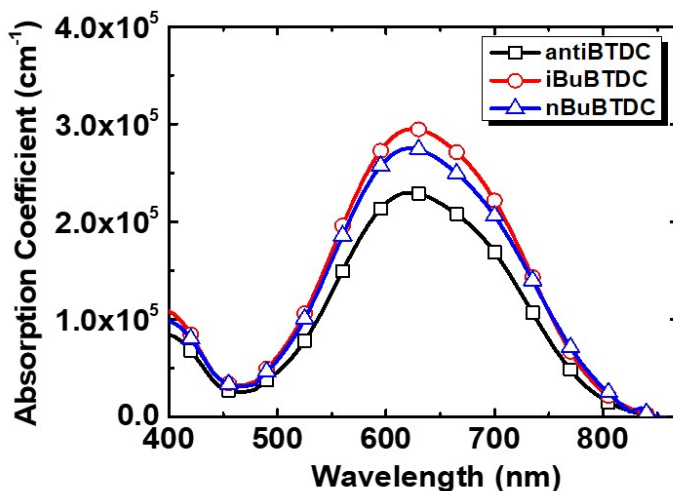
Figure 4.18: Absorption coefficients of antiBTDC, iBuBTDC and nBuBTDC.

The dipolar d-a-a' molecules tend to form dimer units that are packed in a slipped-stack manner as presented in the prevous subsection. All three donors form long-range π-stacked networks as shown in Fig. 4.16. The closer crystal packing distance between iBuBTDC molecules and thus higher packing density due to its shorter isobutyl side chain (Fig. 4.16b) leads to a higher absorption coefficient than the other two molecules studied, followed by the nBuBTDC with slightly lower packing density. The

relatively long, branched side chain of antiBTDC leads to the lowest density. The higher absorption of iBuBTDC and nBuBTDC over antiBTDC also lead to higher J_{SC} as will be shown by the device performance below.

4.3.3 Device performance
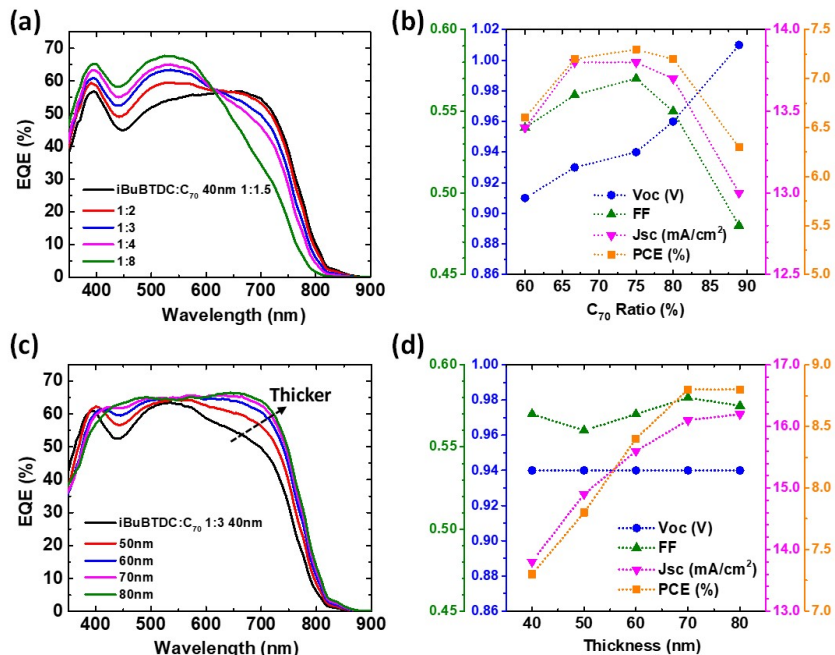
Figure 4.19: **Optimization of the iBuBTDC:C_{70} cells.** a)/c)EQE and b)/d) device parameter plots with different donor:acceptor ratios and active layer thicknesses. The active layer thickness of a) and b) is fixed at 40 nm; the D:A ratio of c) and d) is fixed at 1:3.

The OPV devices are fabricated with the structure as follows: ITO/MoO$_3$ (10 nm)/d-a-a' donor:C_{70} /BPhen:C_{60} (1:1 ratio by vol., 10 nm)/ BPhen (5 nm)/Ag (100 nm). The active layers are optimized in terms of D:A ratios and thickness. Taking iBuBTDC:C_{70} as an example, As the C_{70} ratio increases, the photo response in green increases while the NIR part decreases (Fig. 4.19a). As seen from the device parameter plot of iBuBTDC:C_{70} cell with fixed active layer thickness of 40 nm in Fig. 4.19b, the V_{OC} gradually increases while PCE is dominated by the FF that reaches

its maximum value at 1:3 ratio.

The active layer thicknesses are then optimized with the D:A ratio fixed at 1:3. From Fig. 4.19c, as the active layer becomes thicker, the EQE grows both in the green and the NIR region with a fixed point of 60% at 530 nm. It eventually leads to very flat photo response over the wavelength between 400 and 700 nm. The device parameter is plotted as a function of active layer thickness (Fig. 4.19d). The $V_{OC} = 0.94$ V does not change with the thickness, while the FF fluctuates in a very small range between 0.56 and 0.58. The J_{SC} gradually increases and reaches the peak value at the thickness of 70-80 nm. The overall PCE turns to a saturated point at 70 nm. All three donors present the optimized D:A ratio of 1:3 and active layer thickness of 70 to 80 nm.
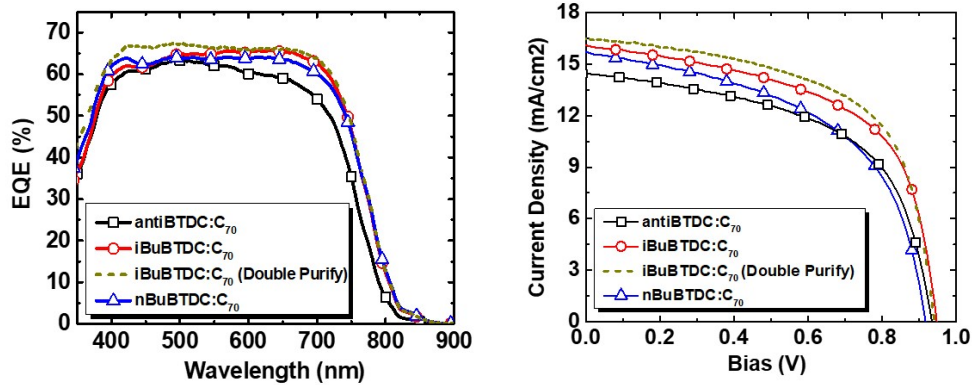
Figure 4.20: EQE (left) and J-V (right) characteristics of antiBTDC, iBuBTDC and nBuBTDC cells.

The EQE and J-V characteristics of the three optimized d-a-a' OPV devices with 1:3 donor:acceptor (D:A) ratio and 70 nm active layer are compared in Fig. 4.20 (solid lines), with details summarized in Table 4.10. All three cells exhibit photoresponse between wavelengths of $\lambda = 350$ to 800 nm, with $V_{OC} > 0.9$ V. The iBuBTDC (red circle) cell shows the highest response in the NIR region with EQE $\sim 65\%$ at 650 nm. The J_{SC} of iBuBTDC:C_{70} and nBuBTDC:C_{70} are 16.1 ± 0.8 mA/cm² and 15.7 ± 0.8 mA/cm², respectively, compared to 14.4 ± 0.7 mA/cm² for antiBTDC:C_{70}.

Table 4.10: Device performance of antiBTDC, iBuBTDC and nBuBTDC mixed with C_{70}.

Device	J_{SC} (mA/cm^2)	V_{OC} (V)	FF	PCE (%)
iBuBTDC:C_{70}	16.1 ± 0.8	0.94 ± 0.01	0.58 ± 0.01	8.8 ± 0.5
	16.5 ± 0.8	0.94 ± 0.01	0.60 ± 0.01	$9.3 \pm 0.5^*$
nBuBTDC:C_{70}	15.7 ± 0.7	0.92 ± 0.01	0.52 ± 0.01	7.5 ± 0.4
antiBTDC:C_{70}	14.4 ± 0.7	0.93 ± 0.01	0.56 ± 0.01	7.5 ± 0.4

* iBuBTDC with additional temperature-gradient sublimation.

With a higher J_{SC} but lower FF than antiBTDC:C_{70}, the nBuBTDC:C_{70} gives a similar $PCE = 7.5 \pm 0.4\%$ at 1 sun, AM 1.5G illumination. On the other hand, the iBuBTDC device achieves $FF = 0.58 \pm 0.01$ and $PCE = 8.8 \pm 0.5\%$, the highest among the three donors. Further improvement of the iBuBTDC device performance is achieved by additional purification of the source material using temperature-gradient sublimation[103], resulting in an increase in FF from 0.58 ± 0.01 to 0.60 ± 0.01. The iBuBTDC:C_{70} cell with 80 nm thick active layer grown from the purified iBuBTDC achieves $PCE = 9.3 \pm 0.5\%$, with $J_{SC} = 16.5 \pm 0.8$ mA/cm2, $V_{OC} = 0.94 \pm 0.01$ V and $FF = 0.60 \pm 0.01$. The EQE and J-V characteristics of this iBuBTDC:C_{70} cell are plotted as dashed lines in Figs. 4.20. All three devices exhibit nearly wavelength-independent EQE across the visible spectrum due to the balanced absorption of the optimized 1:3 D:A active region blends.

4.3.4 Grazing incidence X-ray analysis

To further understand the effects of side chains on morphology and device performance especially the FF, grazing incidence x-ray diffraction (GIXD)[104] was performed on vacuum-deposited films grown on Si substrates pre-coated with a 10 nm thick layer of MoO_3. Shown in Fig. 4.21 are the diffraction patterns and the corre-
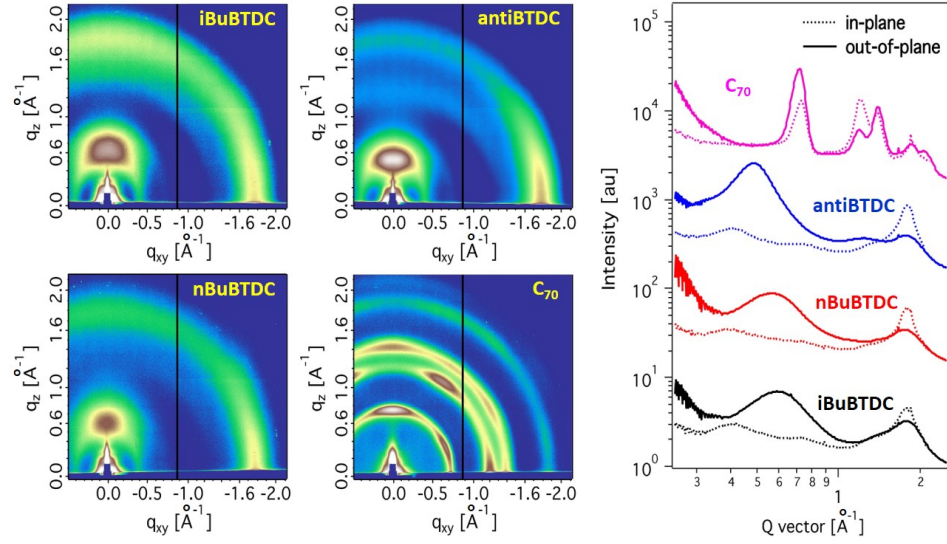
Figure 4.21: Two-dimensional grazing incidence X-ray diffraction (GIXD) scattering patterns of vacuum deposited donor and acceptor thin films and the corresponding line cut profiles.

sponding line-cut profiles of the neat donor and acceptor samples. The iBuBTDC film shows a (100) diffraction peak in the out-of-plane (q_z) direction at 0.61 $\mathring{A}^{-1}$, with a crystal coherence length of $CCL_z = 2.5$ nm. The π-π stacking is seen in both in-plane (q_{xy}) and q_z directions with a full azimuthal angular spreading at 1.79 $\mathring{A}^{-1}$, corresponding to a distance of 0.35 nm, and $CCL_{xy} = 2.1$ nm. The nBuBTDC molecule shows a similar morphology with the (100) diffraction peak at $q_z = 0.58$ $\mathring{A}^{-1}$ ($CCL_z = 2.8$ nm) and π-π stacking at 1.78 $\mathring{A}^{-1}$ ($CCL_{xy} = 2.7$ nm). The antiBTDC exhibits longer range order with a (100) peak at $q_z = 0.49$ $\mathring{A}^{-1}$ ($CCL_z = 4.0$ nm); and a π-π peak at $q_{xy} = 1.79$ $\mathring{A}^{-1}$ ($CCL_{xy} = 2.7$ nm). The C_{70} acceptor thin film also shows molecular packing with the (100) diffraction at $q_z = 0.72$ $\mathring{A}^{-1}$, with $CCL_z = 8.5$ nm, and the (010) and (001) diffraction peaks at 1.21 $\mathring{A}^{-1}$ and 1.39 $\mathring{A}^{-1}$ respectively. A weak diffraction ring is seen at 1.86 $\mathring{A}^{-1}$, corresponding to a distance of 0.34 nm characteristic of the C_{70} intermolecular spacing. The GIXD patterns of d-a-a':C_{70} blend films were also measured. However, the diffraction patterns are dominated by the C_{70} component due to its much stronger crystallinity than the d-a-a' donors in

vacuum-deposited films, preventing differentiation between the morphologies of the three blends.

The devices based on the three compounds exhibit different FFs due to differences in their in-plane and out-of-plane stacking motifs shown in Fig. 4.21. The strongest diffraction signal in the in-plane direction with almost no out-of-plane component is observed for antiBTDC, suggesting a preferred edge-on orientation. In contrast, iBuBTDC shows the most intense signal along q_z, while nBuBTDC shows diffraction intermediate between the two molecules. The higher ratio of face-on π-π stacking in the iBuBTDC film leads to efficient charge transport perpendicular to the substrate, resulting in the highest FF. As seen in Fig. 4.19d, FF and V_{OC} of the iBuBTDC:C_{70} are relatively independent of active layer thickness up to 80 nm, indicating significant long-range order. A 10% relative improvement of FF is observed for the iBuBTDC:C_{70} cell compared with nBuBTDC:C_{70}, which is likely due to the orthogonal arrangement between the adjacent stacks of nBuBTDC molecules that impedes intermolecular charge transfer.

4.3.5 Summary

In summary, the effects of side chain length and shape of small molecule d-a-a' donors on vacuum-deposited thin film properties and OPV performance are analyzed in this section. Two new donors (iBuBTDC and nBuBTDC) modified from the previously reported antiBTDC are synthesized, featuring shorter branched and straight alkyl chains, respectively. The various side chains attached to the same d-a-a' backbone show the same π-π stacking distance of $\sim$ 3.5 Å but different crystal packing configurations, resulting in distinct absorption and charge transfer properties of the three donor molecules. The iBuBTDC with its short isobutyl chain forms a compact arrangement between adjacent π-π stacks that leads to the highest film density. Based on GIXD measurements, iBuBTDC also shows the largest out-of-plan π-π stacking

95

diffraction intensity, while antiBTDC stacks mostly in the in-plane direction. The iBuBTDC therefore achieves improved absorption and intermolecular charge transport compared with antiBTDC, leading to higher OPV J_{SC} and FF with the highest $PCE = 9.3 \pm 0.5\%$. The nBuBTDC with n-butyl side chain has a similar absorption coefficient and J_{SC} to iBuBTDC. However, the orthogonal packing arrangement between neighbor stacks hinders intermolecular charge transfer that significantly reduces the FF, giving a $PCE = 7.5 \pm 0.4\%$, similar to that of antiBTDC. These results suggest that the side chains of d-a-a' small molecule donors play an important role in crystal packing that provides an opportunity to fine tune morphology to achieve a significantly improved device performance.

CHAPTER V

All-Vapor-Deposited Multi-Junction OPVs

In Chapters III and IV, we studied several vacuum-deposited d-a-a' molecules with different donor unit configurations, achieving OPV power conversion efficiencies of 9-10%. However, there are two limitations for single junction cells as indicated by Fig. 5.1. First, the photons with energy larger than the HOMO-LUMO gap results in large thermalization energy loss. Also, unlike inorganic materials with continuous absorption of photons with energy above the band gap (Si is shown as a typical example), organic materials usually exhibit a narrow range of absorption peaks with discrete exciton states. Multijunction structures are designed to compensate such losses and improve the power conversion efficiency beyond that of thermodynamically-limited single junction cells.
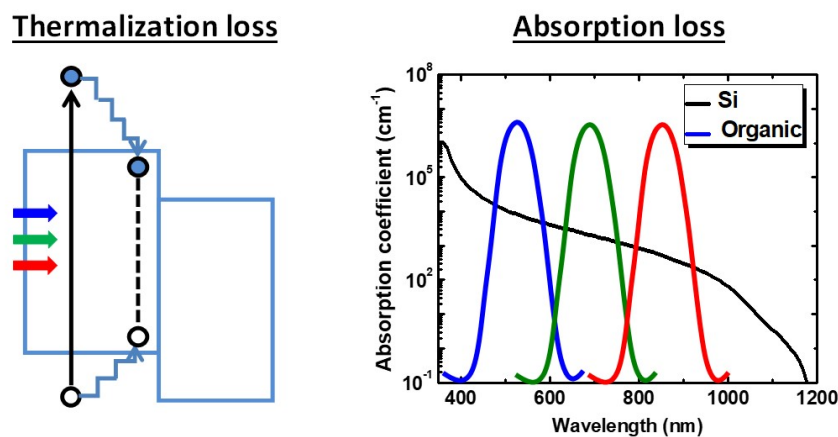
Figure 5.1: Thermalization and absorption losses in single junction OPV cells.

Here we designed and demonstrated all vacuum-deposited multijunction OPV structures with two to four subcells, achieving efficiencies $> 10\%$. The design principles of the tandem and multijunction cells will be discussed first, followed by the experimental results. The devices in this chapter are grown on unpatterned ITO with the area defined by 1 mm diameter circular metal cathode (0.785 mm^2).

5.1 Multijunction design principles

The multijunction designs in this and the next chapter are based on series connections of the subcells, requiring a balanced current density (see Fig. 1.16). The charge recombination zones (CRZ) consisting of several interconnecting layers are between the subcells that act to recombine the electron from one subcell with the hole from the adjacent cell to balance the total current flow in the tandem or multijunction stacks. There are three multijunction design principles generally used to achieve high efficiency:

1. **Subcells with minimal absorption overlap.**
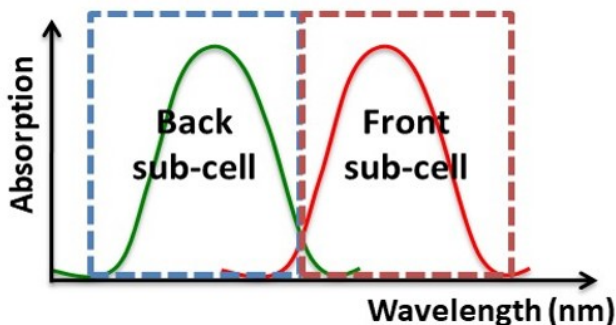
Figure 5.2: Tandem design principle - 1: subcells with minimal absorption overlap.

In order to cover a broader range of the solar spectrum with highest possible current density, ideally different subcells should have very small absorption overlap as indicated by Fig. 5.2. The combination of the green- and NIR-absorbing subcells in this chapter have complementary absorptions, and the NIR-absorbing cell is placed

98

as the front cell adjacent to the ITO complying the optical field distribution. In some cases, the NIR-absorbing cell also has strong absorption in the visible region that generates much higher current density than the green-absorbing cell. It is then placed as the back cell to allow the visible light going through the front green-absorbing cell first for sufficient absorption, which is the structure to be discussed in Chapter VI.

2. Lossless charge recombination zone (CRZ).
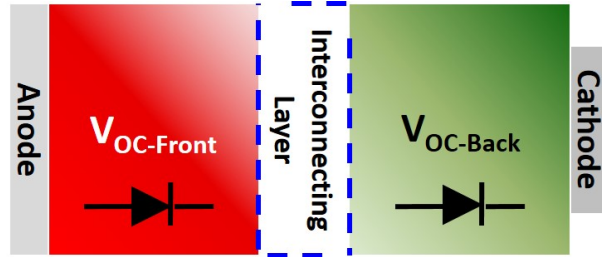
Figure 5.3: Tandem design principle - 2: the CRZ should have no optical or electrical losses.

The CRZ (as seen in Fig. 5.3) serves is a critical component in multijunction structures. It usually consists of an electron-transporting and a hole-transporting interconnecting buffer. It requires very high conductivity for sufficient recombination at the interface to avoid charge accumulation that reduces the V_{OC} and FF of the multijunction cell. Usually, an ultra thin layer of metal nanoparticles (NPs), like Ag NP is deposited in between the two buffer layers to act as the recombination center.[45] In an ideal case, the V_{OC} of the multijunction cell should be equal to the subcells connected in series:

$$V_{OC,Multijunction} = \sum_{1}^{n} V_{OC,Subcell-n} \tag{5.1}$$

The CRZ should also be optically lossless, so that it leaves more light to be absorbed by the active layers. A transparent CRZ with efficient recombination is essential for any high efficiency multijunciton OPV cells.

3. Make use of different orders of optical interference maxima.
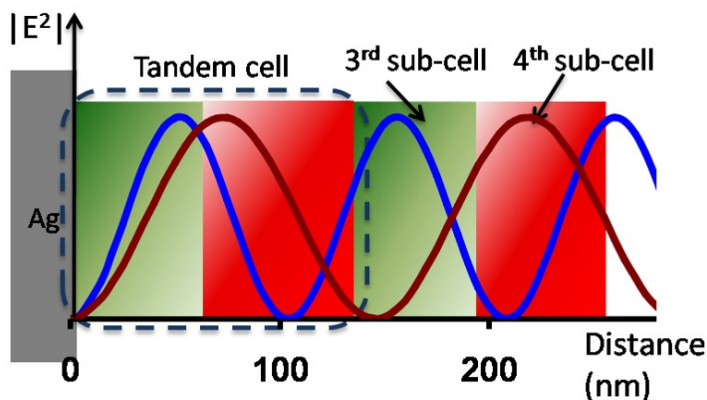
Figure 5.4: Tandem design principle - 3: multijunction structure with subcells placed at different optical interference maxima.

The OPV subcells with M-HJ structures usually have a thickness limit due to the decrease of charge collection efficiency and *FF*. A tandem structure with one green-absorbing and one NIR-absorbing subcell may exhibit a relatively large absorption loss. Third and 4th subcells, therefore, can be inserted to further improve the multijunction absorption and efficiency. As illustrated by Fig. 5.4, taking the metal contact as the static point, light with different wavelengths will show intensity peaks at different positions. The peaks extend further from the metal as the wavelength increases, while the tandem cell is placed at the first order of the optical interference maximum. To harvest light more efficiently, the 3rd and 4th sub-cells are placed at the second interference maximum. The thickness and absorption of each sub-cell is adjusted to match the current density between the subcells.

5.2 Tandem structure and performance

5.2.1 Structure and subcells

The tandem cell with the structure shown in Fig. 5.5 is fully grown by VTE. The front subcell adjacent to the transparent anode comprises the primarily orange-to-

NIR absorbing donor, DTDCTB blended with C_{60}. It is paired with a green-absorbing DBP:C_{70} back subcell. As discussed in Section 3.2, the C_{60} intermolecular charge transfer (CT) absorption in the green is greatly reduced when diluted in DTDCTB. At 1:1 blend ratio, the CT absorption by C_{60} is suppressed to only 40% of its value in the neat film (Fig. 3.1), thus providing a spectrally complementary system with the green-absorbing sub-cell. The extinction coefficient of the 1:1 DTDCTB:C_{60} and the 1:10 DBP:C_{70} blends along with the AM 1.5G solar spectrum, are shown in Fig. 5.5 on the right. The DBP:C_{70} film exhibits a broad spectral response at $\lambda < 700$ nm, while the DTDCTB:C_{60} layer primarily absorbs from $\lambda = 500$ nm to 900 nm. By stacking these two sub-cells, absorption spans the wavelengths from $\lambda = 350$ nm to 900 nm, thereby covering a large portion of solar spectrum with only minimal overlap between the constituent devices. The tandem thus harvests light efficiently with good current match between the sub-cells.
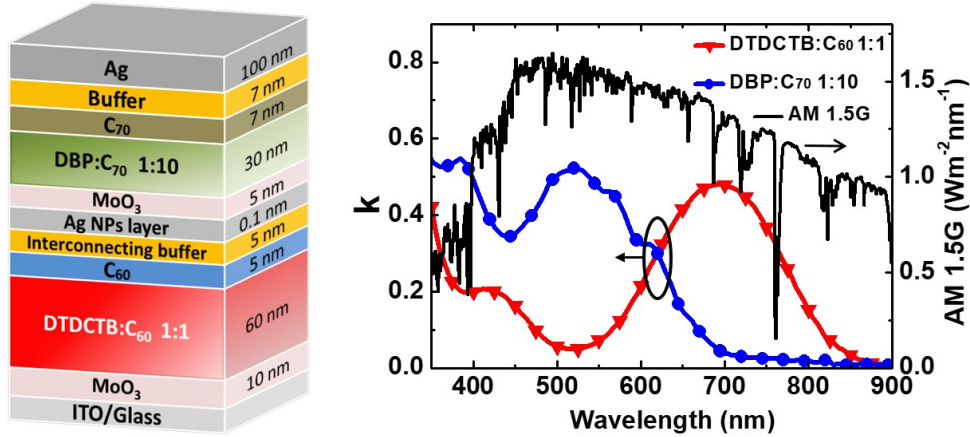
Figure 5.5: Tandem cell with DTDCTB:C_{60} and DBP:C_{70} subcells: structure and subcell extinction coefficients.

An optimized DTDCTB:C_{60} (1:1) single junction photovoltaic cell with 60 nm M-HJ and 20 nm neat C_{60} ratio achieves $J_{SC} = 11.6 \pm 0.2$ mA/cm^2, $V_{OC} = 0.82 \pm 0.01$ V, $FF = 0.55 \pm 0.01$ and $PCE = 5.3 \pm 0.1\%$ at 1 sun, AM 1.5G illumination. In the tandem structure, the thickness of the neat C_{60} layer was reduced from 20 nm

to 5 nm to move the front cell closer to the cathode and increase the absorption by the DTDCTB:C_{60} active layer, and to reduce the CT absorption of the C_{60} layer. The optimized structure of the back subcell is: ITO/MoO$_3$ (5 nm)/DBP:C_{70} (30 nm, 1:10 ratio by vol.)/C_{70} (7 nm)/BPhen (7 nm)/Ag (100 nm), resulting in $J_{SC} = 11.3 \pm 0.2$ mA/cm^2, $V_{OC} = 0.90 \pm 0.01$ V, $FF = 0.61 \pm 0.01$ and $PCE = 6.2 \pm 0.1\%$. The DBP:C_{70} layer is as thin as 30 nm to balance the current of the DTDCTB:C_{60} front cell.

5.2.2 Charge recombination zone

The CRZ between the front and back subcells employs a three-layer structure: electron conducting buffer/Ag NP (1Å)/MoO$_3$. The Ag NPs pin the Fermi levels of the other two layers, providing charge recombination and plasmonic field enhancement.[45] The 3,4,9,10-perylenetetracarboxylic-bisbenzimidazole (PTCBI) had been widely used as the buffer.[105–107] In spite of its high conductivity, interconnecting layers with a PTCBI blocker have a significant absorption loss in the visible and a rather low exciton blocking efficiency. Hence, for cell interconnection we employed a previously reported transparent exciton blocking and electron conducting BPhen:C_{60} electron filter[84], which has been introduced in Section 3.2.2.
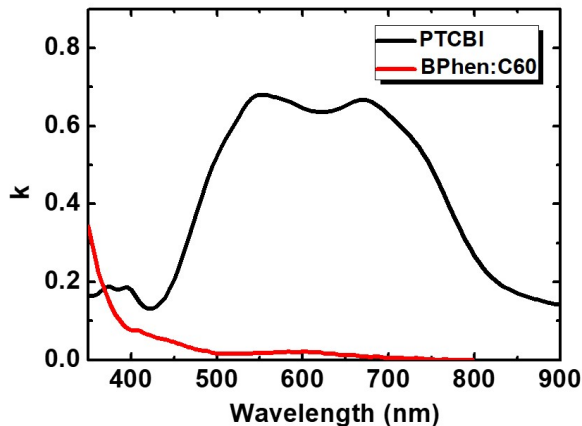
Figure 5.6: Extinction coefficients of PTCBI and BPhen:C_{60}.
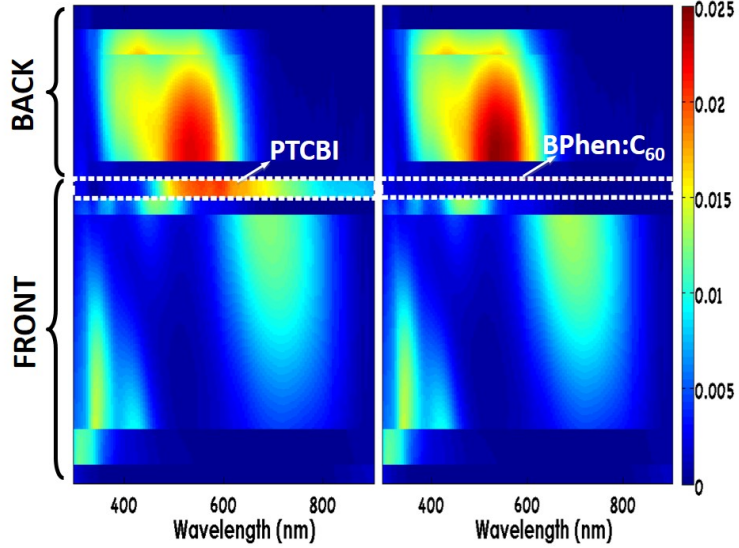
Figure 5.7: Simulated optical field distribution in the tandem cell with PTCBI or BPhen:C_{60} as interconnecting buffer layer.

Fig. 5.6 compares the extinction coefficient of BPhen:C_{60} with PTCBI. The PTCBI presents large absorption between 450 nm to 800 nm with k as large as 0.7. In contract, BPhen:C_{60} only exhibits a very small absorption below 500 nm and $k \approx 0$ above 500 nm. Figure 5.7 shows the simulated absorbed power distribution within the tandem cell, comparing a 5 nm thick PTCBI with a similarly thick BPhen:C_{60} mixed buffer. As the dashed white rectangle indicates, the BPhen:C_{60} is transparent, in striking contrast with the PTCBI buffer. The reduced absorption of the interconnecting buffer leads to improved current density of the front cell as well as the tandem cell, which will be discussed below. The simulation also shows that both sub-cells fit within the first interference maximum of the optical field.

5.2.3 Tandem performance

Figure 5.8 shows the EQE spectrum of the tandem OPV with the structure shown in Fig. 5.5 using PTCBI interconnecting layer. The EQE of the tandem cell is calculated (solid line) based on the transfer matrix method, along with the sum of the subcell measured EQE (dashed line). The tandem EQE is higher than that

measured for both individual component subcells, and is nearly identical with the sum of these efficiencies, except for $< 10\%$ loss between 550 nm and 700 nm where the subcells show a small absorption overlap. The tandem device gives $J_{SC} = 9.2 \pm 0.2$ mA/cm^2, $V_{OC} = 1.72 \pm 0.01$ V, $FF = 0.58 \pm 0.01$, giving $PCE = 9.2 \pm 0.2\%$.
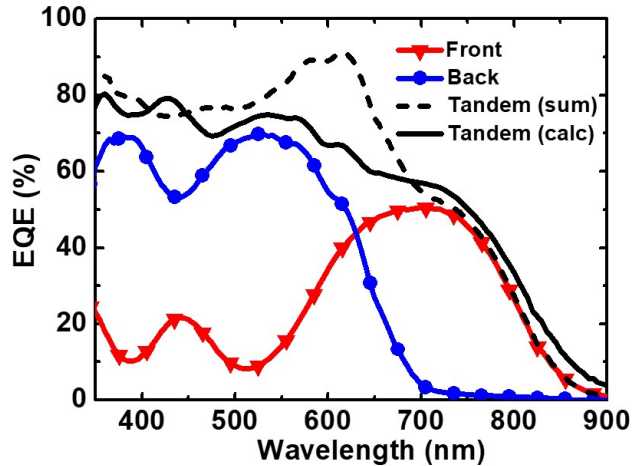
Figure 5.8: Quantum efficiencies of the tandem cell with PTCBI. *EQE* of the measured front-only cell, back-only cell, the sum of the two, and the calculated *EQE* of the tandem cell structure with PTCBI as the interconnecting buffer layer.

The fourth quadrant *J-V* characteristics of tandems utilizing the two interconnecting layers, PTCBI and BPhen:C$_{60}$, are shown in Fig. 5.9. Here, the front cell is fabricated approximating the DTDCTB:C$_{60}$ sub-cell in the tandem stack by inserting a 0.1 nm thick Ag nanoparticle layer followed by a 40nm thick MoO$_3$ spacer located beneath the Ag contact. As expected, when PTCBI is replaced with BPhen:C$_{60}$, J_{SC} increases from 9.9 ± 0.2 mA/cm^2 to 10.4 ± 0.2 mA/cm^2 in the front sub-cell, with no significant change in *FF*. Hence, the efficiency of the front sub-cell increases from $4.8 \pm 0.1\%$ to $5.1 \pm 0.1\%$. Also from Fig. 5.7, the optical field in the DBP:C$_{70}$ sub-cell is enhanced when using BPhen:C$_{60}$, leading to a corresponding increase in current. Consequently, J_{SC} of the tandem cell is increased to 9.9 ± 0.2 mA/cm^2. The results of the cell using BPhen:C$_{60}$ whose structure and optimized layers thicknesses are shown in Fig. 5.5, are summarized in Table 5.1.
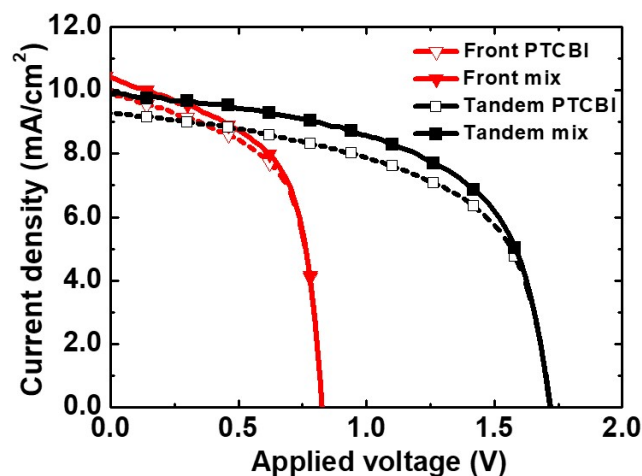
Figure 5.9: *J-V* characteristics of the front-only and the tandem cell with PTCBI or BPhen:C_{60} as interconnecting buffer layer.
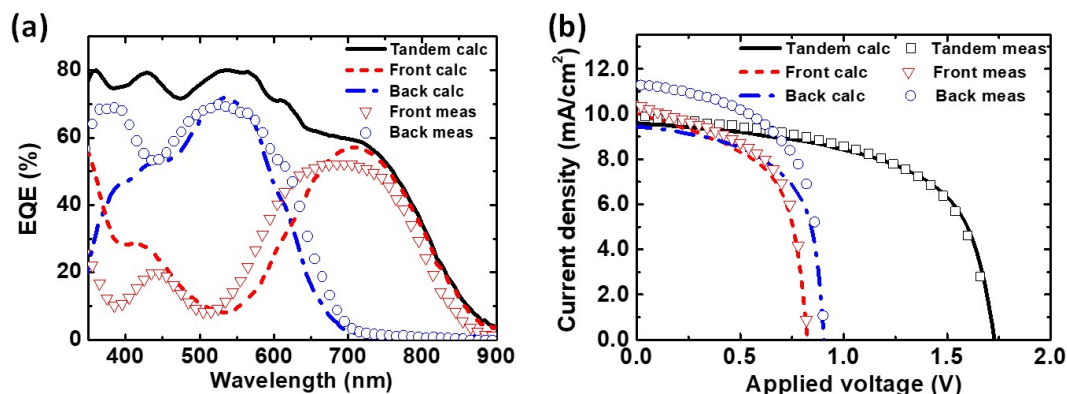
Figure 5.10: Tandem performance with BPhen:C_{60}. Measured and simulated a) *EQE*; and b) *J-V* characteristics of the optimized tandem cell using BPhen:C_{60} as the interconnecting buffer layer.

The optimized tandem cell *EQE* shown in Fig. 5.10a is similar to that employing a conventional PTCBI buffer, while the measured front subcell peak *EQE* increased. Figure 5.10b shows measured and calculated 4th quadrant *J-V* characteristics. The calculated tandem *J-V* agree with the measurement, suggesting that the models are predictive of performance, thereby simplifying device layer thickness design. The optimized tandem OPV cell achieves a measured $J_{SC} = 9.9 \pm 0.2$ mA/cm2, $V_{OC} = 1.72 \pm 0.01$ V, $FF = 0.59 \pm 0.01$, with $PCE = 10.0 \pm 0.2\%$. This represents a $> 60\%$

improvement over the discrete cell efficiencies comprising the stack. Furthermore, the tandem V_{OC} is equal to the sum of the constituent sub-cells, suggesting that the interconnecting charge recombination layer is lossless. However, as discussed in Section 3.4, this tandem structure shows edge effect that leads to an overestimation of J-V measurement, especially for small area cells. The corrected values of J_{SC} and PCE are 8.9 mA/cm^2 and 9.0%, respectively.

Table 5.1: Measured (meas) and calculated (calc) tandem and subcells performance.

Cells	J_{SC} (mA/cm^2)	V_{OC} (V)	FF	PCE (%)
Front (meas)	10.4 $\pm$ 0.2	0.82 $\pm$ 0.01	0.59 $\pm$ 0.01	5.1 $\pm$ 0.1
Front (calc)	10.0	0.82	0.57	4.7
Back (meas)	11.3 $\pm$ 0.2	0.90 $\pm$ 0.01	0.61 $\pm$ 0.01	6.2 $\pm$ 0.1
Back (calc)	9.4	0.90	0.61	5.2
Tandem (meas)*	9.9 $\pm$ 0.2	1.72 $\pm$ 0.01	0.59 $\pm$ 0.01	10.0 $\pm$ 0.2
Tandem (calc)	9.6	1.72	0.60	9.9

* Correction due to edge effect: $J_{SC} \approx 8.9$ mA/cm^2, $PCE \approx 9.0\%$.

5.2.4 Further discussion

Lassiter *et al.* showed that an optimized multijunction structure employs subcells whose currents are approximately matched at the maximum power point (MPP) of operation.[108] They defined $\Delta\eta$ as the power conversion efficiency penalty that is related to the mismatch in constituent sub-cell current densities at their MPPs. That is, the optimal design corresponds to $\Delta\eta \to 0$, where:

$$\Delta\eta = 1 - \frac{J_{MM}V_{MM}}{J_{M1}V_{M1} + J_{M2}V_{M2} + \cdots + J_{Mn}V_{Mn}} \tag{5.2}$$

Here, J_M and V_M are the simulated current density and voltage at the MPP. The subscript M refers to the multijunction cell, and 1, 2, $\cdots$, n refer to each of its sub-
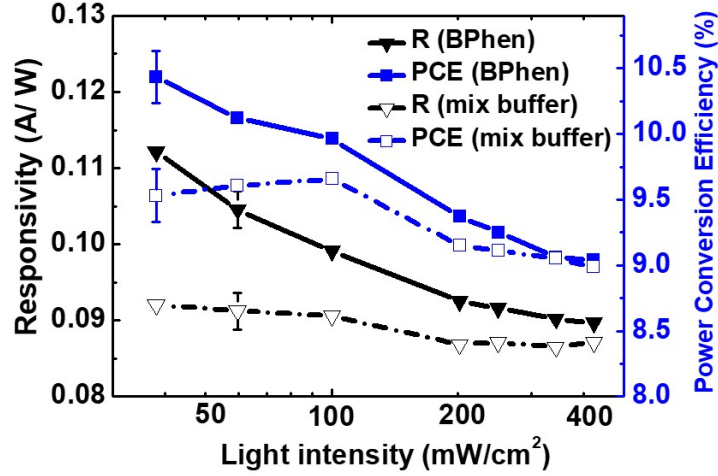
Figure 5.11: Efficiency *vs.* light intensity. Responsivity (R) and *PCE* of the tandem solar cell with BPhen (7 nm) or BPhen:C_{60} (1:1, 5 nm)/BPhen (2 nm) as the cathode buffer layer as a function of light intensity up to 4 suns, AM 1.5G illumination.

cells. According to the simulated *J-V* characteristics of the sub-cells in Fig. 5.10b, the optimized tandem cell has $\Delta\eta = 0.28\%$. This is very close to the ideal case for a tandem where $J_{MT} = J_{M1} = J_{M2}$, and $V_{MT} = V_{M1} + V_{M2}$.

In one tandem cell structure, the BPhen cathode buffer (7 nm, below the Ag contact) was placed with the previously described high electron conductivity, exciton blocking BPhen:C_{60} (5 nm)/BPhen (2 nm) compound electron filter that reduces bimolecular recombination at the buffer/acceptor interface. The electron filter increases the efficiency of the back cell, but also increases the *FF* and J_{SC} differences between the subcells, which ultimately causes a larger mismatch. The current mismatch results in $\Delta\eta = 4.8\%$, leading to a slight reduction in $J_{SC} = 9.0 \pm 0.2$ mA/cm² and $PCE = 9.6 \pm 0.2\%$ from the tandem in Fig. 5.10. However, the reduced tendency for bimolecular recombination and exciton-polaron quenching suggests that the use of this compound buffer can result in improved response at high intensity.[109] The responsivity and *PCE* are measured from 0.2 sun up to 4 suns intensity of the tandem cells, with BPhen or BPhen:C_{60}/BPhen as the cathode buffer layers (see Fig. 5.11).

The responsivity of the tandem cell with BPhen decreases from 0.112 ± 0.002 A/W to 0.090 ± 0.002 A/W, while the tandem with the mixed buffer shows only a minor (5%) change from 0.092 ± 0.002 A/W to 0.087 ± 0.002 A/W. The tandem cell with the mixed cathode buffer shows no efficiency change up to 1 sun intensity, after which it decreases due to series resistance. At 4 suns, both cells exhibit a power conversion efficiency of 9.0%.

5.3 Triple- and quadruple-junctions
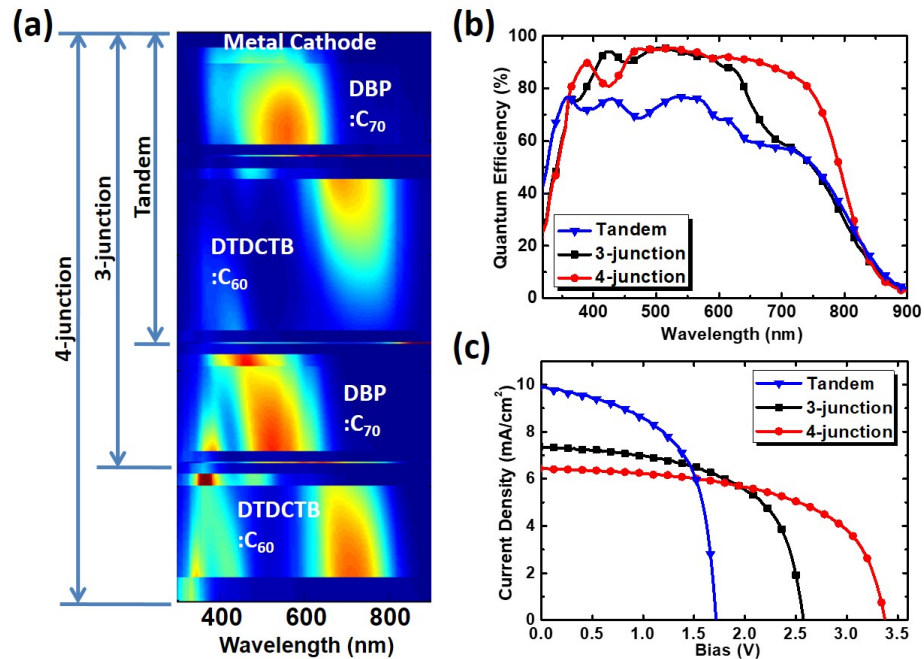
Figure 5.12: Triple- and quadruple-junction structure and performance: a) Device structure; b) Quantum efficiency and c) J-V characteristics, compared with the tandem cell.

From the simulated tandem cell quantum efficiency shown by Fig. 5.10a, the maximum value is 80% below $\lambda = 600$ nm and falls below 50% at 800 nm. Therefore there is still a considerable absorption loss both in the green and NIR region. To take further advantage of the optical field distribution and achieve even higher V_{OC}, as introduced in the design principle section, an additional DBP:C_{70} (1:10) subcell

and another DTDCPB:C_{60} (1:1) subcell is inserted at the front of the tandem stack at the second optical interference maximum as the triple- and quadruple- junction structures, as indicated by Fig. 5.12a.

In the triple-junction cell, the middle DTDCTB:C_{60} (1:1) cell is sandwiched between two DBP:C_{70} sub-cells. The BPhen:C_{60} interconnecting layers are used between the sub-cells to ensure minimal absorption loss. Compared with the tandem cell, the thicknesses of the back DBP:C_{70} and the middle DTDCTB:C_{60} cells are increased over that used in the tandem such that the front, short-wavelength absorbing DBP:C_{70} sub-cell fits into the second order optical interference maximum. The front and back green-absorbing cells absorb at different optical maxima to efficiently harvest short wavelength photons while, cooperating with the middle NIR-absorbing cell. Similar to the tandem cell, the thicknesses of each active layer is optimized by simulation to achieve current balance between sub-cells at 1 sun intensity.

Table 5.2: Device performance of the triple- and quadruple-junction cells.

Cells	J_{SC} (mA/cm^2)	V_{OC} (V)	FF	PCE (%)	$PCE_{corrected}$ * (%)
3-junction	7.3 ± 0.2	2.58 ± 0.01	0.59 ± 0.01	11.1 ± 0.2	/
4-junction	6.4 ± 0.02	3.38 ± 0.01	0.58 ± 0.01	12.6 ± 0.3	10.3

* Corrected efficiency due to edge effect. Triple junction was not measured.

As summarized in Table 5.2, compared with the tandem, the V_{OC} of the triple junction cell increases to 2.58 ± 0.01 V. Although J_{SC} decreases to 7.3 ± 0.2 mA/cm^2, it achieved $PCE = 11.1 \pm 0.2\%$. Figure 5.12b shows that the calculated quantum efficiency at wavelengths from 400 nm to 700 nm approaches 100% in the triple-junction cell due to contributions from the two DBP:C_{70} sub-cells at the different interference maxima. Note that its V_{OC} is 0.04 V lower than the sum of its sub-cells, mainly due to the reduced optical intensity in each active layer. By further adding a front DTDCTB:C_{60} subcell, the quantum efficiency at the NIR region increases

close to 100%, improving PCE to above 12% with V_{OC} of 3.38 V. Both the triple and quadruple-junction efficiencies need to be corrected due to the edge effect (see Section 3.4). The quadruple-junction gives $PCE = 10.3\%$ when fabricated with larger device area and measured with a shadow mask to eliminate the edge effect.

Through this work we demonstrate that the multijunction OPV consisting of sub-cells with complementary, or non-overlapping spectra, and whose sub-cells are positioned to absorb different optical interference orders, can achieve efficiency > 10%. The V_{OC} of the NIR-absorbing DTDCTB:C$_{60}$ cell is as high as 0.82 V with absorption up to 900 nm. The tandem $V_{OC} = 1.72$ V is also among the top of the published structures. On the other hand, both J_{SC} and FF has large room for further improvement, showing potential for future increases in efficiency.

5.4   Tandem EQE and J-V angle-dependence measurements
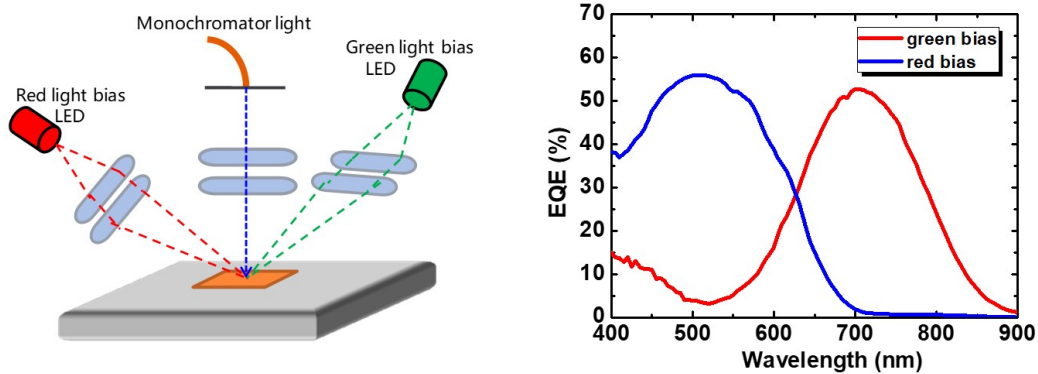
Figure 5.13: Tandem cell subcell EQE measurement: set up (left) and the measured result (right).

The subcells in a tandem structure have different photoresponsive regions with small overlap. Therefore the EQE of the subcells and the tandem cannot be measured by the same set up used for single junction. For the incident monochromatic light at each wavelength, usually only one of the subcells can be turned on. The other

subcell with very small or no response at the incident wavelength will put the tandem cell close to the open-circuit condition. In order to get an accurate measurement, one of the subcells in the tandem needs to be saturated with a DC light bias while measuring the other subcell.[110,111] Figure 5.13 left shows the sketch of the set up. A red LED emitting at 735 nm wavelength is used to bias and saturate the NIR-absorbing DTDCTB:C_{60} subcell while measuring the DBP:C_{70} cell. Similarly, a 505 nm green LED is used to bias the DBP:C_{70} subcell. On the right are the measured subcell EQEs. The measured J_{SC} of the specific tandem cell is 7.6 mA/cm^2, while the EQE integrated current density of the green-absorbing and NIR-absorbing subcells are 7.5 mA/cm^2 and 7.3 mA/cm^2 respectively. It shows the DTDCTB:C_{60} is the current-limiting subcell in the stack. On the other hand, the measured subcell current is slightly lower than the tandem, indicating the subcells may not be fully saturated with the light biases. Nevertheless, the setup exhibits good accuracy for the tandem structure containing subcells with minimal absorption overlap.
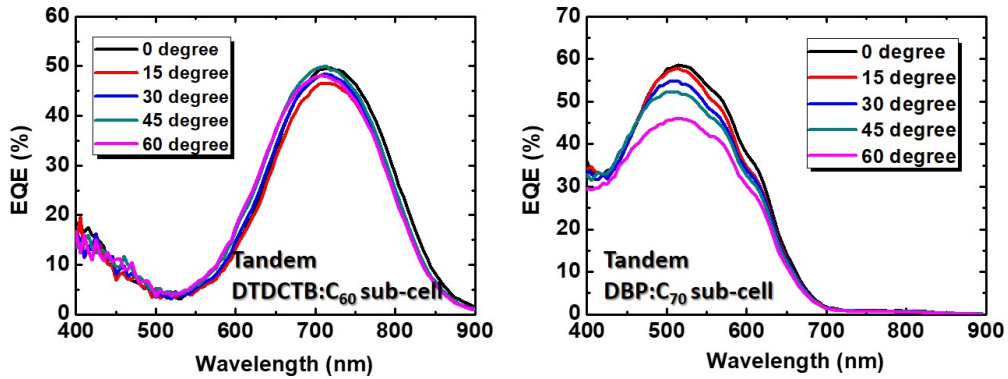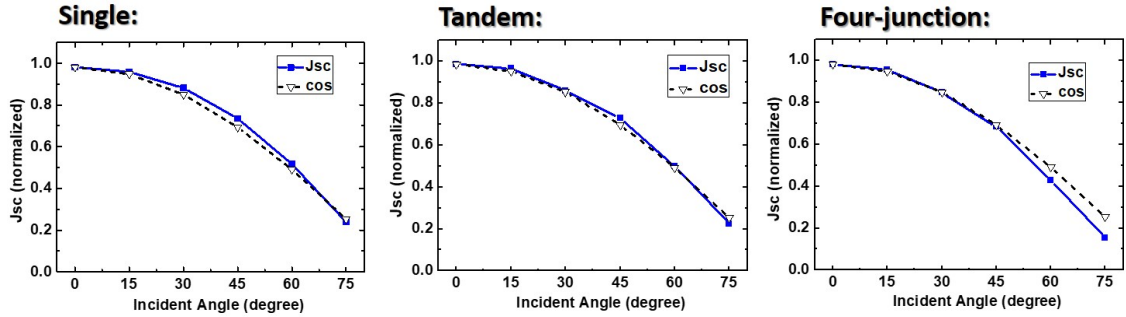

Figure 5.14: Tandem subcell angle-dependent EQE.

The incident light angle (relative to the normal incidence) in Fig. 5.13 is then adjusted from 0° to 60° relative to normal to measure the angle-dependent EQE. Seen from Fig. 5.14, as the angle increases, the EQE of the front DTDCTB:C_{60} cell does not change while the back DBP:C_{70} cell EQE decreases significantly at $\lambda = 500$ nm. The longer light path through the front cell at large incident angle therefore reduces

111

Figure 5.15: Single and multijunction cell angle-dependent J_{SC} characteristics.

the back cell absorption. However since the back cell is not the current-limiting cell, the effect on tandem current balance is smaller than the back cell itself.

Figure 5.15 exhibits the measured J_{SC} of the single junction (DBP:C$_{70}$), tandem and quadruple-junction cells as functions of incident light angle under 1 sun AM 1.5G illumination. The tandem and quadruple-junction OPVs have the same structures as discussed earlier. As the angle (θ) increases, the power density decrease with $\cos(\theta)$, which is indicated by the dashed lines. All of the single, tandem and quadruple-junction curves roughly follow the cosine function. The drop becomes steeper as the number of subcells increases due to unbalanced current density, although the effect is not dramatic except for the quadruple-junction above 45° angle. This result is helpful to understand the multijunction cell performance in a terrestrial application. The multijunction designs, especially the tandem cell, therefore show promise for outdoor applications with relatively small performance loss caused by the solar angle.

CHAPTER VI

High Fabrication Yield Tandem OPV Combining Vacuum-deposited and Solution-Processed Non-Fullerene Acceptor-Based Subcells

The all vacuum-deposited multijunction structure in Chapter V is able to achieve efficiency of 10-12%. However, the performance is still limited by the NIR-absorbing DTDCTB:C_{60} cell, whose EQE peak value is lower than 60% and the FF is lower than 0.6. As a result, the green-absorbing DBP:C_{70} cell needs to be made very thin (30 nm) without the mixed buffer to balance the current and FF. To achieve very high efficiencies, a NIR-absorbing solar cell with better performance is required. Solution-processed non-fullerene acceptors (NFAs) with energy gaps < 1.4 eV have been recently reported with PCEs > 10%[35,60], appearing to be promising as NIR-absorbing subcells for high efficiency multijunction OPVs. The green-absorbing sub-cell is vacuum-deposited for good uniformity, purity and controllability. The DBP:C_{70} cell is replaced by DTDCPB:C_{70} introduced in Chapter III, the highest efficiency VTE cell to date. The tandem structure requires deposition of the solution-processed NFA-based cell onto the surface of a previously vacuum-deposited fullerene-based cell. A nearly optically and electrically lossless charge recombination zone (CRZ) between the sub-cells is employed that efficiently caps and protects the underlying vacuum-

deposited layers, resulting in $\sim 100\%$ fabrication yield for 2 mm^2 and 9 mm^2 devices and a milestone tandem efficiency of 15% under 1 sun, AM 1.5G spectral illumination.

6.1 NIR-absorbing NFAs

The fullerene acceptors, C$_{60}$ and C$_{70}$ for vacuum deposition, and PC$_{60}$BM and PC_{70}BM for solution-processing, have long been used in OPV cells. They provide good electron conductivity and transport when mixed with donors. On the other hand, the HOMO and LUMO levels of the fullerene acceptors are fixed at -6.2 eV and -4.0 eV with the absorption edge $\sim$ 700 nm. Their extinction coefficients are also relatively low (C$_{60}$ and C$_{70}$ as an example shown in Fig 3.1). For NFAs, by adjusting the HOMO energy, the absorption edge can be red-shifted to beyond 900 nm while maintaining relatively high V_{OC} and FF, making them promising NIR OPV candidates by pairing with a variety of donors.
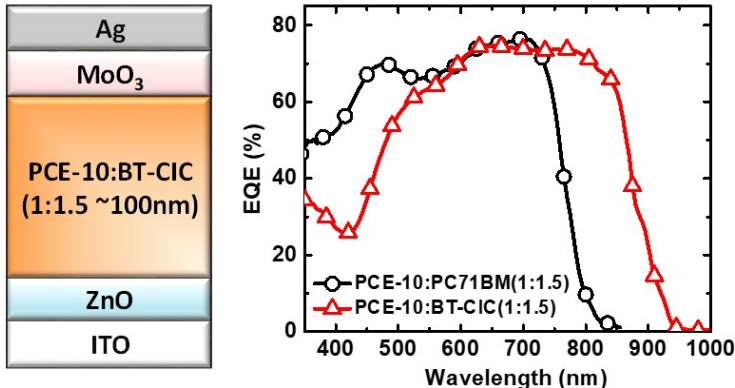
Figure 6.1: Inverted PCE-10:BT-CLC device structure (left) and EQE (right), compared with PCE-10:PC$_{70}$BM fullerene acceptor-based cell.

Figure 6.1, left, shows the NIR-absorbing NFA-based cell comprising a mixture of NFA BT-CIC and the donor polymer PCE-10.[35] The device is in inverted structure that electrons are conducted through ZnO and being collected by the ITO, while holes are transported by MoO$_3$ and collected at the Ag cathode. The NFA BT-CIC has

**Table 6.1:** Devcei performances of PCE-10:PC$_{71}$BM and PCE-10:BT-CIC cells.

Device	J_{SC} (mA/cm^2)	V_{OC} (V)	FF	PCE (%)	AVT* (%)
PCE-10:PC$_{71}$BM	17.9	0.80	0.69	9.6	/
PCE-10:BT-CIC	22.5	0.70	0.71	11.2	/
PCE-10:BT-CIC (Semitransparent)	15.8	0.68	0.66	7.1	43

* Average transmittance.

an a-d-a configuration whose planar backbone and electron-withdrawing Cl atoms reduces the energy gap.[112] It exhibits a LUMO energy of -4.1 eV, which is similar to that of the fullerene acceptor [6,6]-phenyl-C71-butyric acid methyl ester (PC$_{71}$BM), but a shallower HOMO energy of -5.5 eV (compared to -6.0 eV for PC$_{71}$BM). On the right is shown the EQE, as compared with the PCE-10:PC$_{71}$BM cell. Both cells show EQE peak values $\sim$ 75%, while the PCE-10:BT-CIC cell exhibits almost 100 nm red-shifted photoresponse to 950 nm. The performance of these two cells with 100 nm Ag cathode is summarized in Table 6.1. Due to the red-shifted absorption of the NFA acceptor, the PCE-10:BT-CIC cell achieves J_{SC} = 22.5 mA/cm^2, compared with 17.9 mA/cm^2 of the PCE-10:PC$_{71}$BM cell. The FF also improves from 0.69 to 0.71 while the V_{OC} drops from 0.80 V to 0.70 V. The PCE = 11.2% is achieved by the PCE-10:BT-CIC cell, much higher than the VTE-processed DTDCTB:C$_{60}$ NIR-absorbing cell introduced in Chapter III with similar absorption range.

The PCE-10:BT-CIC cell shows the highest EQE from 600 nm to 900 nm while leaving a transparent window below 600 nm, with EQE dropping to $<$ 30% at 450 nm. Figure 6.2 shows the device transmittance with different Ag thicknesses from 10 nm to 20 nm. The cell with 10 nm Ag shows an average transmittance of 43% in the visible, achieving PCE = 7.1% as listed in Table 6.1. The device is light blue as seen from the photo in Fig. 6.2, left. The NFA-based NIR-absorbing cell, therefore, is an

important candidate for multijunction and semitransparent OPV applications.
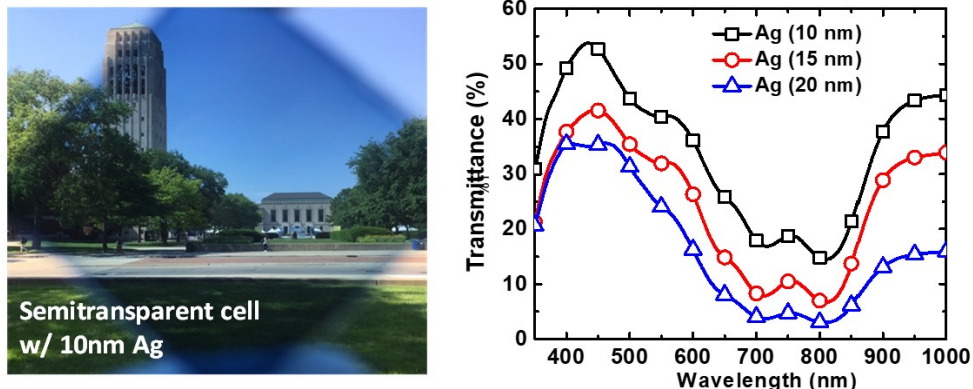
Figure 6.2: Non-fullerene acceptor (NFA)-based semitransparent cell. (Left) The photo of semitransparent PCE-10:BT-CIC cell with 10 nm Ag; (Right) Device transparency with different Ag cathode thicknesses.

6.2 Tandem structure and performance

6.2.1 Subcells
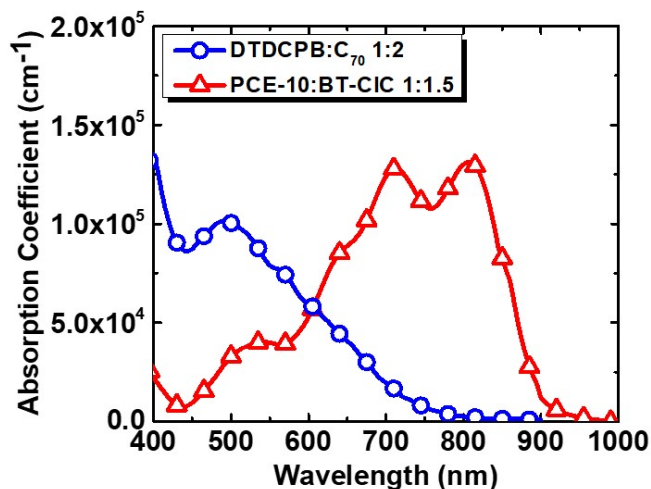
Figure 6.3: Absorption coefficients of 1:2 DTDCPB:C_{70} and 1:1.5 PCE-10:BT-CIC blends.

The front cell (near the transparent conducting anode in the tandem structure) grown by vacuum thermal evaporation (VTE) employs the d-a-a' donor DTDCPB

116

blended with C_{70}.[54] The solution-processed NFA-based back cell (adjacent to the reflecting metal cathode) comprises the PCE-10:BT-CIC.[35] The active layer absorption coefficients is shown in Fig. 6.3. The vacuum deposited small molecule DTDCPB:C_{70} cell strongly absorbs light between wavelengths of $\lambda = 400$ nm to 700 nm. The 1:1.5 PCE-10:BT-CIC mixture shows absorption from $\lambda = 500$ nm to 950 nm, with a peak absorption coefficient of 1.3×10^5 cm^{-1} at around $\lambda = 700$ nm and 800 nm, compared with a peak of 1.0×10^5 cm^{-1} for DTDCPB:C_{70} at $\lambda = 500$ nm. The combination of these cells in a tandem structure results in broad spectral coverage of solar illumination between 400 nm and 900 nm, with each subcell in the stack generating similar currents.

The performance of the optimized single junction PCE-10:BT-CIC NFA cell used for integration into the tandem cell is summarized in Table 6.2, with the conventional structure: ITO/PEDOT:PSS (50 nm)/PCE-10:BT-CIC (1:1.5, 75 nm)/TmPyPB (5 nm)/Ag (100 nm), to be connected with the VTE subcell in series. It attains $J_{SC} = 22.1 \pm 0.4$ mA/cm^2, $V_{OC} = 0.69 \pm 0.01$ V and $FF = 0.70 \pm 0.01$, resulting in $PCE = 10.7 \pm 0.2\%$ at 1 sun (100 mW/cm^2), AM 1.5G simulated spectral illumination. This is comparable to that of an analogous inverted cell[35], indicating efficient electron and hole transport in the TmPyPB and PEDOT:PSS buffer layers. The device shows an average external quantum efficiency, $EQE > 70\%$ between $\lambda = 500$ nm and 850 nm, while leaving a transparency window at $\lambda < 600$ nm that is filled by the visible-absorbing subcell in the tandem structure.

Due to a $J_{SC} > 20$ mA/cm^2 and the spectral coverage into the NIR of the PCE-10:BT-CIC single junction cell, it is optimally employed as the back cell in the tandem OPV. This creates a processing challenge since the PEDOT:PSS and PCE-10:BT-CIC need to be spin-coated from solution on top of the previously VTE-grown films comprising the front cell. Figure 6.4a, left, shows the VTE grown DTDCPB:C70 single junction structure (reference): ITO/MoO$_3$ (10 nm)/DTDCPB:C_{70} (1:2 160

nm)/BPhen:C_{60} (1:1, 8 nm)/Ag (100 nm). It requires a thicker active layer than the previously reported structure (160 nm compared to 80 nm)[54] since it lacks the reflecting metal cathode when inserted into the tandem stack in the front cell position. The donor:acceptor (D:A) ratio is optimized at 1:2 to achieve FF > 0.65. The reference cell yields $J_{SC} = 16.4 \pm 0.3$ mA/cm^2, $V_{OC} = 0.90 \pm 0.01$ V, $FF = 0.66 \pm 0.01$ and $PCE = 9.7 \pm 0.2$ % (Table 6.2).
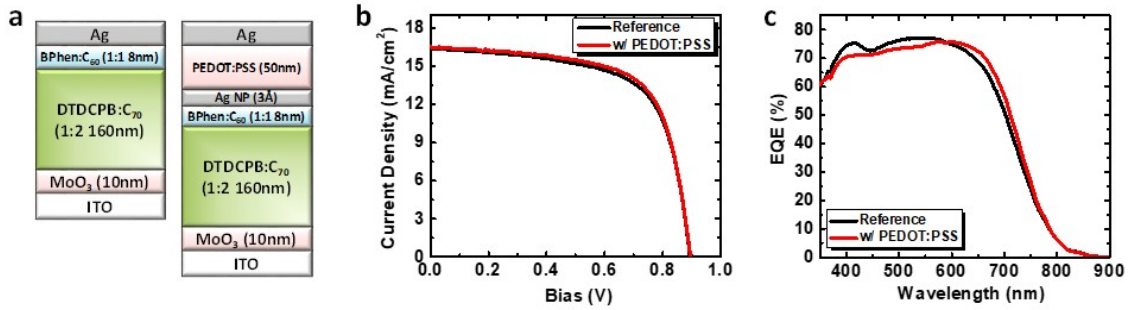
Figure 6.4: DTDCPB:C_{70} subcell with and without (reference) charge recombination zone containing PEDOT:PSS: a) Device structures; b) *J-V* characteristics; and c) *EQE*.

Table 6.2: PCE-10:BT-CIC and DTDCPB:C_{70} subcell performance.

Device	J_{SC} (mA/cm^2)	V_{OC} (V)	FF	PCE (%)
PCE-10:BT-CIC (1:1.5, 75nm)	22.1 ± 0.4	0.69 ± 0.01	0.70 ± 0.01	10.7 ± 0.2
DTDCPB:C_{70} (1:2, 160nm)	16.4 ± 0.3	0.90 ± 0.01	0.66 ± 0.01	9.7 ± 0.2
DTDCPB:C_{70} (1:2, 160nm, w/ CRZ)	16.4 ± 0.3	0.90 ± 0.01	0.67 ± 0.01	9.9 ± 0.2

6.2.2 Charge recombination zone

The CRZ comprises an ultrathin layer of Ag NPs (3 Å) sandwiched in between a VTE-deposited electron filtering buffer layerBPhen:C_{60} and a transparent, solution-

processed PEDOT:PSS layer. The hydrophilic PEDOT:PSS forms a uniform capping layer that prevents the solvents from penetrating and damaging the underlying hydrophobic VTE layers. To understand the performance of the CRZ, it is inserted immediately adjacent to the Ag cathode (Fig. 6.4a, right). As shown by the J-V characteristics in Fig. 6.4b, the device with the CRZ exhibits identical J_{SC} and V_{OC} to that of the reference cell, with a higher $FF = 0.67 \pm 0.01$ and $PCE = 9.9 \pm 0.2\%$ indicating that the recombination zone is optically and electrically lossless. According to the EQE spectra in Fig. 6.4c, the cell with 50 nm thick PEDOT:PSS spacer shows slightly higher photoresponse at long wavelengths than the reference, which is consistent with differences in the optical field distributions.
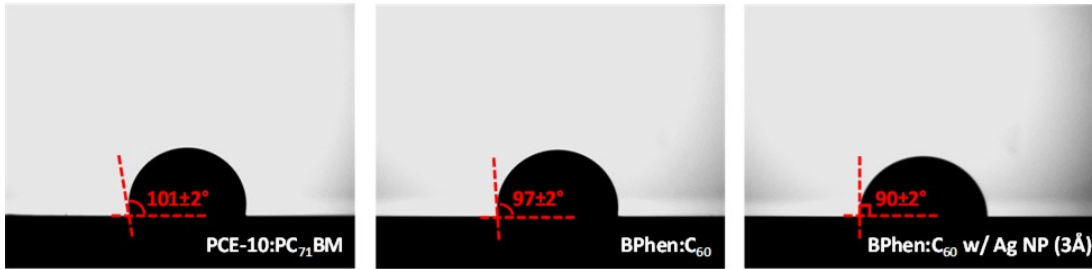
Figure 6.5: Contact angles between the PEDOT:PSS droplet on top of different organic films. The volume of the droplet is 10 μl.

The hydrophilicity of the acidic ($pH = 1$-2) PEDOT:PSS usually leads to incomplete wetting and the possibility of dissolving the underlying hydrophobic layers. In the tandem structure, the acid-resistant BPhen:C_{60} is employed as the front cell exciton blocking layer. The contact angle of the PEDOT:PSS on a BPhen:C_{60} film is 97 $\pm$ 2°, smaller than on the PCE-10:PC$_{71}$BM (101 ± 2°) active layer. The ultra-thin Ag NP layer on top of BPhen:C_{60} further decreases the contact angle to 90 ± 2°(see Fig. 6.5). This results in uniform coverage of the PEDOT:PSS on BPhen:C_{60}/Ag NP while maintaining relatively high surface energy. It effectively protects the VTE front cell from the penetration by the solution-processed back cell active layer.

## 6.2.3 Tandem performance and fabrication yield
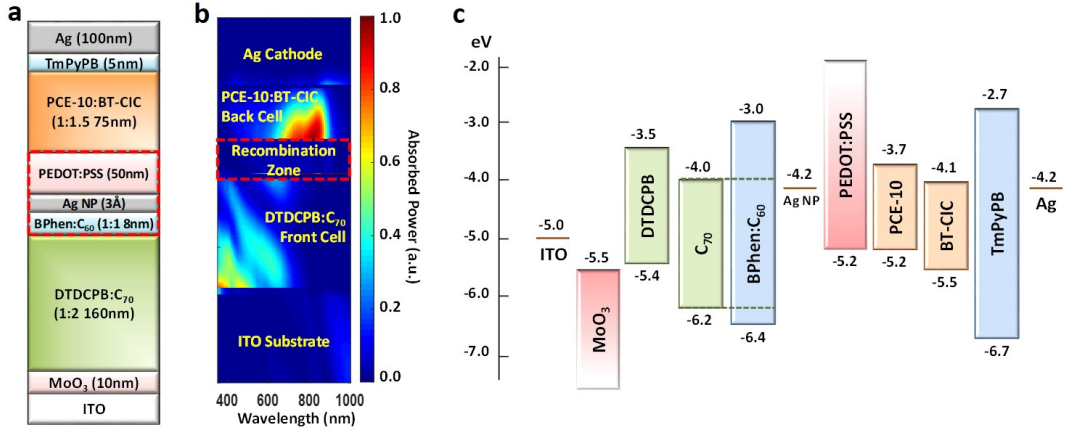
Figure 6.6: Tandem cell combining NFA-based and VTE subcells. a) Schematic of the tandem device, with the recombination zone highlighted by the red dashed box. b) Simulated absorbed optical power density distribution (relative). c) Tandem cell energy level diagram.

The tandem OPV comprises the NIR NFA-based cell on the surface of the vacuum-deposited DTDCPB:C_{70} cell, separated by the BPhen:C_{60}/Ag NP/PEDOT:PSS CRZ (see Fig. 6.6a for the detailed structure). The simulated relative absorbed power distribution is displayed in Fig. 6.6b. The largest absorption occurs within the back cell in the NIR between 700 nm and 900 nm; while the visible light absorption in the front cell without the reflecting metal cathode is less intense, requiring a thicker active layer to balance with the back cell. On the other hand, the CRZ shows almost no absorption, indicating minimal optical loss. The energy level diagram is shown in Fig. 6.6c. A 2 mm^2 tandem cell with a 165 ± 5 nm thick 1:2 DTDCPB:C_{70} layer in the front cell achieves $14.3 \pm 0.3\%$ under 1 sun, simulated AM 1.5G solar irradiation (see Table 6.3).

The measured EQE spectra of the single junction DTDCPB:C_{70} (1:2, 160 nm) and PCE-10:BT-CIC (1:1.5, 75 nm) cells are plotted in Fig. 6.7 left (circles and triangles, respectively). The subcells absorb between $\lambda = 350$ nm and 950 nm, both exhibiting a peak $EQE > 70\%$. The quantum efficiencies of the front and back junctions measured

at NREL as well as the sum of the two in the tandem are shown by the lines. The tandem cell features a nearly wavelength-independent quantum efficiency $> 70\%$ from $\lambda = 400$ nm to 900 nm. The PCE-10:BT-CIC cell in the tandem exhibits a reduced EQE at $\lambda < 750$ nm compared to the single junction cell due to residual absorption by the DTDCPB:C_{70} cell. The combination of spectral coverage and efficiency leads to a balanced current and minimal absorption overlap between the two stacked subcells.
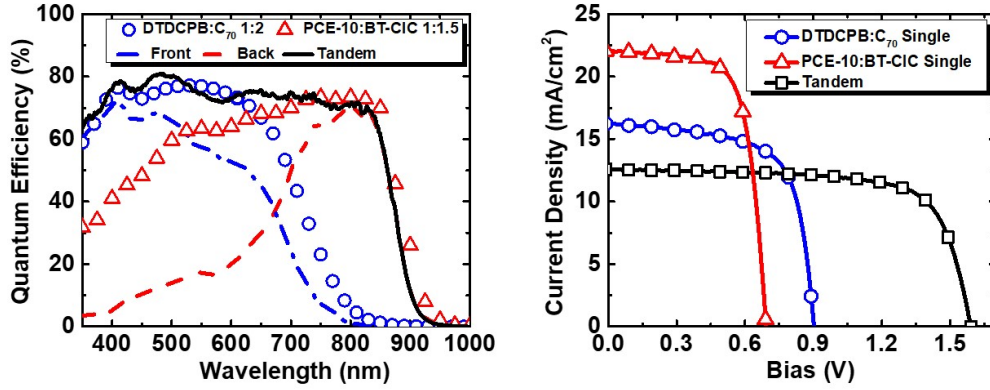
Figure 6.7: Tandem cell performance combining NFA-based and VTE subcells. (Left) Measured quantum efficiencies of the tandem and discrete subcells; (Right) J-V characteristics of the optimized tandem cell together with the single junction subcells.

Figure 6.7, right, shows the J-V characteristics of the optimized, 2 mm^2 tandem cell with 160 nm DTDCPB:C_{70} thickness, together with the discrete subcells. The tandem cell exhibits $J_{SC} = 12.6 \pm 0.2$ mA/cm^2, $V_{OC} = 1.58 \pm 0.01$ V and $PCE = 14.3 \pm 0.3\%$, with $FF = 0.72 \pm 0.01$ higher than both single junction cells. A further increase of the DTDCPB:C_{70} thickness to 170 nm increases the J_{SC} to 12.7 ± 0.2 mA/cm$_2$ while the FF slightly decreases to 0.71 ± 0.01, achieving a similar efficiency of $14.3 \pm 0.3\%$. The reduction in the tandem cell V_{OC} compared with the sum of the V_{OC} of the subcells is smaller than 20 meV, implying that the CRZ is nearly electrically lossless. The performance of the 9 mm^2 tandem cells shows 2% (relative) lower efficiency than the 2 mm^2 devices, giving $J_{SC} = 12.7 \pm 0.2$ mA/cm^2, $V_{OC} =$

| Tandem Area	Total	Working	Yield
2mm²	88	85	97%
9mm²	43	41	95%
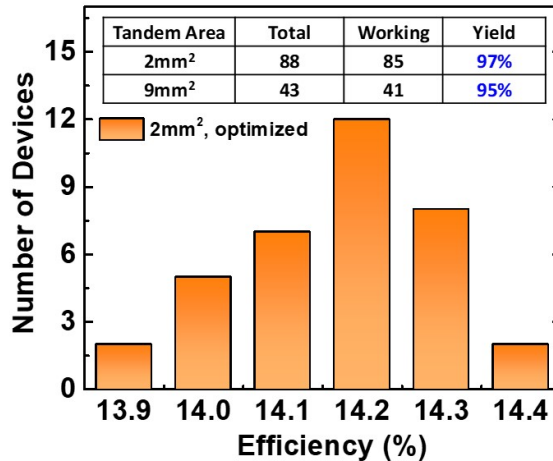
Figure 6.8: Tandem efficiency histogram and device yield. Efficiency histogram for a population of 36 optimized tandem cells (2 mm² effective area, without antireflection coatings). Inset: Tandem cell fabrication yield for populations of 2 mm² and 9 mm² devices.

1.57 ± 0.01 V, $FF = 0.72$ and $PCE = 14.3 \pm 0.3\%$. The difference in FF is due to variations between batches of commercially supplied ITO.

Figure 6.8 shows a histogram of $PCEs$ for a population of 36 tandem devices (2 mm²) with the optimized structures. The efficiencies fall in a narrow range between 13.9% and 14.4% with the mean value of 14.2%. A total population (including both optimized and unoptimized structures) of 88, 2 mm² tandem cells was characterized with results tabulated in Fig 6.8, inset. Of these, 85 devices had a spread in efficiencies < 3% for each device structure, corresponding to a 97% device yield. A similar yield of 95% is observed for a population of 43, 9 mm² tandem cells. The hydrophilic-hydrophobic interface between PEDOT:PSS and the underlying films in the recombination zone therefore acts as a robust protecting cap of the VTE films that results in near perfect device yield.

To reduce optical losses, an ARC was grown onto the glass substrate after the devices were complete. It consists of a bilayer of 120 nm MgF$_2$ (index of refraction, $n_{MgF_2} = 1.38 \pm 0.01$) and 130 nm low refractive index SiO$_2$ ($n_{SiO_2} = 1.12 \pm 0.03$ obtained via glancing-angle deposition[113,114]. The MgF$_2$ was deposited by VTE
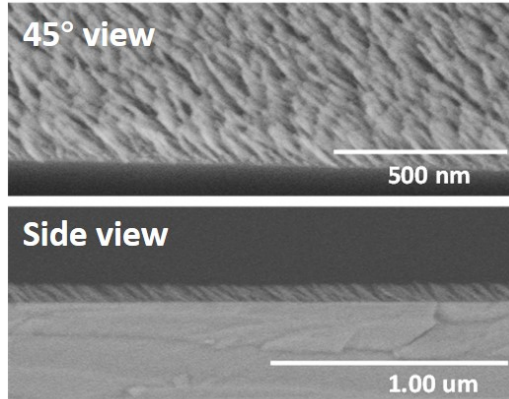
Figure 6.9: Scanning electron microscope (SEM) 45° and side views of the SiO$_2$ film (porous), deposited on the Si substrate with 85° oblique angle.

while the SiO$_2$ was grown by electron beam deposition with the substrate at an angle of 85° to the beam direction. The scanning electron microscope (SEM) images of the SiO$_2$ is shown in Fig. 6.9 with the 45° and side views. The SiO$_2$ presents the porous morphology with tilted pillars standing on the substrate, thereby achieving lower refractive index of $\sim$ 1.1 compared with original value of 1.4 - 1.5 grown without substrate tilting.
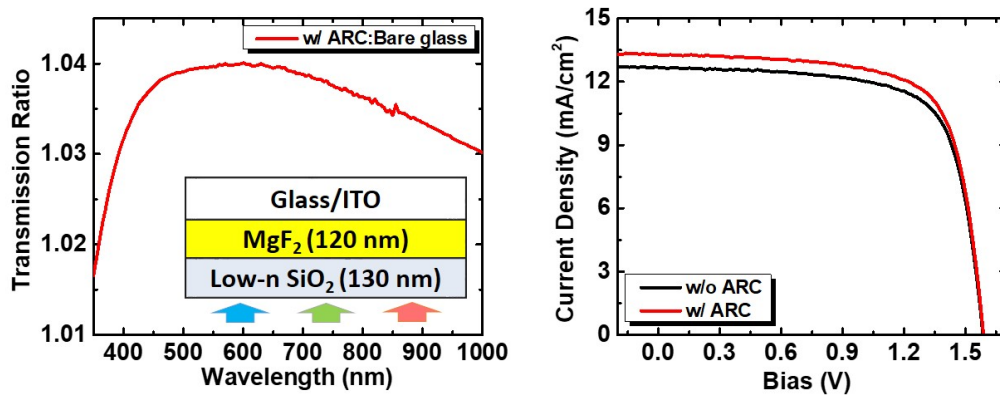
Figure 6.10: Tandem cell performacne with antirefelction coating. (Left) Measured transmission ratio between the glass substrates with and without the antireflection coating (ARC). *Inset:* ARC structure; (Right) *J-V* characteristics of the tandem cells with and without ARC.

The transmission ratio of the glass substrate with and without the ARC increases

by 3% - 4% between $\lambda = 400$ nm and 1000 nm (Fig. 6.10, left). The ARC-coated tandem cell with 170 nm thick 1:2 DTDCPB:C_{70} and 2 mm^2 area shows an increase in J_{SC} from 12.7 ± 0.2 mA/cm^2 to 13.3 ± 0.3 mA/cm^2 to achieve $PCE = 15.0 \pm 0.3\%$, a milestone efficiency for OPV commercialization. The performance parameters and J-V characteristics are shown in Table 6.3 and Fig. 6.10 (right). The 9 mm^2 tandem cell shows similar J_{SC} improvement with ARC, exhibiting $PCE = 14.5 \pm 0.3\%$.

**Table 6.3:** Tandem performance with PCE-10:BT-CIC and DTDCPB:C_{70} subcells.

Device*	J_{SC} (mA/cm^2)	V_{OC} (V)	FF	PCE (%)
Tandem (w/ 160nm DTDCPB:C70)	12.6 ± 0.2	1.58 ± 0.01	0.72 ± 0.01	14.3 ± 0.3
Tandem (w/ 170nm DTDCPB:C70)	12.7 ± 0.2	1.59 ± 0.01	0.71 ± 0.01	14.3 ± 0.3
Tandem (w/ 170nm DTDCPB:C_{70} + ARC)	13.3 ± 0.3	1.59 ± 0.01	0.71 ± 0.01	15.0 ± 0.3

* 2 mm^2 device area.

6.2.4   Large area tandem OPVs

A 1 cm^2 tandem cell on patterned ITO was fabricated and tested to determine if the solution/vapor deposition process could be successfully employed over larger areas. The device without ARC grown on the patterned ITO exhibits $J_{SC} = 12.6 \pm 0.3$ mA/cm^2, $V_{OC} = 1.58 \pm 0.01$ V, $FF = 0.57 \pm 0.01$ and $PCE = 11.5 \pm 0.3\%$ (see J-V characteristics in Fig. 6.11). For comparison, the device performance with different areas (without ARC) are summarized in Table 6.4 and the FF trends at different incident power densities are shown in Fig. 6.11, right.

As listed in Table 6.4, the J_{SC} for a 1 cm^2 cell is consistent with 2 mm^2 and 9 mm^2 cells independent of device area, which indicates the measurement accuracy. This larger device also affirms the scalability of the solution/vapor deposition process.
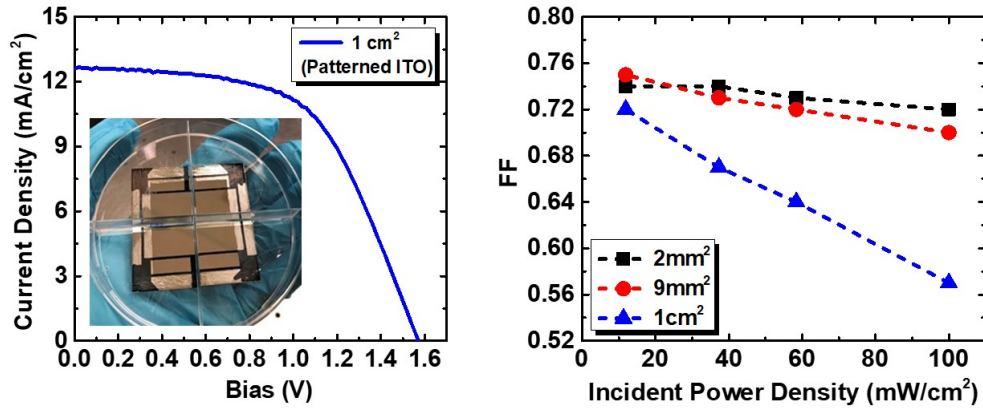
Figure 6.11: 1 cm^2 tandem cell performance. (Left) *J-V* characteristics of 1 cm^2 tandem cells without ARC. *Inset:* Photo of four 1 cm^2 cells; (Right) *FF* as a function of incident light power density for different device areas.

Table 6.4: Tandem performance with different device areas (without ARC).

Area	J_{SC} (mA/cm^2)	V_{OC} (V)	FF	PCE (%)	R_s ($\Omega \cdot cm^2$)
2 mm^2	12.6 ± 0.2	1.58 ± 0.01	0.72 ± 0.01	14.3 ± 0.3	2.7 ± 0.2
9 mm^2	12.7 ± 0.2	1.57 ± 0.01	0.70 ± 0.01	14.0 ± 0.3	5.6 ± 0.5
1 cm^2	12.6 ± 0.3	1.58 ± 0.01	0.57 ± 0.01	11.5 ± 0.3	28 ± 2

Compared with smaller area cells, the only difference is in *FF*, which decreases by $\sim$ 20% from > 0.7 to 0.57. It follows the trend of the increasing series resistance (R_S) from 2 mm^2 ($2.7 \pm 0.2\ \Omega \cdot cm^2$) to 1 cm^2 ($28 \pm 2\ \Omega \cdot cm^2$) by one order of magnitude. From Fig. 6.11 we find that at low power density $\sim$ 0.1 sun, the *FF* of different areas converges to > 0.72. With increasing incident power, the *FF* of 2 mm^2 and 9 mm^2 cells show slight decrease, while the 1 cm^2 cell decreases dramatically from 0.72 at 0.1 sun to 0.57 at 1 sun. It confirms the reduction in *FF* is due to the R_S of the patterned ITO as the area and current density increases, consistent with previous analyses.[115] Reducing the R_S by using a thicker ITO, a sub-anode contact, or a metal grid are likely to further improve the large area device *FF* and *PCE*.

6.2.5 *FF* analysis
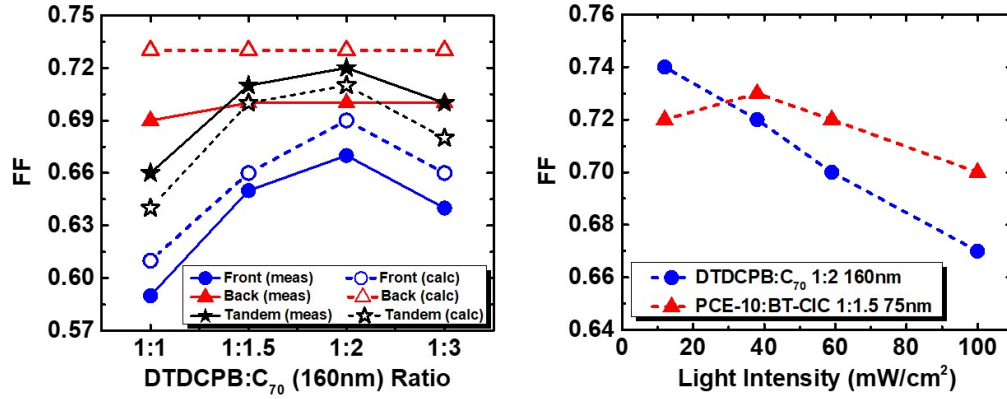
Figure 6.12: Tandem *FF* analysis. (Left) The *FF*s of subcells and tandems cells (2 mm^2) as functions of DTDCPB:C$_{70}$ blend ratios. (Right) The *FF vs.* light intensity for the single junction subcells. The error bars for the measured ($\pm$ 0.01) and calculated ($\pm$ 0.02) data are omitted for clarity.

The tandem cells exhibit *FF* > 0.7 which is higher than both single junction cells, contributing significantly to the *PCE*. To understand this phenomenon, the measured and calculated *FF*s of the tandems and subcells (2 mm^2) with different DTDCPB:C$_{70}$ ratios are plotted in Fig. 6.12, left. The solid circles and triangles represent the measured values of the single junction DTDCPB:C$_{70}$ (160 nm) and PCE-10:BT-CIC (75 nm) cells under AM 1.5G, one sun illumination. Figure 6.12, right, plots the measured *FF* of the two cells as a function of incident light intensity from 0.1 to 1 sun. Both subcells show increasing *FF* with lower light intensity due to reduced bimolecular recombination at smaller current densities. When the two cells are stacked in tandem, the light intensity and current within each subcell is smaller than in the discrete single junction cells. The calculated *FF*s of the subcells in the stack shown in Fig. 6.12 left are therefore higher than their single junction counterparts. According to optical simulations, the front DTDCPB:C$_{70}$ is operated at an equivalent 0.7 to 0.8 sun intensity that results in an increase in *FF* by as much as 0.02 (open circles); the back PCE-10:BT-CIC cell operates at a relatively

low intensity of ~ 0.5 sun corresponding to $FF = 0.73 \pm 0.02$ (open triangles). The calculated tandem FF (open stars) lies between the calculated FFs of the two subcells and matches with the measured values (solid stars) within the simulation error ($\pm$ 0.02), confirming that the higher tandem FF is due to the reduced light intensity within each subcell.

6.2.6   Efficiency outlook

The thermodynamic efficiency limit of single junction OPVs has been shown to be between 22% and 27%, with the actual value determined by the energy loss from exciton and polaron pair binding subsequent to their optical generation.[44] Multijunction solar cells can outperform the single junction thermodynamic limit, which suggests that there is large room for improvements in the OPV efficiency described here. For example, NFAs-based OPVs exhibit efficient charge separation with a relatively small energy loss ($E_{loss} < 0.6$ eV)[116,117] compared to $E_{loss} = 0.7$ - 0.8 eV for fullerene-based cells. By replacing the fullerene acceptor of the front cell with an NFA, the tandem V_{OC} can be increased by approximately 0.2 V. In addition, the NFA-based back cell FF is as high as 0.70 due to ordered intermolecular stacking of the planar molecules, leading to a tandem $FF = 0.72$. Thus, increasing the front cell FF from 0.67 to above 0.7, again through replacement of the fullerene with an NFA, a tandem $FF = 0.75$ is likely to be achieved. Further, the average tandem quantum efficiency still has room for improvement from 75% to $> 90\%$ by stacking of three or more subcells using the variety of deposition techniques. Based on these assumptions, we can expect a 20% relative increase in efficiency of multijunction OPVs to PCE 18% in the near future. Theoretical efficiency calculations will be presented in Chapter VII.

6.3 National Renewable Energy Laboratory (NREL) measurement
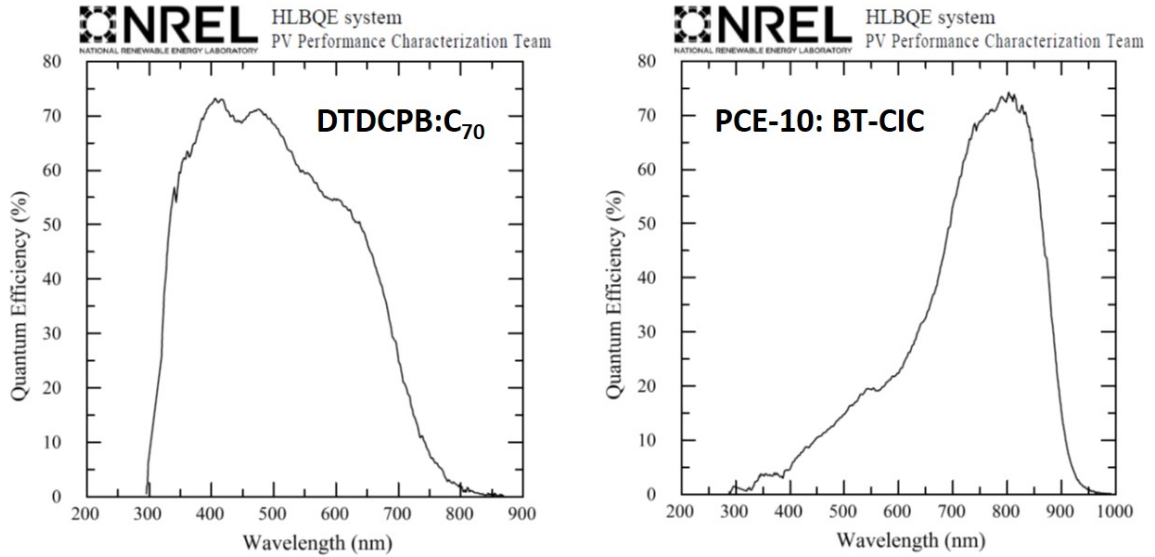
Figure 6.13: Quantum efficiencies measured by NREL. Quantum efficiencies of DTDCPB:C_{70} front cell and PCE-10:BT-CIC back cell in the optimized tandem stack (2 mm^2 device with ARC) measured by NREL.
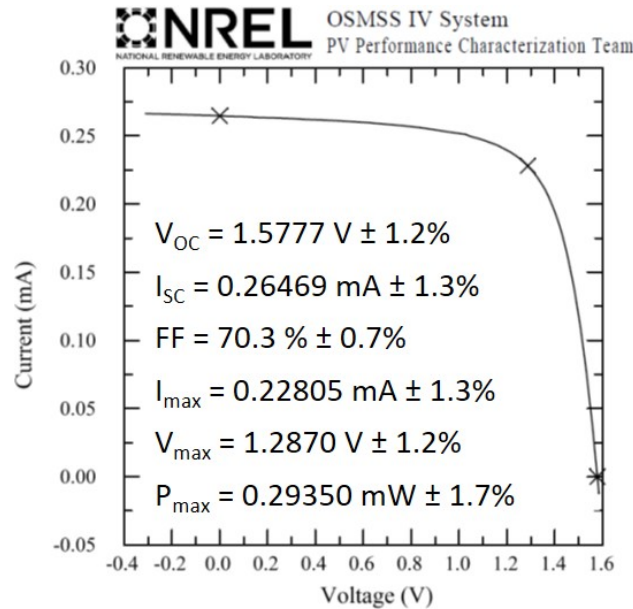
Figure 6.14: *I-V* characteristics measured by NREL. NREL measured tandem cell *I-V* characteristics (2 mm^2 device with ARC), with the extracted efficiency of $14.7 \pm 0.3\%$.

**Table 6.5:** Extracted efficiencies of 8 tandem cells (with ARC) measured at NREL.

Tandem Area	#1	#2	#3	#4
2 mm²	14.7%	14.6%	14.6%	14.7%
9 mm²	14.4%	14.3%	14.4%	14.3%

* The NREL measurements reported were not certified due to a moratorium on OPV certification to allow for a system upgrade at the time of our request.

Efficiencies of both the 2 mm² and 9 mm² tandem cells encapsulated in the N_2 environment were measured by NREL to cross-check their performance. For quantum efficiency measurements, the NIR-absorbing back cell was biased by an unfiltered red-rich Xe lamp while the visible-absorbing front cell was biased by a Xe lamp with a 600 nm short wavelength passband filter. The current-voltage (I-V) characteristics (unmasked) were then measured by the One-Sun Multi-Source Simulator (OSMSS).[118]

The solar simulator spectrum was adjusted based on the measured EQE to achieve the same mismatch factor for all subcells (between 0.997 to 1.005). The measured subcell quantum efficiencies and tandem J-V characteristics (2 mm² with ARC) are shown respectively in Fig. 6.13 and 6.14. All three device parameters measured by NREL (Fig. 6.14) are slightly lower than the result in Table 6.3 measured in our lab, leading to the extracted efficiency of 14.7 ± 0.3%. The extracted efficiencies of the 2 mm² and 9 mm² tandems with ARC are listed in Table 6.5. The 4 cells measured for each area present very consistent performance, confirming the uniformity of the tandem devices. Both efficiencies are within experimental and statistical errors of results obtained on similar cells in our laboratory, taking account the solar simulator spectrum variations and possible degradation during shipment.

The same cells shown in Table 6.5 were measured in our lab with and without a mask. The J_{SC} with the mask is $\sim$ 2% lower than the unmasked case, which is likely due to the non-negligible mask thickness compared with the aperture size. The J-V characteristics of the tandem cells are reproducible from device to device
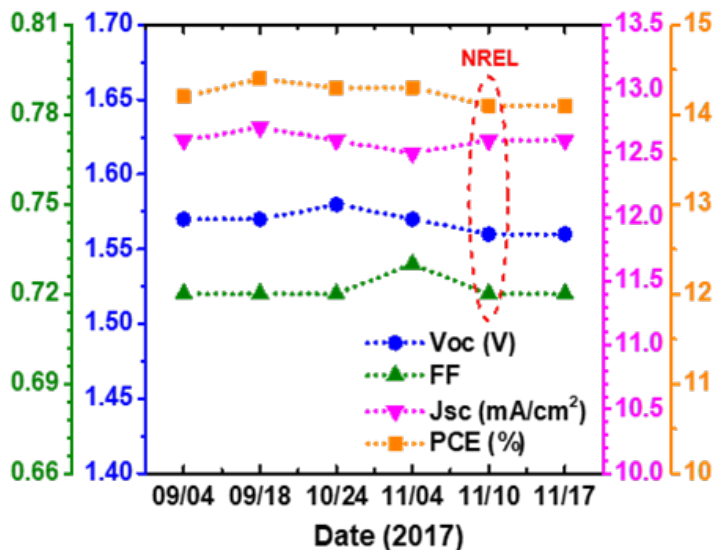
Figure 6.15: Measured tandem performance parameters over time (2 mm^2 tandem w/o ARC).

and run to run, and are independent of the light exposure time (1-5 min). The cells were measured at NREL more than 2 months after fabrication, showing stable performance with little or no apparent degradation. The parameters plotted in Fig. 6.15 are measurements of the same cell from the fabrication date (09/04/2017) to one week after it was shipped back from NREL (11/17/2017). The data points for 11/10 were measured by NREL, and other measurements were done in our lab. The devices were kept in the dark between measurements. The data show the device is stable over the two months with reproducible results. It is worth noting that we obtained the same parameters as NREL after the cell was returned, with a slightly lower *PCE* than before, which may be due to handing during shipment. The methods to improve the cell stability under continuous illumination are still under study.

6.4 Summary

In summary, a high efficiency tandem OPV structure is demonstrated with the NIR-absorbing NFA-based PCE-10:BT-CIC back cell spin-coated onto the visible-

absorbing VTE-grown DTDCPB:C_{70} front cell. The cell broadly absorbs the solar spectrum between $\lambda = 350$ nm and 950 nm. The nearly optically and electrically lossless CRZ comprising the PEDOT:PSS cap on a Ag nanoparticle layer adjacent to a BPhen:C_{60} electron filtering/exciton blocking layer protects the VTE-grown cell from damage during the solution deposition of the NFA active layer. This results in $> 95\%$ tandem device yield out of > 130 devices measured in total with 2 mm^2 and 9 mm^2 device areas, and has been successfully extended to yield 1 cm^2 devices with the same structure. The 2 mm^2 and 1 cm^2 tandem cell deliver $PCE = 14.3 \pm 0.3\%$ and $11.5 \pm 0.3\%$, respectively. The ARC coated glass substrate increases the light in-coupling, yielding a maximum $PCE = 15.0 \pm 0.3\%$. The combination of VTE deposition and solution processing, along with fullerene and NFA subcells provides design and fabrication routes previously unavailable to the fabrication of multijunction OPVs. An NFA-based OPV multijunction efficiency of $\sim 18\%$ is projected based on the design principles demonstrated here.

CHAPTER VII

Is There a There There?

This dissertation has introduced the development and state of the art of the OPV efficiency, especially for vacuum-deposited cells. The recent fast-pace development makes OPV relevant again among thin film solar technologies. So, how much more can it be improved? Will it be competitive in the solar market?

Figure 7.1 shows the efficiency development over time of the main thin film solar technologies. The CdTe and CIGS have the longest history with gradual development over the past 40 years, achieving $\sim 22\%$ efficiency.[24,25] Perovskites are able to get similar efficiency with a much shorter time period starting from 2013. All of the three technologies, however, contain toxic materials such as Cd and Pb, leaving potential problems of packaging and material disposal. Especially for perovskites, water-soluble Pb compounds may cause serious environmental issues, while their poor reliability is another concern.[119] On the other hand, α-Si, dye-sensitized solar cells (DSSCs), OPVs and quantum dot (QD) solar cells display relatively lower efficiencies between 10-15%. There has not been much development of α-Si and DSSC over the past 20 years with the *PCE*s staying at 12-13%, which has led to a reduced research interest. The QD solar cell efficiency has improved from $\sim 3\%$ to $> 13\%$ since 2010.[120] However, it also has toxic and stability issues. For OPV cells, the efficiency remained at $\sim 11\%$ between 2012 and 2016, followed by a big jump recently to 15%
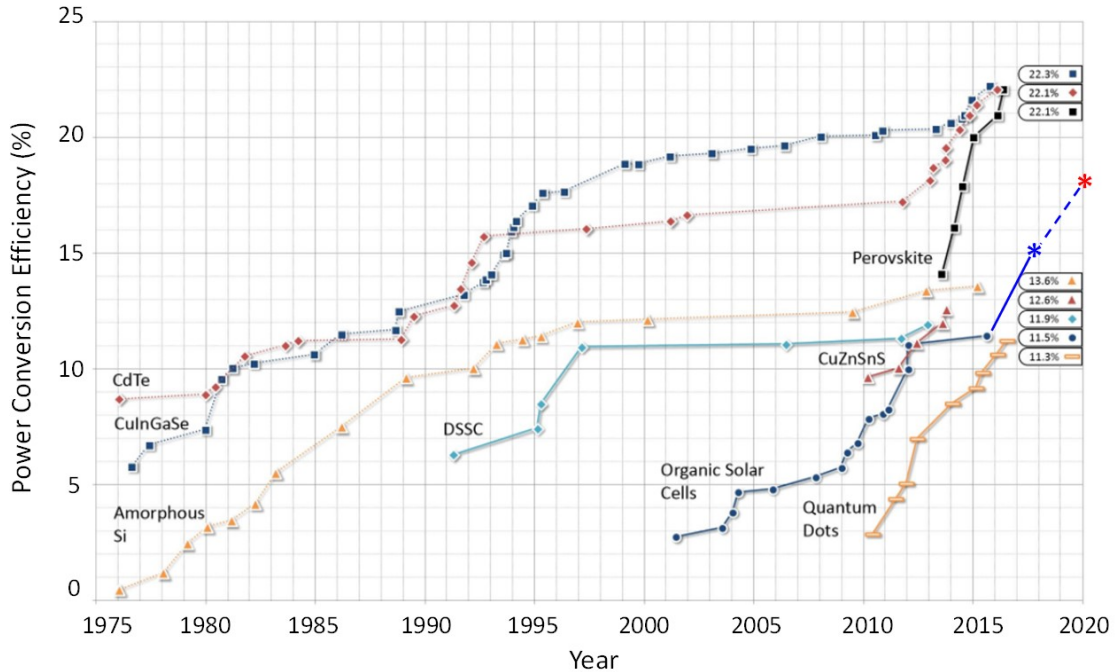
Figure 7.1: Thin film solar cells efficiency development chart. Figure from the website www.ossila.com.

with the emergence of non-fullerene acceptors. As discussed in Chapter VI, a further improvement to $\sim 18\%$ can be expected by 2020, as marked by the dashed blue line in the chart. It could therefore outperform many of the thin film technologies with a very low cost and environmental friendly production. We will discuss below the possible pathways to achieve better OPV efficiencies supported by theoretical calculations.

7.1 The trend

From the early 2000s, OPV efficiency has improved faster than any other thin film solar technologies except perovskites. As seen from Fig. 7.1, perovskite cells experienced phenomenal development between 2013 and 2016, during the OPV bottleneck period. This diverted attention from OPVs at a critical time. However, the recent emergence of NFAs has renewed interest in the development of OPV. It has led to a 30% (relative) efficiency increase in 2 years, and the trend is likely to continue.
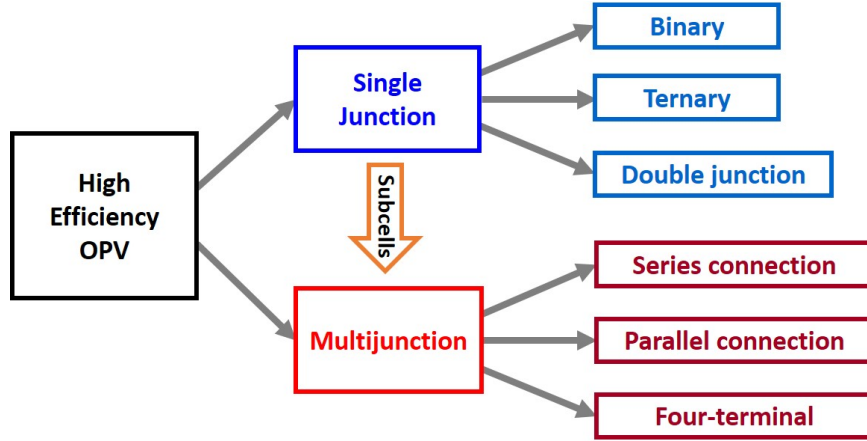
Figure 7.2: Routes for high efficiency OPVs.

Figure 7.2 shows the routes for achieving high efficiency OPVs, which can be divided into single and multijunction cells. Traditional single junction cells employ a binary structure, where the active layer contains one donor and one acceptor material. The ternary cell is achieved by adding an additional donor or acceptor molecule, with > 12% efficiency reported.[61] A double heterojunction structure has also been demonstrated by directly stacking two binary blend active layers.[121] Both the ternary and double junction can effectively improve the active layer absorption and thus J_{SC}, while the FF and V_{OC} often are not limited by the lower boundary among the two binary cells. The mechanism that determines V_{OC} and FF of the ternary and double junction devices is currently an important research topic[122], which can lead to further efficiency improvements by choosing the appropriate material sets. Ternary structures with NFAs are likely to lead the new trend for high efficiency OPVs.[123,124]

The multijunction structure contains a stack of single junction subcells, which can be connected in series, in parallel, or even measured separately as a four-terminal structure[125]. Combinations of high efficiency single junction subcells do not necessarily lead to high efficiency multijunction cells. It requires balanced current density for series connection, balanced voltage for parallel connection, as well as a board coverage of solar spectrum with small energy losses that leads to a large V_{OC}. The NFAs

are a popular choice for this reason. Theoretical calculations of both single and multijunction cells are performed below that predict the practical OPV efficiency limits using various device architectures.

7.2 Theoretical calculations

7.2.1 Opaque OPVs

To estimate efficiency prospects based on foregoing results, we assume a device can achieve 90% EQE over the wavelength between 350 and 1100 nm. The FF is set to be a constant of 0.75. The energy loss, E_{loss}, is defined as the difference between the lowest absorbed photon energy (i.e. the optical gap E_{opt}) and the V_{OC}. For a single junction cell with a long absorption edge of 900 nm (E_{opt} = 1.38 eV) and a energy loss of 0.5 eV, for example, the calculated efficiency would be:

$$PCE_{theory} = \frac{30.2mA/cm^2 \times (1.38 - 0.5)V \times 0.75}{100mW/cm^2} = 19.9\%, \tag{7.1}$$

where J_{SC} = 30.2 mA/cm^2 is calculated by integrating EQE = 90% over the AM 1.5G solar spectrum up to 900 nm.
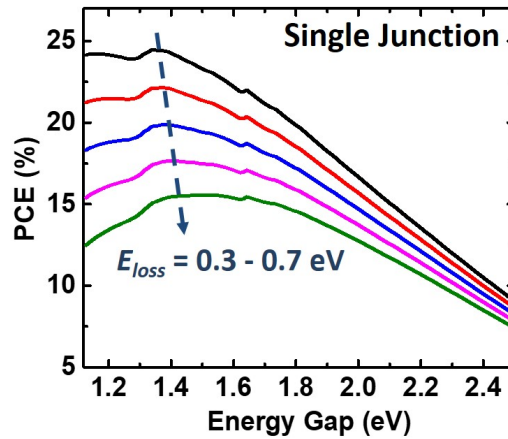
Figure 7.3: Efficiency calculations of single junction opaque OPVs, with the energy loss (E_{loss}) from 0.3 eV to 0.7 eV.

135

Figure 7.3 plots the calculated efficiency as a function of the single junction E_{opt} with different E_{loss}. As expected, the efficiency goes up as E_{loss} decreases from 0.7 eV to 0.3 eV. With the trade off between J_{SC} and V_{OC}, the maximum efficiency is achieved with $E_{opt} \sim 1.4$ eV, i.e. the absorption onset around 900 nm. The peak wavelength shows a slight blue shift from 920 nm to 850 nm as E_{loss} goes up. As calculated from Eq. 7.1, the device with $E_{loss} = 0.5$ eV could achieve the maximum $PCE = 19.9\%$. Further reducing E_{loss} to 0.3 eV, if possible, gives $PCE = 24.5\%$.
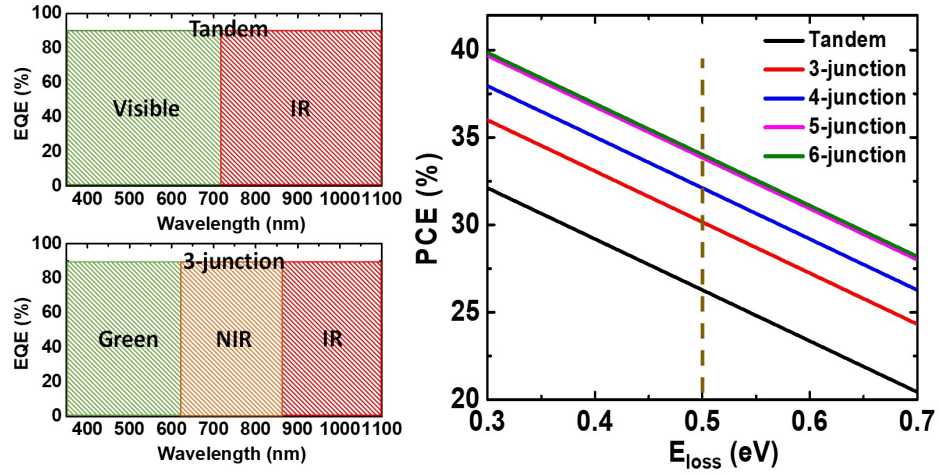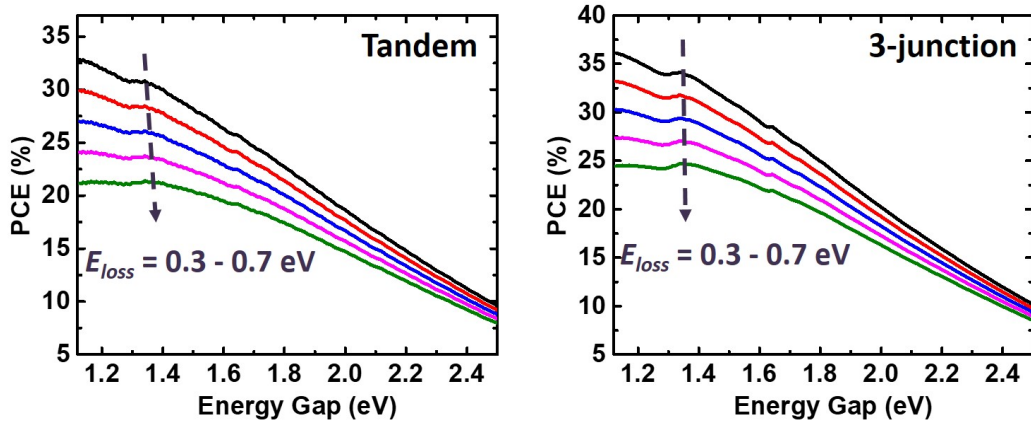

Figure 7.4: Efficiency calculations of multijunction opaque OPVs with 2-6 subcells, as a function of E_{loss}. The subcells are connected in series with balanced. The subcell *EQE* distributions in tandem and triple-junction cells are shown on the left.

For multijunction cells, the absorption edge is first set to be 1100 nm ($E_{opt} \approx 1.1$ eV). Again $EQE = 90\%$ over the spectrum, while the J_{SC} is divided evenly among the subcells in a series connection, as shown in Fig. 7.4 on the left with examples of tandem and triple-junction structures. The J_{SC} generated under AM 1.5G solar spectrum up to 1100 nm with $EQE = 90\%$ is 38.9 mA/cm². Therefore the tandem cell J_{SC} for this calculation is $38.9/2 = 19.5$ mA/cm², and for a triple-junction cell it is $38.9/3 = 13.0$ mA/cm² etc. We assume there is no absorption overlap between the subcells and that the absorption onset of each subcell is found according to the current density of the multijunciton cell. The V_{OC} of the multijunction cell is then

the sum of subcell V_{OC} (= E_{opt} - E_{loss}).

Figure 7.4, right, shows the calculation of multijunciton efficiencies with up to 6 subcells in series as a function of E_{loss} (per subcell). All structures have the same slope, with $\sim 12\%$ PCE decrease as E_{loss} goes from 0.3 eV to 0.7 eV. Due to the accumulated V_{OC}, the efficiency first increases with the number of subcells and saturates at 5 junctions. There is the largest efficiency jump from the tandem to triple junction, with $PCE = 26.3\%$ and 30.2% respectively, at $E_{loss} = 0.5$ eV. Adding additional subcells could improve the efficiency $> 35\%$ in theory, while it may not be practical to fabricate due to material and processing limitations.

Figure 7.5: Efficiency calculations of tandem (left) and triple-junction (right) opaque OPVs, with the energy loss from 0.3 eV to 0.7 eV.

The tandem and triple-junction efficiency is also calculated as a function of the optical gap of the reddest subcell, as shown by Fig. 7.5. In contrast to the single junction that shows a peak efficiency at an energy gap of ~ 1.4 eV (900 nm absorption cutoff), the PCE roughly increases with the onset wavelength up to 1100 nm ($E_{opt} \approx$ 1.1 eV). However, the increase becomes much slower beyond 900 nm. Again, taking $E_{loss} = 0.5$ eV as an example, the tandem cells with the absorption onset at 900 nm and 1100 nm are predicted to exhibit efficiencies of 25.7% and 26.9%. In other words, the NIR-absorbing subcell with the absorption edge ~ 900 nm is sufficient for high

efficiency multijunciton OPVs.

From the above calculations, we learn that with similar E_{loss}, the multijunction structures are expected to achieve $\sim 25\%$ relative higher efficiency than the single junction cell. In both cases, the absorption edge around 900 nm with $E_{opt} \sim 1.4$ eV is sufficient, which has already been demonstrated by NFA-based cells with EQE > 70% and $PCE > 11\%$.[35] Longer wavelength absorption does not improve much, or even reduce the efficiency due to the trade-off between the J_{SC} and V_{OC}. The assumption of $EQE = 90\%$ can be challenging, and the limiting factor for the multijunction structure is likely to be the short-wavelength-absorbing subcell with absorption onset < 700 nm while maintaining high EQE. If setting $EQE = 75\%$, the single junction $PCE > 15\%$ and tandem or triple junction $PCE > 20\%$ are still valid according to the calculations. These are realistic targets based on the current OPV development.

7.2.2 Semi-transparent OPVs

One unique OPV feature is its semi-transparency. The donor and acceptor materials have narrow absorption bands, that the material pairs and blend ratios can be adjusted to achieve desired transparency to the visible spectrum. For single junction cells, transparencies (T) of 50% ($EQE = 50\%$) or 100% ($EQE = 0\%$) in the visible at $\lambda < 650$ nm ($E_{opt} = 1.9$ eV) are calculated, with $EQE = 90\%$ at $\lambda > 650$ nm. Such photoresponse characteristics should be possible to achieve using NFA-based ternary cells. The calculated semitransparent single junction efficiencies as functions of the optical energy gap is plotted in Fig. 7.6, showing similar trends as the opaque cell. For $T = 50\%$, the efficiency reaches the maximum at $E_{opt} \sim 1.4$ eV ($\lambda = 900$ nm) when the energy loss is higher than 0.5 eV. With lower E_{loss}, smaller energy gap with absorption deeper into the NIR region to 1100 nm can further increase the efficiency, however, not by much. At $E_{loss} = 0.5$ eV and $T = 50\%$, it gives the maximum $PCE = 15.5\%$ with absorption onset at 930 nm. The OPV cell with $T = 100\%$ and
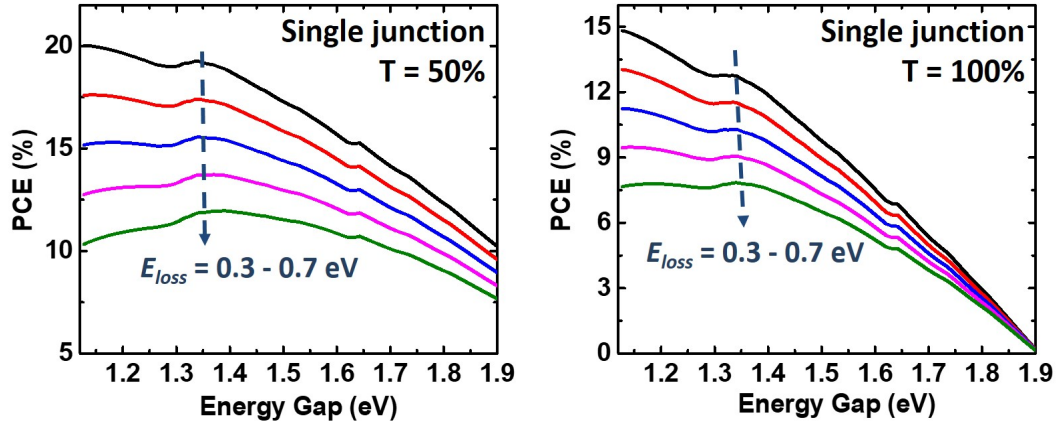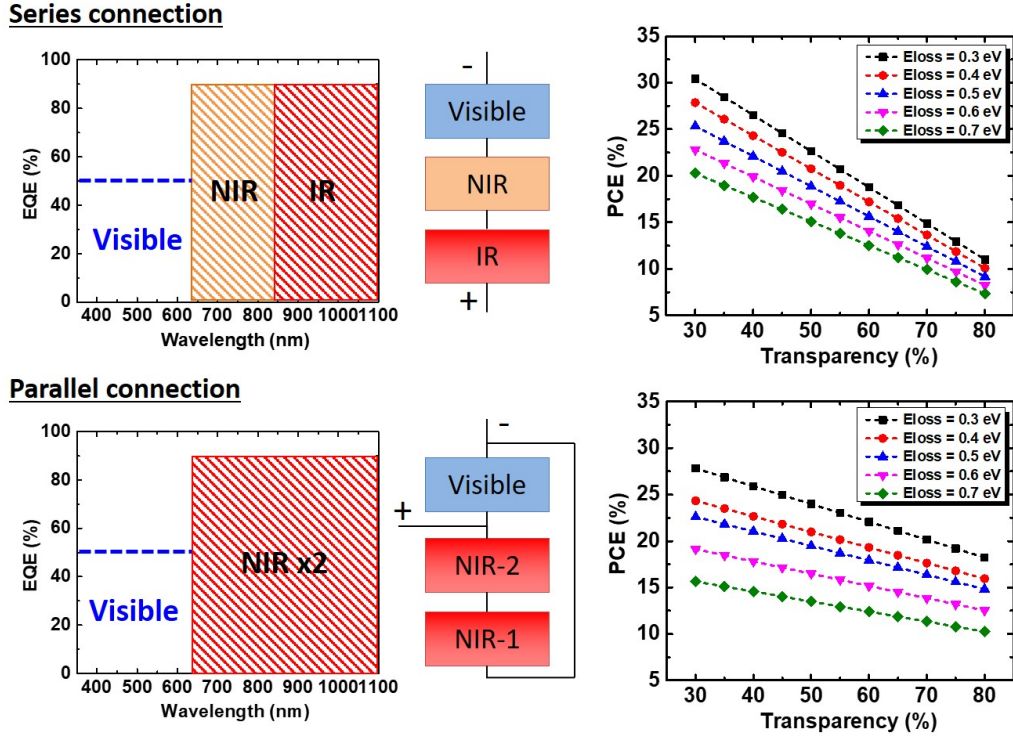
Figure 7.6: Efficiency calculations of single junction semitransparent OPV, with the transparency (T) of 50% or 100% below 650 nm.

$E_{loss} = 0.5$ eV still generates $PCE \approx 10\%$, suggesting that it could be employed as a completely transparent window in the visible while working as a 10% efficient solar cell.

The uneven EQE distribution between the visible and NIR region of semitransparent devices is easier to achieve with multijunction structures. A triple junction cell with one subcell absorbing in the visible and two subcells in the NIR can be connected in series or parallel, as shown by the structures in Fig. 7.7 on the left. In the series connection, the NIR and IR subcells absorb from 640 nm - 840 nm and 840 nm - 1100 nm respectively, with $EQE = 90\%$ and a balanced $J_{SC} = 12.2$ mA/cm^2. The efficiencies are calculated with different visible subcell transparencies from 30% to 80%. Recalling that the J_{SC} of multijunction cells is often between the subcells[72], here we assume the triple junction $J_{SC} = 0.1 \times J_{SC,NIR} + 0.9 \times J_{SC,visible}$, where $J_{SC,NIR}$ and $J_{SC,visible}$ are short-circuit current densities of the NIR- and visible-absorbing subcells. The efficiency is plotted in Fig. 7.7 top right with $E_{loss} = 0.3$ eV - 0.7 eV, giving $PCE = 18.9\%$ at 50% transparency when $E_{loss} = 0.5$ eV, which is higher than $PCE = 15.5\%$ for the single junction. On the other hand, a rapid roll-off towards higher transparencies is observed due to the very low current

139

Figure 7.7: Efficiency calculations of semitransparent triple-junction OPVs, with transparency from 30% to 80%.

density generated in the visible subcell, leading to $PCE < 10\%$ at $T = 80\%$.

To solve the problem of the unbalanced current between the visible and NIR subcells at high transparency, the subcells can be connected in a series-parallel network as shown in Fig. 7.7 bottom. The two NIR subcells absorbing between 640 nm and 1100 nm are connected in series with a total $EQE = 90\%$, then connected in parallel with the visible subcell whose V_{OC} is roughly twice that of the NIR subcell. In this case, a three-terminal connection is required as shown in the middle figure where the current from the visible and NIR regions are summed. The design benefits since the V_{OC} balance does not change with the transparency, which results in a much slower efficiency drop at higher transparency. At $E_{loss} = 0.5$ eV and $T = 50\%$, then $PCE = 19.5\%$. $PCE = 14.8\%$ does not show much decrease as T increases to 80%.

7.3   Conclusion

During the 6 years of my PhD program, I witnessed the OPV efficiency growing from 7% to over 15%. Chapter III and IV introduced several vacuum-deposited donor molecules bearing the d-a-a' structure. The large ground state dipole moment leads to enhanced intra- and inter-molecular charge transfers, resulting in large J_{SC} while maintaining relatively high V_{OC}. The two d-a-a' molecules with propeller donor units described in Chapter III, DTDCTB and DTDCPB, serve as promising NIR-absorbing and green-absorbing subcell candidates, with single junction efficiencies of $\sim 6\%$ and 10%. In addition, a group of d-a-a' molecules with coplanar donor units are discussed in Chapter VI. The molecular conjugation length as well as the side chain configuration are manipulated to understand their effects on device performance. Though iBuBTDC:C_{70} with 9.3% efficiency still does not outperform DTDCPB, its higher absorption and current generation has the potential to be applied to multijunction cells with further structure optimization. The structure-property-performance relations of such d-a-a' molecules also provides design guidance for higher efficiency VTE cells.

The DTDCTB:C_{60} cell is employed as the NIR-absorbing subcell in the fully vaccum-deposited multijunciton structure in Chapter V, paired with DBP:C_{70} green-absorbing subcell. The multijunction with 2-4 subcells were fabricated, achieving $> 10\%$ efficiency. The 15% efficient tandem cell presented in Chapter VI employs the DTDCPB:C_{70} as the visible-absorbing subcell, while the NIR-absorbing subcell is replaced with the solution-processed NFA-based cell PCE-10:BT-CIC with much higher J_{SC} and FF than DTDCTB:C_{60}. The NFA-based OPVs has opened a new era for high efficiency OPVs. Further efficiency improvement is expected with reduced energy losses. The vacuum-deposited NFAs, which has not yet been developed, could be another breakthrough for all vacuum-deposited cells.

Figure 7.8 summaries the three commercialization criteria of OPV: efficiency, cost and lifetime with their expected values. The 14% single junction and 15% multijunc-
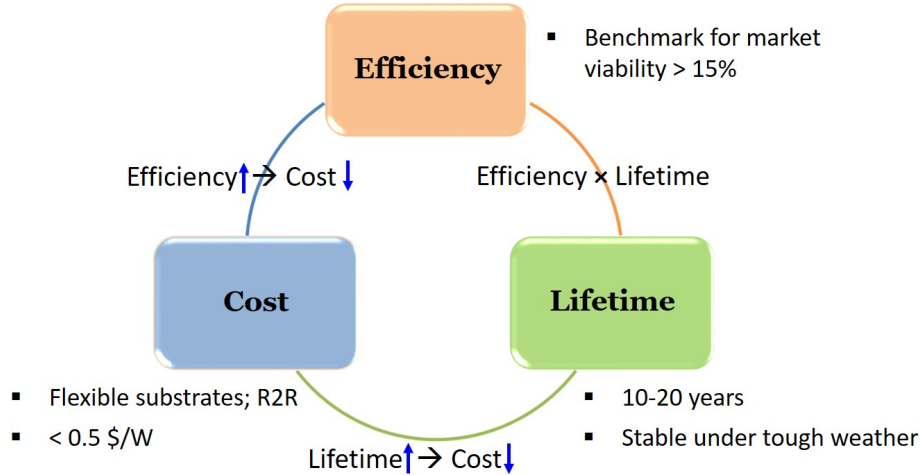
Figure 7.8: OPV commercialization criteria: efficiency, cost and lifetime, and their expected market entry values

tion efficiencies have already been achieved recently in the lab[59], showing potential of OPV technology. Based on the theoretical calculations in this chapter, 15% single junction and 20% multijunction efficiencies are practical targets. On the other hand, there is always a gap between the efficiencies achieved in the lab and the ones in industrial large scale production.[31,115] A 15% module efficiency is likely to require $PCE = 18\%$-20% demonstrated in the lab, which is the multijunction efficiency goal of next step. The material cost for OPV in the industrial scenario (> 100 GW generation) with R2R fabrication was estimated < 0.5 \$/W[126], while it is projected to be further reduced with improved cell performances. Due to the higher material consumptions, the cost of multijunctions in terms of \$/W with current efficiency can be slightly higher than the single junction. Multijunction cells, on the other hand, have advantages in semitransparent applications and also with higher voltage outputs. It is therefore reasonable to conclude that the single and multijunciton cells are equally competitive in the market, while the single junction is likely to step in first due to its lower cost and simpler processing procedures.

Another very important factor for OPV cells is the lifetime. The most recent result in our lab on the vacuum-deposited DBP:C_{70} cell delivers the extracted T_{80} lifetime

longer than 20 years under continuous solar illumination. Multijunction structures with similar material sets but smaller current density than single junctions are expected to achieve even longer lifetimes. The stability of NFA-based OPVs have also been reported with $T_{90} = 2000$ hrs, free of burn-in problems.[127] The stability of high efficiency OPV structures, either solution- or vacuum-processed, have not yet been fully studied. However, it is optimistic to assume that they could achieve similar lifetime with device structure engineering.
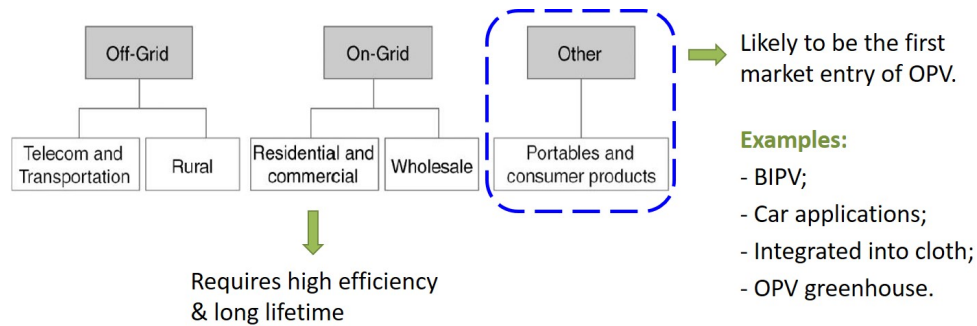

Figure 7.9: Possible OPV market entry - portables and consumer products.

The OPV efficiency and lifetime is not likely to exceed that of Si or GaAs. On the other hand, it does not need to compete with them. The advantages of OPV technology lies in the light and flexible from factors, low-cost fabrications and semi-transparent features. Shown in Fig. 7.9 is the different solar cell applications. Instead of building power stations for on-grid and off-grid electricity generation which requires high efficiency and long lifetime, OPVs are more likely to find their market in portable and consumer products. Some of the examples are building-integrated PVs, applying on cars and clothes, OPV green houses[128] etc. At 15% efficiency, low material cost and 10 to 20 yrs lifetime, OPVs could potentially outperform other thin film technologies for these applications with low module and balance of system (BOS) cost fraction. Whether the OPVs can achieve these goals or not, it should become clear in the next few years.
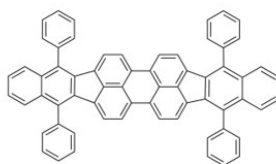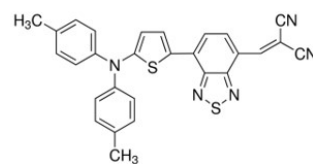
APPENDIX
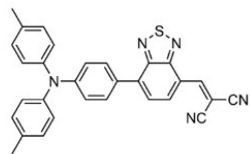
Organic Chemical Structures

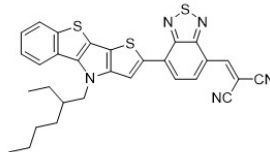## Small Molecule Donors:
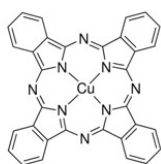
Copper(II) phthalocyanine
(CuPc)

5,10,15,20-tetraphenylbisbenz[5,6]
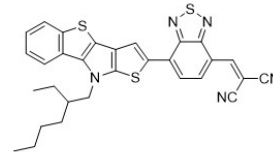indeno[1,2,3-cd:1′,2′,3′-lm]perylene
(DBP)

2-{[7-(5-N,N-Ditolylaminothiophen-2-yl)-2,1,3-
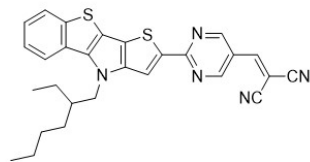benzothiadiazol-4-yl] methylene}malononitrile
(DTDCTB)

2-[(7-{4-[N,N-Bis(4-methylphenyl)amino]
phenyl}-2,1,3-benzothiadiazol-4-yl)
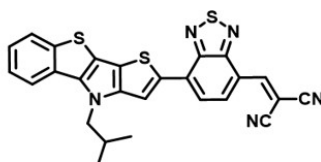methylene]propanedinitrile
(DTDCPB)

2-((7-(N-(2-ethylhexyl)-benzothieno[3,2-
b]thieno[2,3-d]pyrrol-2-yl)benzo[c][1,2,5]
thiadiazol-4-yl)methylene) malononitrile
(anti-BTDC)

2-((7-(N-(2-ethylhexyl)-benzothieno[3,2-
b]thieno[3,2-d]pyrrol-2-yl)benzo[c][1,2,5]
thiadiazol-4-yl)methylene)malononitrile
(syn-BTDC)

2-((2-(4-(2-ethylhexyl)-4H-benzothieno
[3,2-b]thieno[2,3-d]pyrrol-2-yl)
pyrimidin-5-yl) methylene)malononitrile
(PYDC)

2-((7-(N-(isobutyl)-benzothieno[3,2-b]
thieno[2,3-d]-pyrrol-2-yl)benzo[c][1,2,5]
thiadiazol-4-yl)methylene)malononitrile
(iBuBTDC)

2-((7-(N-(n-butyl)-benzothieno[3,2-b]
thieno[2,3-d]-pyrrol-2-yl)benzo[c] [1,2,5]
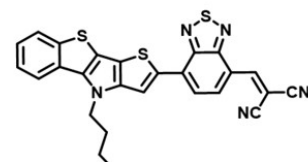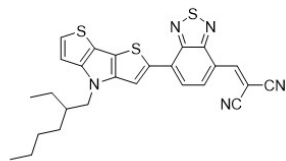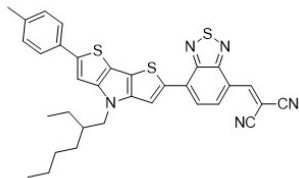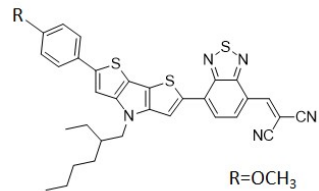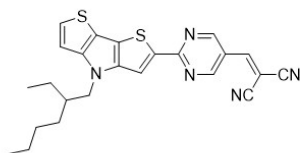thiadiazol-4-yl)methylene) malononitrile
(nBuBTDC)

144

2-((7-(N-(2-ethylhexyl)-dithieno[3,2-b: 2',3'-d]pyrrol-2-yl) benzo[c][1,2,5] thiadiazol-4-yl)methylene)malononitrile

(DBT)

2-((7-(N-(2-ethylhexyl)-6-p-tolyl-dithieno [3,2-b:2',3'-d]pyrrol-2-yl)benzo[c][1,2,5] thiadiazol-4-yl)methylene)malononitrile

(TDBT)

2-((7-(N-(2-ethylhexyl)-6-(4-methoxyphenyl)- dithieno[3,2-b:2',3'-d]pyrrol-2-yl)benzo[c] [1,2,5]thiadiazol-4-yl)methylene)malononitrile

(ADBT)

2-((2-(N-(2-ethylhexyl)-dithieno[3,2- b:2',3'-d]pyrrol-2-yl)pyrimidin-5-yl) methylene)malononitrile

(DPM)
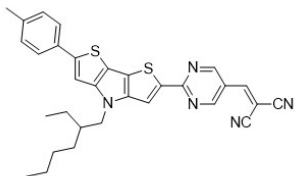
2-((2-(N-(2-ethylhexyl)-6-p-tolyl-dithieno [3,2-b:2',3'-d]pyrrol-2-yl)pyrimidin-5-yl) methylene)malononitrile

(TDPM)
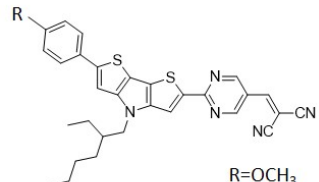
2-((2-(N-(2-ethylhexyl)-6-(4-methoxyphenyl)- dithieno[3,2-b:2',3'-d]pyrrol-2-yl)pyrimidin-5- yl)methylene)malononitrile

(ADPM)
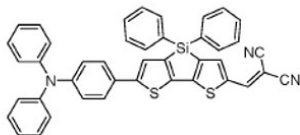
5-[N,N-Bis(phenylamino)phenyl]-5'- dicyanomethylidenemethyl-3,3'- diphenylsilylene-2,2'-bithiophene

(TPDCDTS)
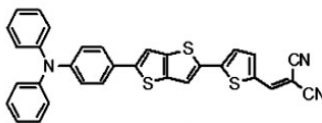
2-((5-(5-(4-(Diphenylamino)phenyl)thieno [3,2-b]-thiophen-2-yl)thiophen-2-yl) methylene)malononitrile

(DTTh)
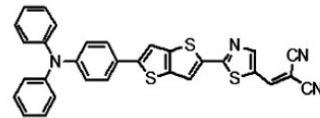
2-((2-(5-(4-(Diphenylamino)phenyl) thieno [3,2-b]-thiophen-2-yl)thiazol-5 yl)methylene)malononitrile

(DTTz)

Small Molecule Acceptors and Buffers:

C$_{60}$

C$_{70}$

Bisbenzimidazo[2,1-a:2′,1′-a′]anthra [2,1,9- def:6,5,10-d′e′f′]diisoquinoline-10,21-dione

(PTCBI)
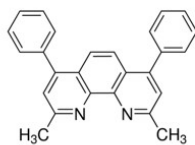
Bathocuproine

(BCP)
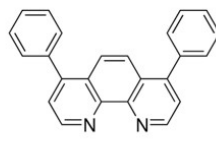
Bathophenanthroline

(BPhen)
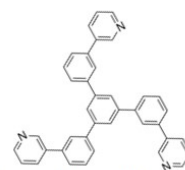
1,3,5-Tri(m-pyridin-3-ylphenyl)benzene

(TmPyPB)

Polymers:
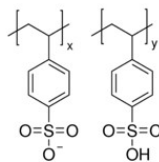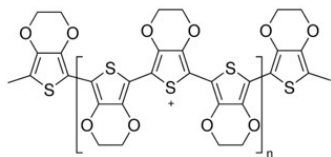
Poly(3,4-ethylenedioxythiophene)-poly(styrenesulfonate)

(PEDOT:PSS)
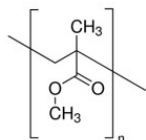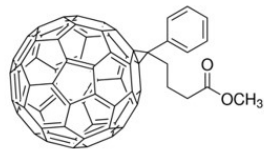
[6,6]-Phenyl C_{61} butyric acid methyl ester

(PC$_{61}$BM)

[6,6]-Phenyl C_{71} butyric acid methyl ester

(PC$_{71}$BM)

Poly(methyl methacrylate)

(PMMA)
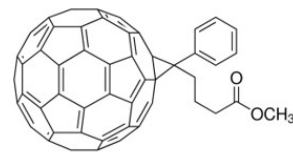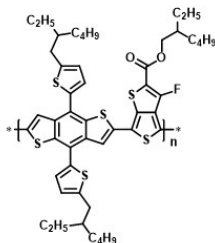
poly[4,8-bis(5-(2-ethylhexyl)thiophen-2-yl) benzo[1,2- b:4,5-b′]dithiophene-co-3-fluorothieno[3,4-b]thio-phene-2-carboxylate]

(PCE-10)
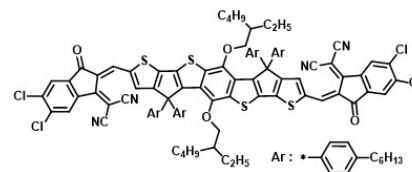
4,4,10,10-tetrakis(4-hexylphenyl)-5,11-(2-ethylhexyloxy)-4,10-dihydro-dithienyl[1,2-b:4,5b′] benzodithiophene-2,8-diyl)bis(2-(3-oxo-2,3-dihydroinden-5,6-dichloro-1-ylidene)malononitrile

(BT-CIC)

BIBLIOGRAPHY

[1] Seager, S. and Slabaugh, M., *Chemistry for Today: General, Organic, and Biochemistry.* Cengage Learning, 2013.

[2] Peumans, P., Yakimov, A. and Forrest, S.R., "Small molecular weight organic thin-film photodetectors and solar cells," *Journal of Applied Physics*, vol. 93, no. 7, pp. 3693–3723, 2003.

[3] Rand, B.P., Genoe, J., Heremans, P. and Poortmans, J., "Solar cells utilizing small molecular weight organic semiconductors," *Progress in Photovoltaics*, vol. 15, no. 8, pp. 659–676, 2007.

[4] Michael M. Coleman, P.C.P., *Fundamentals of Polymer Science: An Introductory Text, Second Edition.* CRC Press, 1998.

[5] Knupfer, M., "Exciton binding energies in organic semiconductors," *Applied Physics A*, vol. 77, no. 5, pp. 623–626, 2003.

[6] Dunlap, W.C. and Watters, R.L., "Direct measurement of the dielectric constants of silicon and germanium," *Phys. Rev.*, vol. 92, no. 6, pp. 1396–1397, 1953.

[7] Harman, A.K., Ninomiya, S. and Adachi, S., "Optical constants of sapphire (al2o3) single crystals," *Journal of Applied Physics*, vol. 76, no. 12, pp. 8032–8036, 1994.

[8] Morgan, S.O. and Yager, W.A., "Dielectric properties of organic components relation to chemical composition and physical structure," *INDUSTRIAL AND ENGINEERING CHEMISTRY*, vol. 32, no. 11, pp. 1519–1528, 1940.

[9] Pope, M. and Swenberg, C.E., *Electronic Processes in Organic Crystals and Polymers.* Oxford University Press, 2nd ed., 1999.

[10] Margenau, H., "Van der waals forces," *Rev. Mod. Phys.*, vol. 11, no. 1, pp. 1–35, 1939.

[11] Born, M. and Oppenheimer, R., "Zur quantentheorie der molekeln," *Annalen der Physik*, vol. 389, no. 20, pp. 457–484, 1927.

[12] Gross, E. and Dreizler, R., *Density Functional Theory.* Nato Science Series B:, Springer US, 2013.

[13] Jordan, P. and Wigner, E., "Über das paulische äquivalenzverbot," *Zeitschrift für Physik*, vol. 47, no. 9, pp. 631–651, 1928.

[14] Burdett, J.J., Mller, A.M., Gosztola, D. and Bardeen, C.J., "Excited state dynamics in solid and monomeric tetracene: The roles of superradiance and exciton fission," *The Journal of Chemical Physics*, vol. 133, no. 14, p. 144506, 2010.

[15] Lax, M., "The franckcondon principle and its application to crystals," *The Journal of Chemical Physics*, vol. 20, no. 11, pp. 1752–1760, 1952.

[16] Kasha, M., "Characterization of electronic transitions in complex molecules," *Discuss. Faraday Soc.*, vol. 9, pp. 14–19, 1950.

[17] Orear, J. and Fermi, E., *Nuclear Physics: A Course Given by Enrico Fermi at the University of Chicago.* Midway Reprints, University of Chicago Press, 1950.

[18] London, F., "The general theory of molecular forces," *Trans. Faraday Soc.*, vol. 33, pp. 8b–26, 1937.

[19] "On the determination of molecular fields. —ii. from the equation of state of a gas," *Proceedings of the Royal Society of London A: Mathematical, Physical and Engineering Sciences*, vol. 106, no. 738, pp. 463–477, 1924.

[20] Slater, J.C. and Koster, G.F., "Simplified lcao method for the periodic potential problem," *Phys. Rev.*, vol. 94, no. 6, pp. 1498–1524, 1954.

[21] "New world record for solar cell efficiency at 46% - french-german co-operation confirms competitive advantage of european photovoltaic industry," *https://www.ise.fraunhofer.de/en/press-media/press-releases/2014/new-world-record-for-solar-cell-efficiency-at-46-percent.html*, Dec 2014.

[22] "26.1% record efficiency for p-type crystalline si solar cells," *https://isfh.de/en/26-1-record-efficiency-for-p-type-crystalline-si-solar-cells/*, Feb 2018.

[23] Powell, D.M. et al, "Crystalline silicon photovoltaics: a cost analysis framework for determining technology pathways to reach baseload electricity costs," *Energy Environ. Sci.*, vol. 5, no. 3, pp. 5874–5883, 2012.

[24] "First solar achieves yet another cell conversion efficiency world record," *http://investor.firstsolar.com/news-releases/news-release-details/first-solar-achieves-yet-another-cell-conversion-efficiency*, Feb 2016.

[25] Kato, T. et al, "Enhanced efficiency of cd-free cu(in,ga)(se,s)2 minimodule via (zn,mg)o second buffer layer and alkali metal post-treatment," *IEEE Journal of Photovoltaics*, vol. 7, no. 6, pp. 1773–1780, 2017.

[26] Forrest, S.R., "The path to ubiquitous and low-cost organic electronic appliances on plastic," *Nature*, vol. 428, pp. 911–918, 2004.

[27] Hoppe, H. and Sariciftci, N.S., "Organic solar cells: An overview," *Journal of Materials Research*, vol. 19, no. 7, p. 19241945, 2004.

[28] Kaltenbrunner, M. et al, "Ultrathin and lightweight organic solar cells with high flexibility," *Nature Communications*, vol. 3, p. 770, 2012.

[29] Andersen, T.R. et al, "Scalable, ambient atmosphere roll-to-roll manufacture of encapsulated large area, flexible organic tandem solar cell modules," *Energy Environ. Sci.*, vol. 7, pp. 2925–2933, 2014.

[30] Li, Y., Xu, G., Cui, C. and Li, Y., "Flexible and semitransparent organic solar cells," *Advanced Energy Materials*, vol. 8, no. 7, p. 1701791, 2017.

[31] Carlé, J.E. et al, "Overcoming the scaling lag for polymer solar cells," *Joule*, vol. 1, no. 2, pp. 274–289, 2018.

[32] Shtein, M., Gossenberger, H.F., Benziger, J.B. and Forrest, S.R., "Material transport regimes and mechanisms for growth of molecular organic thin films using low-pressure organic vapor phase deposition," *Journal of Applied Physics*, vol. 89, no. 2, pp. 1470–1476, 2001.

[33] Vak, D. et al, "Fabrication of organic bulk heterojunction solar cells by a spray deposition method for low-cost power generation," *Applied Physics Letters*, vol. 91, no. 8, p. 081102, 2007.

[34] Ji, G. et al, "Fully coated semitransparent organic solar cells with a doctor-blade-coated composite anode buffer layer of phosphomolybdic acid and pedot:pss and a spray-coated silver nanowire top electrode," *ACS Applied Materials & Interfaces*, vol. 10, no. 1, pp. 943–954, 2018.

[35] Li, Y. et al, "High efficiency near-infrared and semitransparent non-fullerene acceptor organic photovoltaic cells," *Journal of the American Chemical Society*, vol. 139, no. 47, pp. 17114–17119, 2017.

[36] Henemann, A., "Bipv: Built-in solar energy," *Renewable Energy Focus*, vol. 9, no. 6, pp. 14–19, 2008.

[37] der Wiel, B.v., Egelhaaf, H.J., Issa, H., Roos, M. and Henze, N., "Market readiness of organic photovoltaics for building integration," *MRS Proceedings*, vol. 1639, 2014.

[38] Giebink, N.C., Wiederrecht, G.P., Wasielewski, M.R. and Forrest, S.R., "Ideal diode equation for organic heterojunctions. i. derivation and application," *Phys. Rev. B*, vol. 82, p. 155305, 2010.

[39] Forrest, S.R., "The limits to organic photovoltaic cell efficiency," *MRS Bulletin*, vol. 30, no. 1, p. 2832, 2005.

[40] Seaman, C.H., "Calibration of solar cells by the reference cell methodthe spectral mismatch problem," *Solar Energy*, vol. 29, no. 4, pp. 291–298, 1982.

[41] Peumans, P., Uchida, S. and Forrest, S.R., "Efficient bulk heterojunction photovoltaic cells using small-molecular-weight organic thin films," *Nature*, vol. 425, pp. 158–162, 2003.

[42] Yu, G., Gao, J., Hummelen, J.C., Wudl, F. and Heeger, A.J., "Polymer photovoltaic cells: Enhanced efficiencies via a network of internal donor-acceptor heterojunctions," *Science*, vol. 270, no. 5243, pp. 1789–1791, 1995.

[43] Xue, J., Rand, B., Uchida, S. and Forrest, S., "A hybrid planar-mixed molecular heterojunction photovoltaic cell," *Advanced Materials*, vol. 17, no. 1, pp. 66–71, 2004.

[44] Giebink, N.C., Wiederrecht, G.P., Wasielewski, M.R. and Forrest, S.R., "Thermodynamic efficiency limit of excitonic solar cells," *Phys. Rev. B*, vol. 83, p. 195326, 2011.

[45] Rand, B.P., Peumans, P. and Forrest, S.R., "Long-range absorption enhancement in organic tandem thin-film solar cells containing silver nanoclusters," *Journal of Applied Physics*, vol. 96, no. 12, pp. 7519–7526, 2004.

[46] Tang, C.W. and Albrecht, A.C., "Photovoltaic effects of metalchlorophyllametal sandwich cells," *The Journal of Chemical Physics*, vol. 62, no. 6, pp. 2139–2149, 1975.

[47] Tang, C.W., "Two-layer organic photovoltaic cell," *Applied Physics Letters*, vol. 48, no. 2, pp. 183–185, 1986.

[48] Peumans, P., Bulovi, V. and Forrest, S.R., "Efficient photon harvesting at high optical intensities in ultrathin organic double-heterostructure photovoltaic diodes," *Applied Physics Letters*, vol. 76, no. 19, pp. 2650–2652, 2000.

[49] Koltun, M. et al, "Solar cells from carbon," *Solar Energy Materials and Solar Cells*, vol. 44, no. 4, pp. 485–491, 1996.

[50] Peumans, P. and Forrest, S.R., "Very-high-efficiency double-heterostructure copper phthalocyanine/c_{60} photovoltaic cells," *Applied Physics Letters*, vol. 79, no. 1, pp. 126–128, 2001.

[51] Uchida, S., Xue, J., Rand, B.P. and Forrest, S.R., "Organic small molecule solar cells with a homogeneously mixed copper phthalocyanine:c60 active layer," *Applied Physics Letters*, vol. 84, no. 21, pp. 4218–4220, 2004.

[52] Zhao, J. et al, "Efficient organic solar cells processed from hydrocarbon solvents," *Nature Energy*, vol. 1, p. 15027, 2016.

[53] Cheng, P., Li, G., Zhan, X. and Yang, Y., "Next-generation organic photovoltaics based on non-fullerene acceptors," *Nature Photonics*, vol. 12, no. 3, pp. 131–142, 2018.

[54] Griffith, O.L. et al, "Charge transport and exciton dissociation in organic solar cells consisting of dipolar donors mixed with c_{70}," *Phys. Rev. B*, vol. 92, p. 085404, 2015.

[55] Che, X. et al, "Donor-acceptor-acceptor' molecules for vacuum-deposited organic photovoltaics with efficiency exceeding 9%," *Advanced Energy Materials*, 2018.

[56] Lin, H.W. et al, "An effective bilayer cathode buffer for highly efficient small molecule organic solar cells," *Organic Electronics*, vol. 13, no. 10, pp. 1925 – 1929, 2012.

[57] Li, T.y. et al, "Small molecule near-infrared boron dipyrromethene donors for organic tandem solar cells," *Journal of the American Chemical Society*, vol. 139, no. 39, pp. 13636–13639, 2017.

[58] Kan, B. et al, "A series of simple oligomer-like small molecules based on oligothiophenes for solution-processed solar cells with high efficiency," *Journal of the American Chemical Society*, vol. 137, no. 11, pp. 3886–3893, 2015.

[59] Zhang, S., Qin, Y., Zhu, J. and Hou, J., "Over 14% efficiency in polymer solar cells enabled by a chlorinated polymer donor," *Advanced Materials*, p. 1800868, 2018.

[60] Cui, Y. et al, "Efficient semitransparent organic solar cells with tunable color enabled by an ultralowbandgap nonfullerene acceptor," *Advanced Materials*, vol. 29, no. 43, p. 1703080, 2017.

[61] Xu, X. et al, "Highly efficient ternary-blend polymer solar cells enabled by a nonfullerene acceptor and two polymer donors with a broad composition tolerance," *Advanced Materials*, vol. 29, no. 46, p. 1704271, 2017.

[62] Yakimov, A. and Forrest, S.R., "High photovoltage multiple-heterojunction organic solar cells incorporating interfacial metallic nanoclusters," *Applied Physics Letters*, vol. 80, no. 9, pp. 1667–1669, 2002.

[63] Ameri, T., Li, N. and Brabec, C.J., "Highly efficient organic tandem solar cells: a follow up review," *Energy Environ. Sci.*, vol. 6, pp. 2390–2413, 2013.

[64] Che, X., Xiao, X., Zimmerman, J.D., Fan, D. and Forrest, S.R., "High-efficiency, vacuum-deposited, small-molecule organic tandem and triple-junction photovoltaic cells," *Advanced Energy Materials*, vol. 4, no. 18, p. 1400568, 2014.

[65] Li, W., Furlan, A., Hendriks, K.H., Wienk, M.M. and Janssen, R.A.J., "Efficient tandem and triple-junction polymer solar cells," *Journal of the American Chemical Society*, vol. 135, no. 15, pp. 5529–5532, 2013.

[66] You, J. et al, "A polymer tandem solar cell with 10.6% power conversion efficiency," *Nature Communications*, vol. 4, p. 1446, 2013.

[67] Chen, C. et al, "An efficient triplejunction polymer solar cell having a power conversion efficiency exceeding 11%," *Advanced Materials*, vol. 26, no. 32, pp. 5670–5677, 2014.

[68] Yusoff, A.R.b.M. et al, "A high efficiency solution processed polymer inverted triple-junction solar cell exhibiting a power conversion efficiency of 11.83%," *Energy Environ. Sci.*, vol. 8, pp. 303–316, 2015.

[69] Li, M. et al, "Solution-processed organic tandem solar cells with power conversion efficiencies > 12%," *Nature Photonics*, vol. 11, pp. 85–90, 2017.

[70] Cui, Y. et al, "Fine-tuned photoactive and interconnection layers for achieving over 13% efficiency in a fullerene-free tandem organic solar cell," *Journal of the American Chemical Society*, vol. 139, no. 21, pp. 7302–7309, 2017.

[71] Burlingame, Q. et al, "Reliability of small molecule organic photovoltaics with electronfiltering compound buffer layers," *Advanced Energy Materials*, vol. 6, no. 21, p. 1601094, 2016.

[72] Gilot, J., Wienk, M.M. and Janssen, R.A.J., "Optimizing polymer tandem solar cells," *Advanced Materials*, vol. 22, no. 8, pp. E67–E71, 2010.

[73] Van der Auweraer, M., De Schryver, F.C., Borsenberger, P.M. and Bssler, H., "Disorder in charge transport in doped polymers," *Advanced Materials*, vol. 6, no. 3, pp. 199–213, 1994.

[74] Wrthner, F. and Meerholz, K., "Systems chemistry approach in organic photovoltaics," *Chemistry A European Journal*, vol. 16, no. 31, pp. 9366–9373, 2010.

[75] Lin, H.W. et al, "A new donor-acceptor molecule with uniaxial anisotropy for efficient vacuum-deposited organic solar cells," *Chem. Commun.*, vol. 47, pp. 7872–7874, 2011.

[76] Kim, J. et al, "Highly efficient vacuum-processed organic solar cells containing thieno[3,2-b]thiophene-thiazole," *The Journal of Physical Chemistry C*, vol. 118, no. 22, pp. 11559–11565, 2014.

[77] Lin, L.Y. et al, "A low-energy-gap organic dye for high-performance small-molecule organic solar cells," *Journal of the American Chemical Society*, vol. 133, no. 40, pp. 15822–15825, 2011.

[78] Lin, H.W. et al, "Pyridine-based electron transporting materials for highly efficient organic solar cells," *J. Mater. Chem. A*, vol. 1, pp. 1770–1777, 2013.

[79] Chen, Y.H. et al, "Vacuum-deposited small-molecule organic solar cells with high power conversion efficiencies by judicious molecular design and device optimization," *Journal of the American Chemical Society*, vol. 134, no. 33, pp. 13616–13623, 2012.

[80] Zou, Y., Holst, J., Zhang, Y. and Holmes, R.J., "7.9% efficient vapor-deposited organic photovoltaic cells based on a simple bulk heterojunction," *J. Mater. Chem. A*, vol. 2, pp. 12397–12402, 2014.

[81] Kazaoui, S. et al, "Comprehensive analysis of intermolecular charge-transfer excited states in c_{60} and c_{70} films," *Phys. Rev. B*, vol. 58, pp. 7689–7700, 1998.

[82] Li, N., Lassiter, B.E., Lunt, R.R., Wei, G. and Forrest, S.R., "Open circuit voltage enhancement due to reduced dark current in small molecule photovoltaic cells," *Applied Physics Letters*, vol. 94, no. 2, p. 023307, 2009.

[83] Chan, M.Y. et al, "Efficient organic photovoltaic devices using a combination of exciton blocking layer and anodic buffer layer," *Journal of Applied Physics*, vol. 100, no. 9, p. 094506, 2006.

[84] Bartynski, A.N. et al, "A fullerene-based organic exciton blocking layer with high electron conductivity," *Nano Letters*, vol. 13, no. 7, pp. 3315–3320, 2013.

[85] Nunomura, S., Sakata, I. and Kondo, M., "In situ photocurrent measurements of thin-film semiconductors during plasma-enhanced chemical vapor deposition," *Applied Physics Express*, vol. 6, no. 12, p. 126201, 2013.

[86] Nunomura, S., Che and Forrest, S.R., "Charge trapping in mixed organic donoracceptor semiconductor thin films," *Advanced Materials*, vol. 26, no. 45, pp. 7555–7560, 2014.

[87] Burlingame, Q. et al, "Centimetre-scale electron diffusion in photoactive organic heterostructures," *Nature*, vol. 554, pp. 77–80, 2018.

[88] Lu, H.I. et al, "New molecular donors with dithienopyrrole as the electron-donating group for efficient small-molecule organic solar cells," *Chemistry of Materials*, vol. 26, no. 15, pp. 4361–4367, 2014.

[89] Che, X. et al, "Regioisomeric effects of donoracceptoracceptor small-molecule donors on the open circuit voltage of organic photovoltaics," *Advanced Materials*, vol. 28, no. 37, pp. 8248–8255, 2016.

[90] Meyers, F., Marder, S.R., Pierce, B.M. and Bredas, J.L., "Electric field modulated nonlinear optical properties of donor-acceptor polyenes: Sum-over-states investigation of the relationship between molecular polarizabilities (.alpha., .beta., and .gamma.) and bond length alternation," *Journal of the American Chemical Society*, vol. 116, no. 23, pp. 10703–10714, 1994.

[91] Pai, C.L., Liu, C.L., Chen, W.C. and Jenekhe, S.A., "Electronic structure and properties of alternating donoracceptor conjugated copolymers: 3,4-ethylenedioxythiophene (edot) copolymers and model compounds," *Polymer*, vol. 47, no. 2, pp. 699–708, 2006.

[92] Chung, C.L. et al, "A-d-a type organic donors employing coplanar heterocyclic cores for efficient small molecule organic solar cells," *Organic Electronics*, vol. 28, pp. 229–238, 2016.

[93] Coropceanu, V. et al, "Charge transport in organic semiconductors," *Chemical Reviews*, vol. 107, no. 4, pp. 926–952, 2007.

[94] Armin, A. et al, "Balanced carrier mobilities: Not a necessary condition for high-efficiency thin organic solar cells as determined by mis-celiv," *Advanced Energy Materials*, vol. 4, no. 4, p. 1300954, 2014.

[95] Juka, G., Nekraas, N. and Geneviius, K., "Investigation of charge carriers transport from extraction current transients of injected charge carriers," *Journal of Non-Crystalline Solids*, vol. 358, no. 4, pp. 748–750, 2012.

[96] Mark, P. and Helfrich, W., "Space-charge-limited currents in organic crystals," *Journal of Applied Physics*, vol. 33, no. 1, pp. 205–215, 1962.

[97] Bulovi, V., Deshpande, R., Thompson, M. and Forrest, S., "Tuning the color emission of thin film molecular organic light emitting devices by the solid state solvation effect," *Chemical Physics Letters*, vol. 308, no. 3, pp. 317–322, 1999.

[98] Renshaw, C.K., Zimmerman, J.D., Lassiter, B.E. and Forrest, S.R., "Photoconductivity in donor-acceptor heterojunction organic photovoltaics," *Phys. Rev. B*, vol. 86, p. 085324, 2012.

[99] Gierschner, J., Cornil, J. and Egelhaaf, H.J., "Optical bandgaps of π-conjugated organic materials at the polymer limit: Experiment and theory," *Advanced Materials*, vol. 19, no. 2, pp. 173–191, 2007.

[100] Torras, J., Casanovas, J. and Alemn, C., "Reviewing extrapolation procedures of the electronic properties on the -conjugated polymer limit," *The Journal of Physical Chemistry A*, vol. 116, no. 28, pp. 7571–7583, 2012.

[101] Mishra, A. et al, "Ada-type s,n-heteropentacenes: Next-generation molecular donor materials for efficient vacuum-processed organic solar cells," *Advanced Materials*, vol. 26, no. 42, pp. 7217–7223, 2014.

[102] Liu, J. et al, "Tri-diketopyrrolopyrrole molecular donor materials for high-performance solution-processed bulk heterojunction solar cells," *Advanced Materials*, vol. 25, no. 41, pp. 5898–5903, 2013.

[103] Forrest, S.R., "Ultrathin organic films grown by organic molecular beam deposition and related techniques," *Chemical Reviews*, vol. 97, no. 6, pp. 1793–1896, 1997.

[104] Fritz, S.E., Martin, S.M., Frisbie, C.D., Ward, M.D. and Toney, M.F., "Structural characterization of a pentacene monolayer on an amorphous sio2 substrate with grazing incidence x-ray diffraction," *Journal of the American Chemical Society*, vol. 126, no. 13, pp. 4084–4085, 2004.

[105] Lassiter, B.E., Zimmerman, J.D., Panda, A., Xiao, X. and Forrest, S.R., "Tandem organic photovoltaics using both solution and vacuum deposited small molecules," *Applied Physics Letters*, vol. 101, no. 6, p. 063303, 2012.

[106] Lassiter, B.E., Zimmerman, J.D. and Forrest, S.R., "Tandem organic photovoltaics incorporating two solution-processed small molecule donor layers," *Applied Physics Letters*, vol. 103, no. 12, p. 123305, 2013.

[107] Zimmerman, J.D. et al, "Control of interface order by inverse quasi-epitaxial growth of squaraine/fullerene thin film photovoltaics," *ACS Nano*, vol. 7, no. 10, pp. 9268–9275, 2013.

[108] Lassiter, B.E., Renshaw, C.K. and Forrest, S.R., "Understanding tandem organic photovoltaic cell performance," *Journal of Applied Physics*, vol. 113, no. 21, p. 214505, 2013.

[109] Xiao, X., Bergemann, K.J., Zimmerman, J.D., Lee, K. and Forrest, S.R., "Small-molecule planar-mixed heterojunction photovoltaic cells with fullerene-based electron filtering buffers," *Advanced Energy Materials*, vol. 4, no. 7, p. 1301557, 2014.

[110] Cheyns, D., Kim, M., Verreet, B. and Rand, B.P., "Accurate spectral response measurements of a complementary absorbing organic tandem cell with fill factor exceeding the subcells," *Applied Physics Letters*, vol. 104, no. 9, p. 093302, 2014.

[111] Timmreck, R. et al, "Characterization of tandem organic solar cells," *Nature Photonics*, vol. 9, pp. 478–479, 2015.

[112] Tang, M.L., Oh, J.H., Reichardt, A.D. and Bao, Z., "Chlorination: A general route toward electron transport in organic semiconductors," *Journal of the American Chemical Society*, vol. 131, no. 10, pp. 3733–3740, 2009.

[113] Xi, J.Q. et al, "Very low-refractive-index optical thin films consisting of an array of sio$_2$ nanorods," *Opt. Lett.*, vol. 31, no. 5, pp. 601–603, 2006.

[114] Slootsky, M. and Forrest, S.R., "Enhancing waveguided light extraction in organic leds using an ultra-low-index grid," *Opt. Lett.*, vol. 35, no. 7, pp. 1052–1054, 2010.

[115] Xiao, X., Lee, K. and Forrest, S.R., "Scalability of multi-junction organic solar cells for large area organic solar modules," *Applied Physics Letters*, vol. 106, no. 21, p. 213301, 2015.

[116] Liu, J. et al, "Fast charge separation in a non-fullerene organic solar cell with a small driving force," *Nature Energy*, Jun 2016.

[117] Li, Y. et al, "Non-fullerene acceptor with low energy loss and high external quantum efficiency: towards high performance polymer solar cells," *J. Mater. Chem. A*, vol. 4, pp. 5890–5897, 2016.

[118] Moriarty, T., Jablonski, J. and Emery, K., "Algorithm for building a spectrum for nrel's one-sun multi-source simulator," in *2012 38th IEEE Photovoltaic Specialists Conference*, pp. 001291–001295, 2012.

[119] Babayigit, A., Ethirajan, A., Muller, M. and Conings, B., "Toxicity of organometal halide perovskite solar cells," *Nature Materials*, vol. 15, pp. 247–251, 2016.

[120] Sanehira, E.M. et al, "Enhanced mobility cspbi3 quantum dot arrays for record-efficiency, high-voltage photovoltaic cells," *Science Advances*, vol. 3, no. 10, 2017.

[121] Huang, J. et al, "Highly efficient organic solar cells consisting of double bulk heterojunction layers," *Advanced Materials*, vol. 29, no. 19, p. 1606729, 2017.

[122] Faist, M.A. et al, "Understanding the reduced efficiencies of organic solar cells employing fullerene multiadducts as acceptors," *Advanced Energy Materials*, vol. 3, no. 6, pp. 744–752, 2013.

[123] Ameri, T., Khoram, P., Min, J. and Brabec, C.J., "Organic ternary solar cells: A review," *Advanced Materials*, vol. 25, no. 31, pp. 4245–4266, 2013.

[124] Hou, J., Inganäs, O., Friend, R.H. and Gao, F., "Organic solar cells based on non-fullerene acceptors," *Nature Materials*, vol. 17, pp. 119–128, 2018.

[125] Mantilla-Perez, P., Martinez-Otero, A., Romero-Gomez, P. and Martorell, J., "4-terminal tandem photovoltaic cell using two layers of ptb$_7$:pc$_{71}$bm for optimal light absorption," *ACS Applied Materials & Interfaces*, vol. 7, no. 33, pp. 18435–18440, 2015.

[126] Machui, F. et al, "Cost analysis of roll-to-roll fabricated ito free single and tandem organic solar modules based on data from manufacture," *Energy Environ. Sci.*, vol. 7, pp. 2792–2802, 2014.

[127] Gasparini, N. et al, "Burnin free nonfullerenebased organic solar cells," *Advanced Energy Materials*, vol. 7, no. 19, p. 1700770, 2018.

[128] Emmott, C.J.M. et al, "Organic photovoltaic greenhouses: a unique application for semi-transparent pv?," *Energy Environ. Sci.*, vol. 8, no. 4, pp. 1317–1328, 2015.